SAPIENZA
UNIVERSITÀ DI ROMA

Spontaneous photonic lattices and nonlinear waves in nanodisordered ferroelectrics

Facoltà di Scienze Matematiche, Fisiche e Naturali

Dottorato di Ricerca in Fisica – XXXI Ciclo

Candidate

Mariano Flammini

ID number 1353210

Thesis Advisor

Prof. Eugenio Del Re

February 2019

Thesis defended on 12 February 2019
in front of a Board of Examiners composed by:

Livia Bove, Carlo Altucci, Elisa Molinari (chairman)

Spontaneous photonic lattices and nonlinear waves in nanodisordered ferroelectrics
Ph.D. thesis. Sapienza – University of Rome

© 2019 Mariano Flammini. All rights reserved

This thesis has been typeset by LaTeX and the Sapthesis class.

Author's email: mariano.flammini@uniroma1.it

A mio nonno Checco

List of publications discussed in this Thesis

- D. Pierangeli, M. Flammini, L. Zhang, G. Marcucci, A. J. Agranat, P. G. Grinevich, P. M. Santini, C. Conti, and E. DelRe"Observation of Fermi-Pasta-Ulam-Tsingou Recurrence and Its Exact Dynamics," *Phys. Rev. X* **8**, 041017 (2018);

- F. Di Mei, L. Falsi, M. Flammini, D. Pierangeli, P. Di Porto, A. J. Agranat, and E. DelRe, "Giant broadband refraction in the visible in a ferroelectric perovskite," *Nat. Photonincs* **12**, 734-738 (2018);

- M. Flammini, G. Di Domenico, D. Pierangeli, F. Di Mei, A. J. Agranat and E. DelRe, "Observation of Bessel-beam self-trapping," *Phys Rev. A* **98**, 033808 (2018);

- C. Ciano, M. Flammini, V. Giliberti, P. Calvani, E. DelRe, F. Talarico, M. Torre, M. Missori and M. Ortolani, "Confocal Imaging at 0.3 THz With Depth Resolution of a Painted Wood Artwork for the Identification of Buried Thin Metal Foils," *IEEE T THz Sci Techn* **8**, 390-396 (2018);

- M. Flammini, E. Pontecorvo, V. Giliberti, C. Rizza, A. Ciattoni, M. Ortolani and E. DelRe, "Observation of evanescent-wave filtering in images using remote terahertz structured illumination," *Phys. Rev. Applied* **8**, 054019 (2017);

- M. Ferraro, D. Pierangeli, M. Flammini, G. Di Domenico, L. Falsi, F. Di Mei, A. J. Agranat and E. DelRe, "Observation of polarization-maintaining light propagation in depoled compositionally disordered ferroelectrics," *Opt. Lett.* **42**, 3856-3859 (2017);

- M. Flammini, C. Bonsi, C. Ciano, V. Giliberti, E. Pontecorvo, P. Italia, E. DelRe and M. Ortolani, "Confocal Terahertz Imaging of Ancient Manuscripts," *J Infrared Milli Terahz Waves* **38**, 435–442 (2017);

- D. Pierangeli, M. Flammini, F. Di Mei, J. Parravicini, C. E. M. de Oliveira, A. J. Agranat and E. DelRe, "Continuous solitons in a lattice nonlinearity," *Phys. Rev. Lett.* **114**, 203901 (2015).

Abstract

In this Thesis we deal with nanodisordered ferroelectric perovskite crystals. These material have been demonstrated to be a good test-bed to study nonlinear optical phenomena due to their strong optical properties. In fact, their embedded disorder enhances their response at the phase transition and makes these materials suitable to sustain solitons and rogue waves also with low optical power.

We first use self-focusing at the paraelectric phase to study nonlinear wave propagation. Our experiments are conceived to investigate the evolution of structured waves in time and in space. We make three beams to interfere to optically observe the Fermi-Pasta-Ulam-Tsingou recurrence. We experimentally verify its analytic solution provided by Grinevich-Santini that allows us to predict the exact position of each recurrence. Moreover, we demonstrate that the periodic behavior is lost if the system ceases to be integrable. We study the appropriate interference pattern in the form of nondiffractive Bessel beams to investigate what happens to such waves in a self-focusing medium. We identify two regimes: a Bessel beam self-trapping and a breathing soliton. Furthermore, we demonstrate the feasibility of Bessel beam writing to build a scalable and rewritable network of waveguides inside the bulk ferroelectric medium.

We also studied the unique properties of the ferroelectric phase. The most evident outcome is the so-called super-crystal that is a spontaneous photonic 3D lattice that emerges from the interplay between material order and disorder. We study the super-crystal in different ways and we recover the periodic behavior for linear and nonlinear propagation. In detail we report a periodic pattern for birefringence and second harmonic generation. The main result is that we have observed the highest value of the refractive index reported in literature for visible light and we have connected the effect to the super-crystal. This material allows, in theory, to transmit light without any information loss, that is without diffraction and chromatic dispersion.

The physics of diffraction is also investigated with the introduction of an innovative method to achieve super-resolution. We exploit a confocal microscope and a remote knife-edge technique. This allows us to directly study the role of evanescent waves in super-resolution imaging forming, i.e. they are filtered out as the super-resolved image approaches to the diffraction-limited one. Experiments here are performed with a terahertz frequency,

$\lambda \sim 1.00$ mm, to easily accede the near field and capture the information carried by the evanescent waves.

Although all topics are related to each other, we thought it appropriate to split the thesis into three parts which correspond to the main topics that we have addressed during the PhD.

In Part 1, our main interest is on the nonlinear propagation of specifically designed light patterns. In Chapter 1, we introduce the theoretical basis necessary to support our experimental findings. We introduce the nonlinear Schrödinger equation (NLSE), the equation that rules most of nonlinear optics, and we solve it for several significant input conditions. Then, we describe the beam propagation method, an important tool to obtain a numerical integration of the NLSE. In Chapter 2, we report the experimental observation of the Fermi-Pasta-Ulam-Tsingou recurrence and we compare results to the Grinevich-Santini theory. In Chapter 3, we deal with Bessel beams. We show the self-trapping/breathing state and we illustrate the Bessel wave-guide method. In Chapter 4 we the study the nonlinear lattice embedded in a ferroelectric perovskite. The resultant periodic nonlinearity disappears during the photorefractive cumulative process.

In the Part 2 our interest is on the nanodisordered ferroelectric perovskite, so that, here, light represents the main probe to investigate crystal properties. In Chapter 5 we introduce the samples and in particular we describe the super-crystal. In Chapter 6 we deal with the linear response of the super-crystal and we report the formation of a light polarization lattice. We also study the temperature dependence of the phenomenon, discovering that trough polarization measurements we can characterize the paraelectric-ferroelectric transition. In Chapter 7 we exploit the crystal compositional disorder to achieve second harmonic generation through random phase-matching. Our preliminary study indicates a 3D photonic lattice that is the nonlinear analogue of the super-crystal. In Chapter 8 we report the observation of the index of refraction. We perform experiments with both laser light and white light and we estimate $n_0 > 26$.

In Part 3 we describe our experiments with a confocal microscope in the terahertz radiation. In Chapter 9 we introduce the method to achieve remote super-resolution through the knife-edge technique and we study the filtering out of the evanescent components varying the distance of the knife from the sample.

Contents

List of publications discussed in this Thesis iii

Abstract **iv**

I Nonlinear optical spatial waves **1**

1 Introduction **3**
1.1 Nonlinear wave equation 3
1.2 Notable solutions of the linear Helmholtz equation 5
1.2.1 Gaussian Beam 5
1.2.2 Bessel Beam and Airy Beam 6
1.3 Photorefractive effect 7
1.3.1 The Kukhtarev-Vinetskiis model 8
1.3.2 Nonlinear variation of the refractive index 11
1.3.3 Cumulative nature of photorefractive response 12
1.4 Photorefractive screening soliton 14
1.4.1 (1+1)D Soliton 14
1.4.2 Anisotropy in the photorefractive response and (2+1D) soliton . . . 15
1.4.3 Solitons interaction 16
1.5 Modulation Instability 16
1.6 Rogue Waves 17
1.7 Numerical solution of the NLSE 19
1.7.1 BPM simulation of (1+1D) soliton 20

2 Observation of the exact dynamics of the Fermi-Pasta-Ulam-Tsingou recurrence **22**
2.1 Integrability and the FPUT problem 22
2.2 Exact recurrences in the nonlinear Schrödinger equation 23
2.3 Numerical Simulations 25
2.4 Experimental Setup 26

2.5 Experimental Results . . . 30
2.5.1 Analysis of the recurrence . . . 33
2.6 Discussion . . . 34

3 Bessel Beam propagation in self-focusing medium 36
3.1 Nonlinear Nondiffracting Waves: an overview . . . 36
3.2 Numerical Results . . . 37
3.3 Experimental Results . . . 38
3.4 Bessel self-trapping interaction . . . 43
3.5 Discussion . . . 45
3.6 Bessel beams waveguide induction . . . 46
3.6.1 Theoretical Background . . . 47
3.6.2 Experiments . . . 48

4 Continuous Soliton in a Lattice Nonlinearity 51
4.1 Physical Context . . . 51
4.2 Experimental Environment . . . 53
4.3 Numerical Simulations . . . 54
4.4 Experimental Results . . . 55

II Optics in nanodisordered ferroelectrics 59

5 Super-crystals in composite ferroelectrics 61
5.1 Ferroelectric Perovskites . . . 61
5.2 Polar Nano Regions and Relaxors . . . 63
5.3 Spontaneous Ordered Phase Transition . . . 65
5.3.1 Super-Crystal Observation . . . 65
5.3.2 Super-Crystal Model . . . 68

6 Observation of polarization-maintaining light propagation in depoled compositionally disordered ferroelectrics 71
6.1 Light Polarization in Anisotropic Media . . . 71
6.2 Experimental Setup . . . 73
6.3 Global Stokes Parameter Measurements . . . 74
6.4 Spatially Resolved Experiments . . . 75
6.5 Temperature Varying Measurements . . . 76

7 Second Harmonic Generation in nanodisordered ferroelectrics 78
7.1 Second Harmonic Generation . . . 78
7.1.1 Phase-Matching . . . 79

7.2 Phase Matching In Periodic Structures . . . 80
7.3 Random Phase Matching . . . 82
7.4 Preliminary Results . . . 83

8 Giant broadband refraction in the visible in a ferroelectric perovskite 86
8.1 Fresnel Refraction Theory . . . 86
8.1.1 Giant Refraction and Anisotropy . . . 87
8.2 Experimental Setup . . . 88
8.3 White Light Propagation . . . 90
8.4 Laser Light Propagation . . . 92
8.4.1 Index of refraction evaluation from diffraction . . . 96
8.5 Perspectives . . . 96

III Knife-Edge Super-Resolution 97

9 Evanescent-Wave Filtering in Images Using Remote Terahertz Structured Illumination 99
9.1 Introduction . . . 99
9.2 Fourier Analysis Method . . . 101
9.3 Remote Super-Resolution . . . 101
9.4 Experiments . . . 103
9.5 Results . . . 107
9.6 Ultimate resolution limit . . . 109
9.7 Discussion . . . 110
9.8 Future Perspectives . . . 111

Conclusions 112

Acknowledgments 113

Bibliography 114

Part I

Nonlinear optical spatial waves

In this Part we discuss the propagation of specific light patterns in a Kerr-like nonlinearity. We first introduce the theoretical background necessary to support our experimental findings. Then we describe experiments on the Fermi-Pasta-Ulam-Tsingou recurrence. We study Bessel Beams and their propagation in conditions of extreme self-focusing, addressing also the possibility to exploit them to write waveguides in the bulk ferroelectric medium. Finally, we describe the formation of spatial solitons in a periodic linear and nonlinear index of refraction pattern.

Our results are published in Ref. [1], [2] and [3].

Chapter 1

Introduction

In the first Chapter we describe the theoretical background necessary to understand the arguments treated in the following chapters. First, we highlight the role of the paraxial Helmholtz equation in describing propagation. We point out that, including a nonlinearity, we obtain the nonlinear Schrödinger equation. Then, we find the expression of the nonlinear variation of the refraction index according to our specific system and, thanks to this, we are able to introduce some of the main nonlinear phenomena: solitons, modulation instability and rogue waves.

1.1 Nonlinear wave equation

In this Section we derive the nonlinear wave equation starting from the Maxwell Equations and we recall its wide field of application, beyond optics. The macroscopic Maxwell equations are [4]:

$$\nabla \cdot \vec{D} = \rho_l \tag{1.1a}$$

$$\nabla \cdot \vec{B} = 0 \tag{1.1b}$$

$$\nabla \times \vec{E} = -\frac{\partial \vec{B}}{\partial t} \tag{1.1c}$$

$$\nabla \times \vec{H} = \frac{\partial \vec{D}}{\partial t} + \vec{J}, \tag{1.1d}$$

where ρ_l is the free-charge density whereas $\vec{J}$ is the current density. In dielectrics, $\vec{H}$ e $\vec{D}$ are specified by the constitutive relations

$$\vec{D} = \varepsilon_0 \vec{E} + \vec{P} \tag{1.2a}$$

$$\vec{B} = \mu_0(\vec{H} + \vec{M}), \tag{1.2b}$$

where $\vec{P}$ and $\vec{M}$ are the vectors of electric and magnetic polarization respectively. We can always take $\vec{M} = 0$ and $\mu_r = 1$ since all media that we have studied have a negligible magnetization. We can consider $\vec{P}(\vec{E}) = \varepsilon_0(\bar{\bar{\varepsilon}}_r - 1)\vec{E}$ so that $\vec{D} = \bar{\bar{\varepsilon}}\vec{E}$ with $\bar{\bar{\varepsilon}} = \varepsilon_0\bar{\bar{\varepsilon}}_r$ where $\bar{\bar{\varepsilon}}_r$ is the two index permittivity tensor which, from here on, we recall ε and $\varepsilon_0 \approx 8.85 \cdot 10^{-12}$ F/m is the vacuum permittivity. Now we take the monochromatic field $\vec{E}(\vec{r}, t) = \vec{E}_\omega(\vec{r})e^{i\omega t}$, with ω the fixed frequency and with the above consideration, we can rewrite the Maxwell Equations

$$\nabla \cdot (\varepsilon_\omega \vec{E}_\omega) = 0, \tag{1.3a}$$

$$\nabla \cdot \vec{H}_\omega = 0, \tag{1.3b}$$

$$\nabla \times \vec{E}_\omega = -i\omega\mu_0\vec{H}_\omega, \tag{1.3c}$$

$$\nabla \times \vec{H}_\omega = i\omega\varepsilon(\omega)\vec{E}_\omega. \tag{1.3d}$$

We apply $\nabla\times$ to (1.3c) and, exploiting (1.3a) and (1.3d), we obtain

$$\nabla^2\vec{E}_\omega + \nabla\left(\vec{E} \cdot \frac{\nabla\varepsilon}{\varepsilon}\right) + \frac{\varepsilon}{\varepsilon_0}\frac{\omega^2}{c^2}\vec{E}_\omega = 0, \tag{1.4}$$

with $c = \frac{1}{\sqrt{\mu_0\varepsilon_0}} \approx 2.99 \cdot 10^8$ m/s that is the speed of light in vacuum. We define the refractive index as $n(\omega, \vec{r}) = \sqrt{\frac{\varepsilon(\omega,\vec{r}}{\varepsilon_0}} = \sqrt{\bar{\bar{\varepsilon}}_r}$ and $k_0 = \frac{\omega}{c} = \frac{2\pi}{\lambda}$ and we can rewrite Eq. (1.4):

$$\nabla^2\vec{E}_\omega + 2\nabla\left(\vec{E}_\omega \cdot \nabla\ln(n(\omega))\right) + k_0^2 n^2(\omega)\vec{E}_\omega = 0. \tag{1.5}$$

This is a vectorial equation that we can simplify following the dimensional analysis of Ref. [5]. We can neglect the second term of Eq. (1.5) for $\lambda \sim 0.5\mu m$ (optics fields) and for common beam dimensions and we obtain the Helmholtz scalar equation

$$\nabla^2\vec{E}_\omega + k_0^2 n^2(\vec{r})\vec{E}_\omega = 0, \tag{1.6}$$

with the refractive index $n(\vec{r}) = n_0 + \delta n(\vec{r})$ where n_0 is its constant part whereas $\delta n(\vec{r})$ is the position dependent part that includes the nonlinearity. In our experiments the longitudinal size of the beam l_z is much lager than its transverse size l_{xy}, typically $l_z \sim 1 \div 3$ m and $l_{xy} \sim 10 \div 1000$ μm. In these conditions, the paraxial approximation holds and the field can be expressed as $\vec{E}_\omega(\vec{r}) = \vec{A}_\omega(\vec{r}_\perp, z)e^{-ik(\omega)z}$ with $k(\omega) = k_0 n_1(\omega) = \frac{\omega}{c}n_1(\omega)$. Finally, exploiting all the previous formulas we can write the paraxial Helmholtz equation:

$$\frac{\partial\vec{A}_\omega}{\partial z} + \frac{i}{2k}\nabla_\perp^2\vec{A}_\omega = -ik\frac{\delta n(\vec{r})}{n_0}\vec{A}_\omega, \tag{1.7}$$

here the term with $\partial^2/\partial z^2$ does not appear because we have imposed the Slowly Varying Envelop Approximation (SVEA). Eq. (1.7) represents a fundamental equation for beam

propagation. We will extensively recall Eq. (1.7) in this Thesis to predict and verify the experimental findings. The second term describes diffraction, i.e. the beam spreading, whereas the term on right is the general expression of nonlinearity. We point out that, despite the fact that we have obtained it from Maxwell equation, Eq. (1.7) is relevant in a more general context, in fact, it is called NonLinear Schrödinger Equation (NLSE) and has the same structure of the Schrödinger Equation in quantum mechanics. NLSE can be found in almost of the systems concerning waves [6–13], therefore optics represents a good test-bed to discover most of the NLSE possibilities.

1.2 Notable solutions of the linear Helmholtz equation

In this Section we limit our analysis to the linear part of Eq. (1.7) [and Eq. (1.6)]. Discarding all the nonlinear contributions, we get the linear paraxial Helmholtz equation

$$\frac{\partial \vec{A}_\omega}{\partial z} + \frac{i}{2k}\nabla_\perp^2 \vec{A}_\omega = 0. \tag{1.8}$$

Two of the most notable solutions of Eq. (1.8) are the gaussian beam and Bessel beam which we introduce below.

1.2.1 Gaussian Beam

The gaussian beam is a specific parabolic solution of Eq. (1.8) and it is expressed by the following formula for x-polarized beam propagating along z [14]

$$\vec{A}(r,z) = A_0 \hat{x} \frac{w_0}{w(z)} \exp\left(\frac{-r^2}{w(z)^2}\right) \exp\left(-i\left(kz + k\frac{r^2}{2R(z)} - \zeta(z)\right)\right), \tag{1.9}$$

where $r = \sqrt{x^2+y^2}$, z is the axial distance from the focus, $R(z)$ is the radius of curvature of the beam wavefront, $w(z)$ is the beam width at a given position z with $w_0 \equiv w(z=0)$ the so-called beam waist. The phase term $\zeta(z)$ is the so-called Gouy phase, a phase that have to be considered as well as the phase velocity.

The beam intensity $I = \frac{|\vec{A}(r,z)|^2}{2\eta_i}$ (with η_i the wave impedance) is obtained evaluating the modulus of the pointing vector $\vec{S}$ which has always the z direction [4]. We get $I(r,z) = I_0\left(\frac{w_0}{w(z)}\right)^2 \exp\left(\frac{-2r^2}{w^2(z)}\right)$ so that the intensity I has a clear guassian shape with $w^2(z)/2$ that represents its variance. Instead of using $w(z)$, in our experiments we prefer to exploit the so-called Full-Width-at-Half-Maximum (FWHM) to describe the beam dimension. We point out that $\mathrm{FWHM}(z) = \sqrt{2\ln 2}w(z)$.

The beam width is $w(z) = w_0\sqrt{\frac{z}{z_R}}$, so that we can introduce the Rayleigh length (or Rayleigh range) $z_R = \frac{\pi w_0^2}{\lambda}$. At $z = z_R$ the beam width is $\sqrt{2}$ larger, and conventionally z_R

is an important parameter to experimentally characterize the the intrinsic diffraction of a gaussian beam.

In the end, we note that the Fourier transform of gaussian beam is a gaussian beam itself. This fact is very important because gaussian beams preserve its own shape passing through a lens, since every lens produces the Fourier transform of the input beam [15].

1.2.2 Bessel Beam and Airy Beam

In this Paragraph we introduce two of the most significant non-diffractive solutions of (1.8). The property of non-diffraction arises from plane waves, also solutions (1.8). Indeed, non-diffracting beams are volume interference patterns of plane waves and inherited their proprieties [2]. For example, these patterns exhibit self-healing, i.e. they reform after an obstacle, since their parent plane waves permeate all space. The Airy Beam (AB) and the Bessel Beam (BB) belong to the category of non-diffractive beams. Both AB and BB carry an infinite amount of energy and have an infinite number of secondary lobes that provide energy to the main lobe, avoiding diffraction[16, 17]. A realization of both consist in considering for example AB or BB with a gaussian envelope. These new solutions, the so called Airy-Gauss beam or Bessel-Gauss beam, maintain the properties or AB and BB but only for finite distances suitable for experiments [18, 19]. These nondiffracting waves are encountered in many fields, i.e in acoustics [20–22], quantum mechanics [16, 23] and in optics[17, 24, 25] with several associated applications, i.e. in plasma generation [26], material processing [27, 28] and microscopy [29].

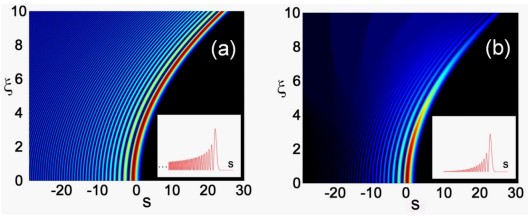

Figure 1.1. Propagation of (a) Airy beam and (b) Airy-Gauss beam. (From Ref. [25])

ABs bend during propagation, as reported in Fig. 1.1(a), and they are often called accelerating beams [16]. Considering the dimensionless variables $s = x/x_0$ and $\xi = z/kx_0$ with x_0 an arbitrary transverse scale, the AB expression is [25]

$$E(\xi, s) = Ai\left(s - (\xi/2)^2\right) \exp\left(i(s\xi/2) - i(\xi^3/12)\right) \tag{1.10}$$

with Ai the Airy function. As shown in Fig. 1.1(b), Airy-Gauss beam maintains most of the features of the AB, i.e. the bending, but progressively loses intensity. Looking at the intensity profiles, the insets of Fig. 1.1, it is clear that the tail of Airy-Bessel beam decays

faster than the tail of AB.

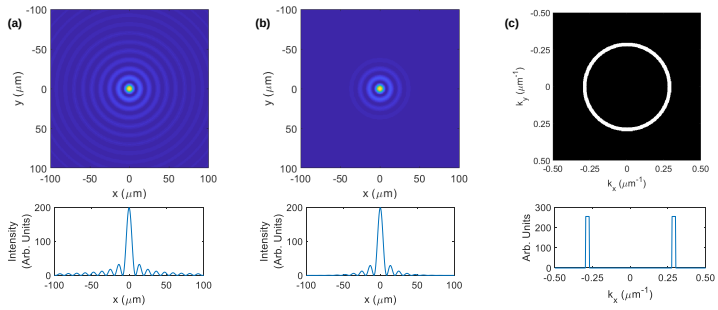

Figure 1.2. Numerical simulation of the transverse intensity of (a) Bessel and (b) Bessel-Gauss beam. In the numerics we use $k_r = 0.28\ \mu\text{m}^{-1}$ and, only for (b), $\sigma = 60\ \mu$m. (c) Fourier trasform of the Bessel beam in (a).

A BB is characterized by the presence of a central intense lobe surrounded by less intense rings, as reported in Fig. 1.2(a). Its equation is [30]

$$E(r, \phi, z) = A_0 \exp(ik_z z) J_n(k_r r) \exp(\pm in\phi) \tag{1.11}$$

with A_0 the amplitude and where n represents the order of the Bessel function J and ϕ is the azimuthal component. To achieve the Bessel-Gauss equation we consider Eq. (1.11) and a gaussian envelope $\exp(-x^2/\sigma^2)$. Here we report the simpliest, but very important (e.g. for simulations), case of $z = 0$, the complete formula is provided in Ref. [19]:

$$E(r, z = 0) = A_0 J_n(k_r r) \exp(-r^2/\sigma^2) \tag{1.12}$$

with σ^2 the variance of the gaussian curve and smaller the σ, less the number of the Bessel rings, as shown in Fig. 1.12(b).

We note that the BB arises from the interference of plane waves that propagate on a cone [30], i.e. they have all the same transverse wavevector modulus $|k_r|$. This reflects on the Fourier spectrum of the BB that is a ring as shown in Fig. 1.2(c). We have exploited the Fourier property to generate BB in Chapter 3 where we extensively study BBs, both for linear and nonlinear propagation.

1.3 Photorefractive effect

In this Section we consider, among all, the photorefractive effect, that is the principal nonlinear phenomenon that occurs in our crystals. The photorefractive effect is a phenomenon in which a local variation of the index of refraction is induced by an optical field

proportional to the light intensity [31]. The photorefractive effect arises from the charge carriers that are optically generated by a light pattern. The charges then migrate due to drift or diffusion and they generate a space-charge field due to the charge separation. Ultimately, such a field produces a refractive index change via the Pockels' effect [32]. The model that is commonly adopted to describe the photorefractive effect is the Kukhtarev-Vinetskiis model that we will explain in the next Paragraph.

1.3.1 The Kukhtarev-Vinetskiis model

Here we introduce the Kukhtarev-Vinetskiis model (KV model) for the photorefractive effect. Thanks to this model we will get the explicit formula for the induced space-charge field used later to compute the refractive index modulation. The basic elements of the

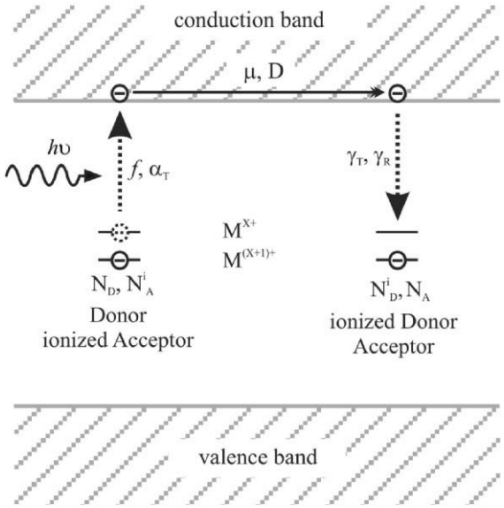

Figure 1.3. Scheme of the band structure of a typical photorefractive material and sketch of the charge carriers separation (recombination) in the illuminated (dark) zone of the crystal (From Ref. [33]).

KV model are reported in Fig. 1.3. We consider a dielectric medium with in-band deep acceptors and photosensitive donor impurities, their density are respectively N_a and N_d and typically $N_d \gg N_a$. When light propagates inside the crystal with a non-uniform intensity distribution $I(\vec{r})$, the charge carriers of the donor sites in the bright areas are excited and, then, they drift and/or diffuse till they recombine in the acceptor sites in the dark area. The result is a spatial charge field that depends on the light pattern [33]. The KV model assumes a constant number of impurities and can be summarized by the rate equation [34]

$$\frac{\partial}{\partial t} N_d^+ = (\beta + sI(\vec{r}))(N_d - N_d^+) - \gamma N_e N_d^+, \tag{1.13}$$

where N_d^+ is the ionized donor density, N_e is the free electron concentration, β is the thermal ionization coefficient, s is the photo-ionization coefficient related to the absorption cross-section and γ electron-donor recombination constant according to Langevin theory [33]. We remind that the Einstein diffusion coefficient is $D = (\mu k_B T)/e_0$ with μ is the carrier mobility, e_0 is the modulus of the elementary charge and $K_B T$ is the thermal energy with k_B the Boltzmann constant. To complete the KV model we include the continuity equation that connects the current density $\vec{J}$ with the average charge density distribution ρ

$$\frac{\partial}{\partial t}\rho + \nabla \cdot \vec{J} = 0, \tag{1.14}$$

with $\vec{J} = e\mu N_e \vec{E} + k_b T \mu \nabla N_e$ and $\rho = e(N_d^+ - N_a - N_e)$ where we have considered that all the acceptors are ionized due to thermal excitation. Finally, the space charge electric field $\vec{E}_{sc}$ can be obtained from the Poisson's equation

$$\nabla \cdot (\varepsilon \vec{E}_{sc}) = \rho. \tag{1.15}$$

In principle, from the above set of equations we can exactly find $\vec{E}_{sc}$ but the system does not have an analytic solution. We, therefore, have to make some simplifications. We consider that two time scales intervene: the charge recombination time τ_r and the dielectric relaxation time τ_d and typically $\tau_r \ll \tau_d$ [5]. This statement, with also the consideration that usually $N_e \ll N_a$ and $\alpha \equiv (N_d - N_a)/N_a \gg 1$, allows us to manage Eq. (1.13) and ρ to get:

$$N_e = \frac{(\beta + sI)}{\gamma}\left[\frac{N_d - p/e}{p/e + N_a}\right], \tag{1.16}$$

and, substituting this to (1.14), we achieve [5]

$$\begin{aligned}\nabla\Bigg[\frac{\gamma}{e\mu s\alpha}\frac{\partial(\varepsilon(0)\vec{E})}{\partial t} + \vec{E}(\beta/s + I)\frac{1 - \frac{\nabla\cdot(\varepsilon(0)\vec{E})}{\alpha N_a e}}{1 + \frac{\nabla\cdot(\varepsilon(0)\vec{E})}{N_a e}} + \\ + \frac{k_B T}{e}\nabla\cdot\left((\beta/s + I)\frac{1 - \frac{\nabla\cdot(\varepsilon(0)\vec{E})}{\alpha N_a e}}{1 + \frac{\nabla\cdot(\varepsilon(0)\vec{E})}{N_a e}}\right)\Bigg] = 0,\end{aligned} \tag{1.17}$$

where we use $\varepsilon(0)$ to underline that the dielectric response is quasi-static for the considered time scales. We can define the dark intensity $I_d \equiv \beta/s$, this term represents the light-independent thermal contribution to the charge ionization. I_d is part of the more general background illumination I_b that takes into account all the secondary intensities that intervene during the process. Since $\alpha \gg 1$ and for the quasi-stationary case ($\partial\vec{E}/\partial t \approx 0$), Eq. (1.17)

reduces to

$$\vec{E}(I_b+I)\frac{1}{1+\frac{\nabla\cdot(\varepsilon\vec{E})}{eN_a}}+\frac{k_bT}{e}\nabla\cdot\left((I_b+I)\frac{1}{1+\frac{\nabla\cdot(\varepsilon\vec{E})}{eN_a}}\right)=g, \tag{1.18}$$

where g is a boundary-condition-dependent constant. For the unbiased case, that is $V=0$, $g=0$ and we get the diffusive electric field $\vec{E}=-\frac{k_bT}{e}\frac{\nabla I}{I_b+I}$. A more complex picture can be obtained considering $g\neq 0$ which means that there is an external bias electric field $E_0\neq 0$. If this occurs, it's hard to manage equations also for the one dimensional case ($\nabla\to\frac{d}{dx}$) and only a perturbative approach is possible. To do this, we introduce the following dimensionless quantities:

$$Y\equiv\frac{|\vec{E}|}{E_0}\qquad Q\equiv\frac{I_b+I}{I_b}\qquad \xi\equiv\frac{x}{x_q}=x\frac{eN_a}{\varepsilon E_0}, \tag{1.19}$$

where x_q is the saturation length. Typically the illuminated region of the crystal l is much smaller than the whole crystal length $L\gg l$, consequently $E_0\simeq V/L$. Thanks to the definitions in (1.19), Eq. (1.18) can be rewritten:

$$\frac{YQ}{1+Y'}+a\left[\frac{Q'}{1+Y'}-\frac{Q}{(1+Y')^2}Y''\right]=G, \tag{1.20}$$

with $a=N_ak_bT/\varepsilon E_0^2$ e $G=g/E_0I_b$ and where the symbol $'$ indicates $d/d\xi$. Assuming $l\gg x_q$, the nonlocal effects are secondary and Eq. (1.20) becomes:

$$Y=\frac{G}{Q}-a\frac{Q'}{Q}+\frac{GY'}{Q}+a\frac{Y''}{1+Y'}, \tag{1.21}$$

in which the first term indicates the local contributions whereas terms with the derivative takes into account the nonlocal contributions. If the first term is appreciably bigger than the others, a saturated Kerr-like nonlinearity formula is recovered. This occurs for our experiments where the beam dimension, that is its Full-Width-at-Half-Maximum (FWHM), is $\Delta x\sim l\sim 10\mu m$. Since the derivatives scale with $\eta=x_q/l\sim 0.01$ whereas a is typically of the order of units [5] we can expand in orders of η. At the zero-th order we have

$$Y^{(0)}=\frac{G}{Q}+o(\eta), \tag{1.22}$$

and, iterating, we get the first order

$$Y^{(1)}=\frac{G}{Q}-a\frac{Q'}{Q}-\frac{Q'}{Q}\left(\frac{G}{Q}\right)^2+o(\eta^2), \tag{1.23}$$

the first term is the so-called screening term and governs the soliton formation. It is a local term since the field in a given position depends only from the optical intensity in the same position. Since typically $G \simeq -1$, this term makes $|\vec{E}| < E_0$ because the charges rearrange to screen the external field, hence its name. The second term is the diffusion field whereas the third term represents a coupling between the diffusion field and the screening field: they both are nonlocal terms and they give rise to asymmetrical contributions that can distort beam propagation, e.g. they cause soliton to bend [35].

1.3.2 Nonlinear variation of the refractive index

At this point we render explicit the nonlinearity enclosed in $\delta n(\vec{r})$ term in Eq. (1.7). In this Thesis, we deal with the electro-optic response as the principal phenomenon that gives rise to the nonlinear variation of the refractive index. The electro-optic response emerges from the coupling between a low-frequency electric field, for us the quasi-static photorefractive $\vec{E}$, and high-frequency electromagnetic field $\vec{E}_{opt}$, i.e. the light beam. The physical mechanism of the coupling can be explained assuming that the material reacts to the presence of $\vec{E}$ changing locally its dielectric properties. This means a variation of the high-frequency polarization that affects also the propagation of $\vec{E}_{opt}$. The more suitable parameter to describe the electro-optic effect is the tensor $\varepsilon = \varepsilon_0 n^2$ or the strictly correlated tensor $1/n^2$ [5]. We define $(1/n^2) = (1/n^2)|_{\vec{E}=0} + \Delta\left(\frac{1}{n^2}\right)$. The tensor variation $\Delta\left(\frac{1}{n^2}\right)$ is therefore caused by the low-frequency $\vec{E}$ via the nonlinear components of the susceptibility of the medium, i.e. its polarization and electric displacement vector. We note that $\Delta\left(\frac{1}{n^2}\right)$ can be considered a local variation if it is compared to the spatial and temporal nonlocality of the charge migration [5]. The E-dependence of $\Delta\left(\frac{1}{n^2}\right)$ can be summarized by the following tensorial expression:

$$\Delta\left(\frac{1}{n^2}\right)_{ij} = r_{ijk}E_k + s_{ijkl}E_kE_l, \tag{1.24}$$

where the sum on repeated indices is assumed and r_{ijk} and s_{ijkl} are the linear and quadratic electro-optic coefficients respectively. In our experiments we essentially deal with only centrosymmetric media, which are all of our crystals, above their Curie point. For centrosymmetric materials, the linear term in (1.24) disappeared and only the quadratic electro-optic response remains with s_{ijkl} that has a strong temperature dependence. In this situation, it is more appropriate to consider polarization $\vec{P}$ instead of $\vec{E}$, so we have

$$\Delta\left(\frac{1}{n^2}\right)_{ij} = g_{ijkl}P_kP_l, \tag{1.25}$$

with g_{ijkl} the element of the electro-optic tensor referred to $\vec{P}$. We point out that g_{ijkl} is temperature independent since all the dependence in temperature is enclosed in ε. From

(1.25) we get the second order variation of the refractive index $\Delta n(E)$

$$\delta n(E) = -\frac{1}{2} n_0^3 g_{eff} \varepsilon_0^2 \left(\varepsilon_r - 1\right)^2 E^2 \tag{1.26}$$

where we have introduced g_{eff} the effective electro-optic parameter. Through the photorefractive effect we have found the expression for $|\vec{E}|$ [Eq. (1.22)] and inserting it in (1.26), we finally obtain:

$$\delta n(I) = -\delta n_0 \frac{1}{\left(1 + I/I_b\right)^2} \tag{1.27}$$

with $\delta n_0 = (1/2) n^3 g_{eff} \varepsilon_0^2 \left(\varepsilon_r - 1\right)^2 E_0^2$. We note that g_{eff} governs the sign of the nonlinearity. We have a focusing (defocusing) nonlinearity for $g_{eff} > 0$ ($g_{eff} < 0$). The ratio I/I_0 indicates that also low powers can produce appreciable effects and it is a consequence of the cumulative response.

1.3.3 Cumulative nature of photorefractive response

Photorefraction is a nonlinearity based on the electro-optic response to a photoinduced space-charge field [5]. The spatial and temporal dynamics of the nonlinearity are dominated by the underlying mechanisms leading to the space-charge distribution, namely photoexcitation/recombination from deep-inband donor-impurities and charge migration through drift and thermal diffusion. Under quite general assumptions, typical of most experimental conditions, and in the accessible 1+1D case, that is, when the optical field depends only on one transverse axis (say the x axis), the photo-excitation/migration/recombination mechanism reaches a steady-state for an electric field that is well approximated by

$$E(x) = \frac{E_0}{1 + \frac{I(x)}{I_d}}, \tag{1.28}$$

where I is the optical intensity and I_d is the dark illumination. The dark illumination is the intensity equivalent to the low residual thermal conductivity in the absence of the optical field. It can be artificially increased illuminating the sample with a second plane-wave optical field, the so-called background illumination. This model is termed the steady-state screening model for photorefractive solitons. For a linear electro-optic response, that is, in conditions in which $\Delta n(E) \propto E$, this leads to the saturated Kerr response $\Delta n = -\Delta n_0 (1 + I/I_s)^{-1}$, with $I_s \equiv I_d$ while, for a quadratic electro-optic response with $\Delta n(E) \propto E^2$, to the saturated response $\Delta n = -\Delta n_0 (1 + I/I_s)^{-2}$. At steady-state, the small fraction of light absorbed by the donor impurities promotes to the conduction band the same number of electrons per unit of time that recombe throughout the sample, while on consequence of the space-charge field, diffusion, and external bias, the net charge migration per unit time in all regions is zero. This steady-state is reached only after a transient regime in which

the space-charge is built-up in time, or accumulated, ultimately to form the steady-state distribution. In this transient, nonlinear response is accumulated, the crystal passing from being a homogeneous system to one with a growing Δn. The build-up process, in conditions in which the crystal is subject to a constant external bias and is illuminated by a constant optical field, involves a complex temporally nonlocal optical response [36].

A good approximation to the transient can be achieved on time scales larger than the electron-recombination time, i.e., in conditions in which the excitation-recombination process has reached locally an equilibrium. Here the transient is governed by the charge relaxation process associated to charge conservation, $\partial_t \rho + \nabla \cdot \mathbf{J} = 0$, where ρ and $\mathbf{J}$ are respectively the charge and current densities. The build-up then obeys

$$t_d \frac{\partial E}{\partial t} + \left(1 + \frac{I}{I_d}\right) E = E_0, \tag{1.29}$$

where t_d is the dielectric relaxation time. The model can be further simplified by considering situations of weak diffraction, that is, conditions in which the build-up is essentially constant along the propagation axis, so that [5]

$$E = E_0 e^{-\left(1+\frac{I}{I_d}\right)\frac{t}{t_d}}. \tag{1.30}$$

For a quadratic electro-optic response, the resulting nonlinearity is

$$\Delta n = -\Delta n_0 e^{-\left(1+\frac{I}{I_d}\right)\frac{2t}{t_d}} \simeq -\Delta n_0 e^{-\frac{2It}{I_d t_d}} \equiv -\Delta n_0 e^{-\frac{I}{I_s(t)}} \tag{1.31}$$

as $I \gg I_d$ in the regions of interest for the propagation and having defined $I_s(t) \equiv I_d t_d / 2t$.

It also possible, under some approximations, the most important of which is neglecting the weak x dependence, to exploit the time dependence of the nonlinearity to achieve the evolution of the light beam along z or, more precisely, along the so-called z_{eff}. The easiest way to derive z_{eff} is to consider the one-dimensional NLSE for the pure Kerr nonlinearity:

$$i\frac{\partial u}{\partial z} + \frac{1}{2}\frac{\partial^2 u}{\partial x^2} + \delta n |u|^2 u = 0. \tag{1.32}$$

In a first approximation, the dependence on time t can be can be factored out from the nonlinear variation of the refractive index $\delta n = f(t)\Delta n(|u|^2)$, where $f(t)$ is a function which depend only on t. The dynamics along each transverse coordinate is thus described by the one-dimensional equation $i\partial_z u + (1/2k)\partial^2_{xx} u + 2\rho|u|^2 u = 0$, where $\rho = (k/n)\Delta n_0 f(t)$ is the single parameter that fixes the relative strength of diffraction and nonlinearity. Introducing the following change of variables, $z_{eff} = \rho z$, $X = \sqrt{2k\rho}x$ and $u(x,z) = \psi(X, z_{eff})$, the equation can be transformed into the dimensionless NLSE: $i\partial_{z_{eff}}\psi + \partial_{XX}\psi + 2|\psi|^2\psi = 0$. An analogous renormalization of the wave equation is widely adopted in nonlinear fiber optics, where the optical power of the input wave is

exploited to mimic the spatial dynamics along the fiber [37]. Rigorously, since the normalization makes dispersive terms slowly varying along the propagation, the approach allows to observe only an effective field evolution.

1.4 Photorefractive screening soliton

Solitons, in general, are localized waves that do not spread in time or space. They are ubiquitous in nature and can be found in several systems such as optical fibers [38, 39], semiconductor microcavities [40], Bose-Einstein condensates [10], water [41], crystals [42] and lattices [3].

From a mathematical point of view, spatial solitons emerge when the diffraction is exactly compensated by the nonlinearity so that the beam is shape-invariant along propagation, namely the z axis. The solution is analytic for pure Kerr nonlinearity and for (1+1D) soliton, that is a soliton with only one transverse dimension, i.e. x-axis, that propagates along another dimension, i.e. z-axis. For (2+1)D soliton, two transverse dimensions, x and y, plus one propagation dimension, a numerical description is possible and the picture requires the taking into account the intrinsic instability of the 2D nonlinearity and the anisotropy of the photorefractive response.

1.4.1 (1+1)D Soliton

As discussed above, (1+1D) admits an analytic solution. The soliton, to preserve the shape of the beam during propagation, needs that the z-dependent factor is confined only in a phase factor. We, therefore, impose the solitonic solution as follows, trying to find the right parameters according to Eq. (1.7),

$$A(x,z) = u(x)e^{i\Gamma z}\sqrt{I_b + I_d} \tag{1.33}$$

with Γ the solitonic propagation constant and, as discussed above, $I_d \ll I_b$. Passing trought the dimensionless quantities [43]

$$\xi \equiv \frac{x}{d} \qquad d \equiv (\pm 2kb)^{-1/2} \qquad b \equiv \frac{k}{n}\left[\frac{1}{2}n^3 g_{eff}\varepsilon_0^2(\varepsilon_r - 1)^2 l\left(\frac{V}{L}\right)^2\right], \tag{1.34}$$

In these assumptions we have included the value of $\delta n(I)$ found before. We get, therefore, the dimensionless equation for centrosymmetric bright screening (1+1)D soliton [44]:

$$\frac{d^2u(\xi)}{d\xi^2} = -\left[\frac{1}{1+u_0^2} - \frac{1}{(1+u(\xi)^2)^2}\right]u(\xi) \tag{1.35}$$

where d is called nonlinear length and $u(\xi)$ is the soliton amplitude $u(x)$ normalized to the square root of the sum of background and dark irradiances. In the $u_0 \ll 1$ limit, the pure Kerr model is recovered, which is integrable, and the solution takes the shape of a hyperbolic secant [43, 45]. This means that for an input gaussian beam some intensity is radiated away to get the right secant-profile [46]. This solution represents an attractor to the system dynamics and it is stable to perturbations [47]. The main beam parameters that characterize the soliton solution are the normalized width $\Delta\xi$ (associated to the FWHM of the imput beam) and the normalized intensity u_0 and the relation between these two is unique [47].

The full problem can be solved integrating numerically Eq. (1.35) and the solution remains a bell-shaped function but it is are neither a Gaussian nor a hyperbolic secant [47]. In this case the relation between $\Delta\xi$ and u_0 is no longer fixed but it is summarized by the so-called existence curve (an example of this is reported in Fig. 1.4).

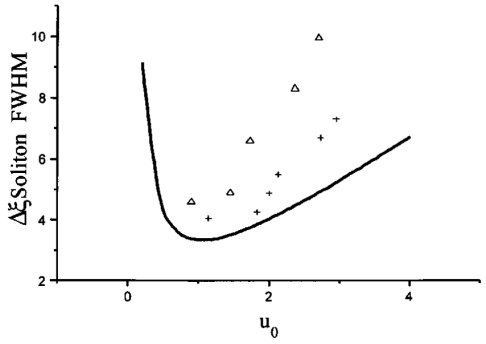

Figure 1.4. Soliton existence curve for photorefractive spatial solitons. The solid line is a theoretical prediction whereas the dots are experimental points. (From Ref. [44]).

1.4.2 Anisotropy in the photorefractive response and (2+1D) soliton

In the simplified 1+1D model, the low-frequency photoinduced electric field E depends only on the transverse x-axis along which the bias field is applied. In a more general situation, as occurs for optical beams that are confined in two transverse directions in the (x, y) plane, the situation is more involved since the external field is delivered by two x-directed plane electrodes while the photoinduced electric field $\mathbf{E}$, obeying the quasi-static irrotational condition $\nabla \times \mathbf{E} \simeq 0$, will also have a y-directed component [5]. In typical experimental conditions, a prevalently x-directed field $\mathbf{E} \simeq E\mathbf{u}_x$ emerges in a manner analogous to what occurs when a dielectric cylinder (the illuminated region) is place in a uniform electric field. As for the polarization charge in the dielectric, here the space-charge forms two lateral lobes along the x-axis. The lobes break the rotational symmetry of the nonlinearity. The lobes, that have been subject of intense debate and study, play a dominant

role when diffraction is strong. In the weakly diffracting case, as the one investigated in this Thesis, they affect the finer details of the nonlinear dynamics.

The anisotropy seems to theoretically to allow, at least, only (2+1D) elliptic soliton and to prohibit the existence of perfectly cylindrical one [48]. In truth, circular soliton are also possible, the key is the lobes suppression that occurs for enough small transverse dimension Δx and Δy [48]. In turn, we have to note that the two-dimensional soliton is unstable for pure Kerr nonlinearity but it is stable for the saturable nonlinearity as our photorefractive one [49].

1.4.3 Solitons interaction

One of the featuring properties of solitons is how they behave after a mutual interaction. This problem is extensively studied for a great variety of different soliton such as dark solitons [50], solitons with different dimensionality [51], solitons carrying an orbital angular momentum [52] and optical spatial bright solitons [53]. Every soliton-soliton interaction is affected by the degree of coherence between them.

Solitons manifest elastic and inelastic collision, so that, despite from their wave nature, they behave like particle. The forces exchanged during interaction can modify the soliton shape and/or direction. It is possible to observe, for low-saturation systems, interpenetration without energy exchange, soliton repulsion and soliton spiraling [54, 55], whereas, for highly saturated media, energy transfer occurs with soliton oscillation and fusion [56]. Among all, for optical bright soliton, coherence regulates the attractive and repulsive forces. In detail, when the two solitons are perfectly in-phase (out-of-phase), an attractive (repulsive) force intervenes [57]. Incoherent collision, instead, simply reproduces the attractive force to a lesser degree [53].

1.5 Modulation Instability

In this Section we brief introduce to Modulation Instability (MI), another phenomenon that is described by NLSE. Then, MI is correlated to solitons and, like the latter, MI can be observed in many fields [58].

Formally this kind of instability emerges when the propagation is affected by a very strong nonlinearity. Like solitons, we are able to analytically treat MI only for (1+1) dimension and for pure Kerr nonlinearity, that represents a limit for our experiment. In these approximations, we recall Eq. (1.32)):

$$i\frac{\partial u}{\partial z} + \frac{1}{2}\frac{\partial^2 u}{\partial x^2} + |u|^2 u = 0. \tag{1.36}$$

A possible solution is given by the continuous plane wave $u(x,z) = u_0 \exp(ipz + iqz)$

with u_0 is a constant and p and q satisfy the dispersion relation $p = -q^2/2 + u_0^2$ [49]. Now we evaluate the stability of this solution against the small perturbation parameters u_1 and v_1. Inserting the perturbed solution $u = (u_0 + u_1 + iv_1)\exp(ipz + iqz)$ in (1.36), we get a system of two couple equations that can be solved imposing the plane wave form $\exp(iKz + iQx)$. The dispersion relation obtained is

$$K = -qQ + Q\left(Q^2/4 - u_0^2\right)^{1/2}, \tag{1.37}$$

and the solution remains stable until $u_0^2 < Q^2/4$. Otherwise for $u_0^2 > Q^2/4$, that is for large self-focusing, the solution becomes unstable and MI emerges [49]. MI is the result of the nonlinear amplification of the small perturbations producing a strong modulation on the principal wave [58].

Experimentally, we observe MI when we propagate the light beam in the photorefractive crystal with self-focusing conditions that exceed those appropriate for the soliton existence, e.g. too high electric field or temperature too close to T_C. We observe 1D wave break up in equally spaced aligned 2D solitons that maintain the overall 1D symmetry as in Fig. 1.5.

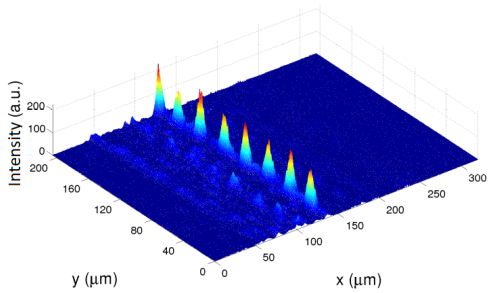

Figure 1.5. Experimental observation of modulation instability in KLTN crystal at $T = T_C + 5K$. The input 1D light beam with $\lambda = 532$ nm and FWHM$= 9$ μm first linearly propagates and spread to FWHM$= 31$ μm after 2.4 mm of crystal length. After the application along the y-axis of an external electric field of 2.5 kV/cm, the beam shrinks and collapse to the MI reported.

Providing further nonlinearity, the behavior changes dramatically and random speckle pattern emerges with the appearance of rogue waves.

1.6 Rogue Waves

In this Section we make a brief introduction of rogue waves, extreme events that can affect several wave-sustaining systems [59]. In particular, our attention is focused on spatial rogue waves that emerge in a photorefractive crystal due to the very strong cumulative nonlinearity larger than that the one that sustains modulation instability .

The first observations of rogue waves were done in ocean [60]. Since they represent a

real danger for vessels, many efforts heve been exercised to understand the phenomenon but with little success due to the intrinsic difficult of observing in nature such rare events [61]. The need of available controllable experimental conditions has driven the search for rogue waves in different systems. In fact, despite they come from different mechanisms, all extreme events respond to an universal statistics and they fulfil the NLSE. The aim is to exploit more affordable systems as test benches for their ocean counterpart and, of these, a very suitable choice are ferroelectric crystals in proximity of the phase-transition due to their large photorefractive nonlinearity and their intrinsic random distribution of ferroelectric domains of different size and orientation [62].

The key signature of the extreme events is the presence of long-tail statistics, which indicates, for spatial experiments, the existence of high intensity peaks in the transverse profile. To clarify this point, we introduce the intensity distribution function, e.g. extrapolating the peak intensities over more than one thousand images. For a gaussian distribution we expect a decay following the function $P(I) = \exp(-I/\bar{I})/\bar{I}$ [63]. Large deviation from gaussian behavior means that the intensity distribution is described by a stretched exponential $P(I) = \exp\left(-cI^b - a)\right)$ with $b < 1$ that indicates the presence of long tail statistics. Furthermore, to recognize a rogue wave, the hydrodynamic criterion is also commonly adopted, that is an extreme event is identified if its intensity exceed at least by a factor of two the mean amplitude of the highest one-third of the detected waves [64]. Both of these criteria are well satisfied by photorefractive ferroelectric crystals close to the Curie point as shown in Fig. 1.6(a). It is relevant the the rogue phenomena disappear for crystals far above the phase transition (Fig. 1.6(b)), demonstrating the relevant role of nonlinearity in extreme events formation. Simulations, indeed, demonstrates that the modulation instability state evolves into more complex state with random quasi-soliton fusion [61].

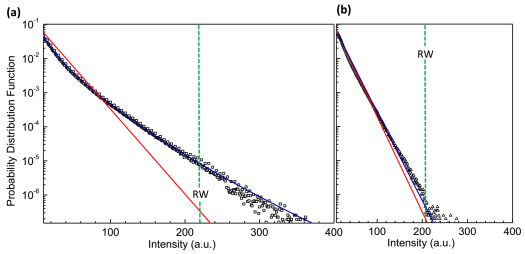

Figure 1.6. Rogue wave in nanodisorder ferroelectric crystal for (a) large nonlinearity for $T \sim T_C$ and (b) small nonlinearity for $T > T_C$. Solid red line represents the gaussian P(I), green dashed line indicates the limit of hydrodynamic criterion and squares and triangles are experimental points. The blue lines are fit curve with stretch exponential with (a) $b = 0.65$ and (b) $b = 0.99$. (Adapted from Ref. [61]).

In the next chapters we will discuss again extreme events in nonlinear media. We will study the special case of rogue waves that produce an evidence of a Fermi-Pasta-Ulam-Tsingou recurrence and, ultimately, we will be able to predict their appearance.

1.7 Numerical solution of the NLSE

In this Section we discuss briefly a numerical method to solve the NLSE (1.7) and to obtain the evolution of a given light beam into a nonlinear medium. The method is the so-called Beam Propagation Method (BPM) and it is a kind of Split-Step Fourier Method [65, 66].

To derive the BPM we can rewrite the one-dimensional NLSE in the compact form:

$$\frac{\partial}{\partial z}A = (\hat{D} + \hat{N})A, \tag{1.38}$$

where $\hat{D} = -\frac{i}{2k}\frac{\partial^2}{\partial x^2}$ e $\hat{N} = -i\frac{k}{n_0}\delta n(x)$ are the diffraction and the nonlinear inhomogeneities operators respectively. Eq. (1.38) can be solved formally and solution is expressed in the recursive mode:

$$A(x, z + l) = e^{l(\hat{D}+\hat{N})}A(x, z), \tag{1.39}$$

where l is the single evolution step. Generally, the dispersion and nonlinearity effects are not separable because they act together all along the propagation in the medium and the commutator $\left[\hat{D}, \hat{N}\right] \neq 0$.

The BPM provides an approximate solution of the NLSE applying separately $\hat{D}$ and $\hat{N}$ for each step of l length. The approximation is good if $l \ll L$ the whole propagation and if the dynamics along z is sufficiently slow. In these hypotheses we can apply the Trotter identity[1] [67] on Eq. (1.39) and we obtain:

$$A(x, z + l) = e^{\frac{l}{2}\hat{D}}e^{l\hat{N}}e^{\frac{l}{2}\hat{D}}A(x, z) + \mathcal{O}(l^2). \tag{1.40}$$

This equation gives the recipe to built an efficient algorithm. We apply cyclically the operators $\hat{D}$ and $\hat{N}$ on the initial state to get the evolution. We can do this because the analytical effects of $\hat{D}$ and $\hat{N}$ are known.

Specifically, to take into account $\hat{D}$, we must move in the Fourier space. Neglecting $\hat{N}$, we have in direct space $\frac{\partial}{\partial z}A = \frac{\partial^2}{\partial x^2}A$ that corresponds in Fourier space of:

$$\frac{\partial}{\partial z}A = ik_x^2 A, \tag{1.41}$$

and the solution of this equation is $A(k_x, z + \Delta z) = A(k_x, z)e^{\frac{i}{2}k_x\Delta z}$. To explicit the effect

[1] Given two non-commuting operators A and B, we have:

$$e^{(A+B)} = \lim_{S\to\infty}\left(e^{A/2S}e^{B/S}e^{B/2S}\right)^S \simeq \left(e^{A/2S}e^{B/S}e^{B/2S}\right)^S e^{\mathcal{O}(1/S^2)}.$$

of $\hat{D}$ in direct space, we can simply perform the inverse Fourier transform and we obtain:

$$A(x, z + \Delta z) = \int_{\mathbb{R}} A(k_x, z) e^{\frac{i}{2} k_x \Delta z} e^{i k_x x} dk_x. \tag{1.42}$$

For $\hat{N}$ the derivation is easier. In fact, neglecting $\hat{D}$, we have $\frac{\partial}{\partial z} A = -i \frac{k}{n_0} \delta n(x) A$ whose solution is directly $A(x, z + \Delta z) = A(x, z) e^{-i \frac{k}{n_0} \delta n(x) \Delta z}$.

1.7.1 BPM simulation of (1+1D) soliton

In this Paragraph we report a significant example of the using the BPM to achieve the soliton propagation in a self-focusing medium which follows the saturable Kerr nonlinearity $\delta n(I) = -\delta n_0 \frac{1}{(1+I/I_b)^2}$.

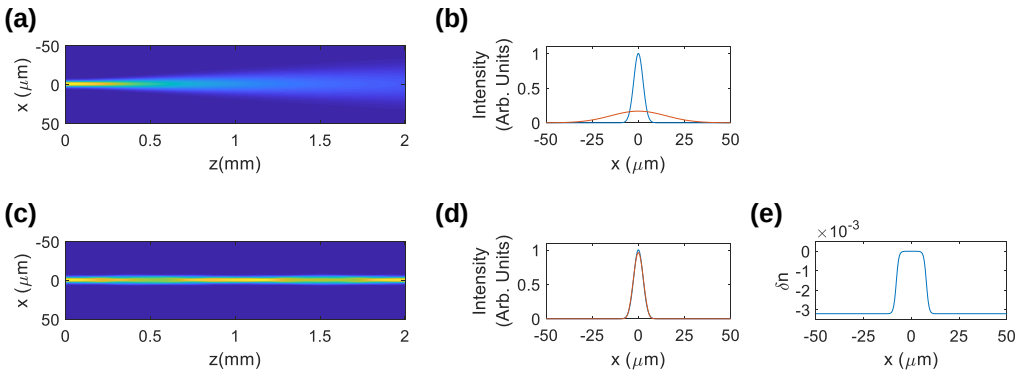

Figure 1.7. Linear and non linear propagation in 2 mm photorefractive medium of an input gaussian beam with FWHM= 6 μm. (a) Linear propagation in the $x - z$ plane and (b) profiles at $z = 0$ (blu line) and $z = 2$ mm (orange line). The diffraction produces a beam with FWHM=34 μm. (c) Soliton propagation in the $x - z$ plane and (d) profiles at $z = 0$ (blu line) and $z = 2$ mm (orange line). (e) Refractive index variation δn at $z = 2$ mm. The other parameters of the simulations are: $\lambda = 532$ nm, $n_0 = 2.3$, $I/I_b = 60$, $\delta n_0 = 10^{-4}$, $\epsilon_r = 1.3 \times 10^4$, $g_{eff} = 0.16$, $E_0 = 2.4$ kV/cm.

First, we study the linear propagation of a gaussian beam with FWHM= 6 μm along $z = 2$ mm medium with $n_0 = 2.3$. The resulting propagation is shown in Fig. 1.7(a). From Fig. 1.7(b) we can appreciate the amount of the diffraction: the beam spreads up to a FWHM=34 μm.

The introduction of the nonlinearity of Eq. (1.27), induced by the application of $E_0 = 2.4$ kV/cm, sustains the solitary propagation of Fig. 1.7(c) without appreciable changing in the beam profile between the input and the output of the medium [Fig. 1.7(d)]. Thanks to the BPM we can also study the shape of the nonlinear refraction index variation δn that we report in Fig. 1.7(e). We see that there is a global lowering of the refractive index except from the area illuminated by the beam. The net effect is to create a sort of waveguide, that is

a zone with a refractive index upper than outside, and this cause the beam to be guided and, ultimately, to not diffract.

Chapter 2

Observation of the exact dynamics of the Fermi-Pasta-Ulam-Tsingou recurrence

Fermi-Pasta-Ulam-Tsingou[1] recurrence (FPUT) is one of the most important problems in nonlinear physics [69]. In this Chapter we report our experiments that allowed us to observe several spatial recurrences. The recurrence period and phase-shift are found in remarkable agreement with the exact recurrent solution of the Nonlinear Schröedinger Equation provided by Grinevich and Santini [70, 71], whereas the recurrent behavior disappears as integrability is lost. This identify the origin of the recurrence in the integrability of the underlying dynamics and allows us to reconstruct the exact initial condition of the system after several return cycles.

2.1 Integrability and the FPUT problem

The FPUT problem was discovered by Fermi in collaboration with Pasta, Ulam and Tsingou two years before the publication of their famous paper [72], occurred one year after Fermi's death. Fermi didn't understand why a chain of weakly anharmonic oscillators, with a single-mode initial condition, doesn't exhibit thermalization, also after a long time scale[2]. They discovered that the system, instead of converging to the equilibrium, that is the energy equipartition on all the modes, returns, almost periodically, to its initial state. Indeed, nonlinear interaction in a multimodal system introduces coupling between its linear modes. When a reduced set of modes is initially excited, the energy exchange associated to this coupling provides the route to reach thermodynamic equilibrium. This process towards

[1] The contribution of Mary Tsingou was officially recognized only in 2008 [68].

[2] In 1955 they believed that their time scale was long, referring to their computational power. Nowadays their time scale is generally considered short.

thermalization is irreversible but they showed that it can present local reversibility, with the appearence of specific quasi-periodic states [69, 73, 74].

An approach to understand the physical mechanism underlying the phenomenon rests on the quasi-integrability of the system [75–78]. This property implies the existence of a time scale for which the FPUT dynamics is essentially integrable. In fact, for integrable models, pure thermalization is never reached since normal modes are phase-locked and not free to resonantly interact and spread energy over the entire spectrum [76]. Consistently, certain integrable systems support breathers; their phase space presents homoclinic orbits connecting unstable solutions, so that trajectories starting in proximity of these unstable points can return close to the original state. The key role of integrability explains why the FPUT recurrence has eluded in-depth experimental investigations. Specifically, while in numerical studies the thermalization time was too large to be initially identified, quite the opposite issue arises in experiments: in open systems involving several interacting modes recurrences to the initial state are not normally reported. In fact, due to the effect of intrinsic dissipation or input noise amplification [79], a natural process rarely is integrable and preserves multiple returns. In fact, observations in Hamiltonian systems have so far been limited to one or two return cycles [80]. Evidences of the recurrence of states have been reported in deep water waves [80], surface gravity waves [81], magnetic rings [82], optical microresonators [83] and optical fibers [84–86]. In spite of these efforts, how the specific initial condition determines the properties of the recurrent behavior remains a fundamental point that has never found experimental validation. An important attempt in this direction has been reported very recently in loss-compensated optical fibers [86], where, however, the tailored amplification allows the system just to mimic the return cycles that would have its non-dissipative counterpart. In this setting, among the many recurrent behaviors expected varying the input state, only the two types with opposite symmetry has been observed and related to separate families of orbits in phase space [86]. The observation of the FPUT dynamics as predicted by exact solutions of an underlying integrable model remains an open challenge.

2.2 Exact recurrences in the nonlinear Schrödinger equation

In this section we resume the theory of Santini and Grinevich about the recurrence of rogue waves. We start our analysis by recalling the NonLinear Schrödinger Equation (NLSE) (Eq. 1.7 of Chapter 1) and, more specifically, we use its integrable form, i.e. for pure Kerr effect:

$$i\partial_z\psi + \partial_{xx}\psi + 2|\psi|^2\psi = 0. \tag{2.1}$$

This equation is associated to an universal model describing the propagation of a quasi-monochromatic field $\psi(x,z)$ in a weakly nonlinear medium [87]. Exact solutions of Eq. (2.1) corresponding to perturbations of the constant background wave have recently attracted considerable attention in hydrodynamics and optics [39, 41, 88–92], in particular as they describe the dynamics of the Modulation Instability (MI) and may be relevant in explaining the formation of extreme amplitude waves (rogue waves) [59, 61, 93–96]. On the other hand, the NLSE naturally arises as the continuous limit (infinite number of modes) for the dynamics of a chain of anharmonic oscillators coupled by a cubic nonlinearity, the so called β-FPUT model [97, 98]. In this framework, the problem of finding the time scale of the recurrence as a function of the specific input condition has been elusive up to recently. The analytic description of the recurrence for an initially-perturbed background field of finite length with a single unstable mode has been reported by Grinevich and Santini using the finite-gap method or matched asymptotic expansions [70, 71]. Theory points out a variety of phase-shifted recurrences closely determined by the phase and amplitude of the input condition. In particular, considering the single-mode perturbed input field

$$\psi_0(x) = 1 + \varepsilon \left(c_1 e^{ikx} + c_2 e^{-ikx} \right), \tag{2.2}$$

with complex amplitudes c_1 and c_2 and $\varepsilon \ll 1$, we expect the recurrent growth of a coherent structure of the Akhmediev type (x-periodic) and its recurrent decay to the initial state. The first-appearance time or recurrence partial-period of this large-amplitude wave is predicted to as [70, 71]

$$Z_1 = \frac{1}{\sigma_k} \log \left(\frac{\sigma_k^2}{2\varepsilon|\alpha|} \right), \tag{2.3}$$

where $\sigma_k = k\sqrt{4-k^2}$ is the growth rate of the input unstable mode with wavevector k and $\alpha = c_1^* - c_2 \exp(2i\vartheta)$ with $\vartheta = \arccos(k/2)$. The multiple recurrence of the field to the initial condition corresponds to periodic orbits close to the homoclinic orbit described by the well-known Akhmediev breather (AB) exact solution of the NLSE [99]. In fact, in the m-th recurrent nonlinear stage of the dynamics ($m \geq 1$), the field is described by the AB soliton, which, at its maximum, reads as

$$\psi(x, Z_m) = e^{i\xi_m} \frac{\cos(2\vartheta) + \sin(\vartheta)\cos[k(x - X_m)]}{1 - \sin(\vartheta)\cos[k(x - X_m)]} + O(\varepsilon), \tag{2.4}$$

where ξ_m, Z_m and X_m are parameters related to the input condition through the elementary functions [70, 71]

$$\begin{aligned} Z_m &= Z_1 + (m-1)\frac{2}{\sigma_k}\log\left(\frac{\sigma_k^2}{2\varepsilon\sqrt{|\alpha\beta|}}\right), m \geq 1 \\ X_m &= \frac{\arg(\alpha) - \vartheta + \pi/2}{k} + (m-1)\frac{\arg(\alpha\beta)}{k}, \\ \xi_m &= 2Z_m + 2(2m-1)\vartheta, \end{aligned} \tag{2.5}$$

with $\beta = c_2^* - \exp(-2i\vartheta)c_1$. Altough solution of the Akhmediev type have been observed and connected to recurrent behaviors in different settings [80, 86], experimental demonstration of Eq. (2.3), which forms the basis for the FPUT dynamics in a broad range of systems, is lacking. In other words, the way in which these exact recurrent solutions can have physical relevance is an open question.

2.3 Numerical Simulations

In this Section we show the FPU recurrence numerically, evolving the state (2.2) through the pure Kerr NLSE via the BPM (explained in Chapter 1). To simplify the analysis we

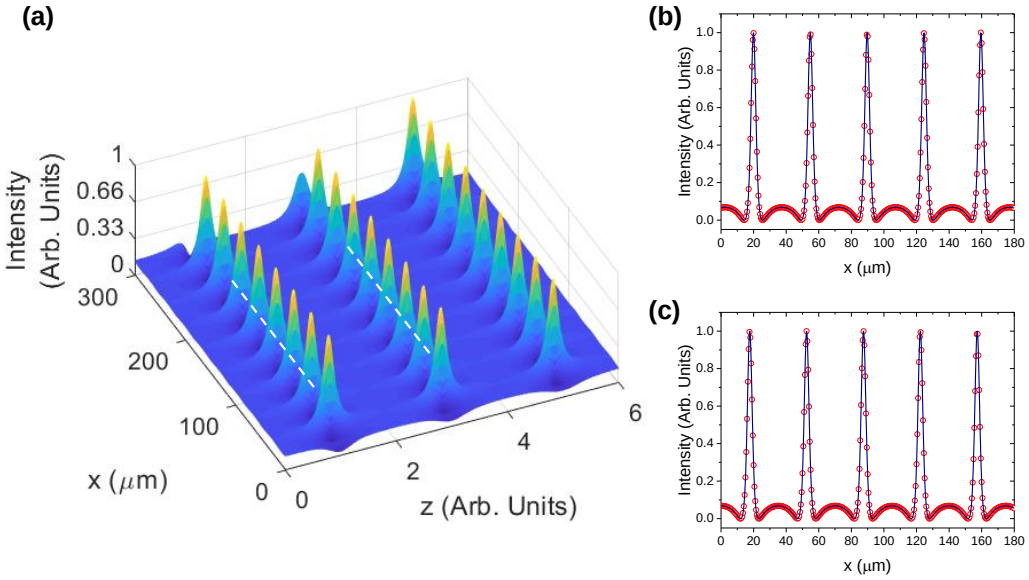

Figure 2.1. Numerical simulation of the FPUT recurrence. (a) Evolution of the symmetric state $\psi_0(x) = 1 + \varepsilon\left(|c|e^{ikx} - |c|e^{-ikx}\right)$ with $k = 0.18\ \mu\text{m}^{-1}$ with the appearence of three FPUT recurrences. Each rogue has an Akhmediev breather profile as analyzed along the white dashed lines for the first one (b) and the second one (c). Points are the numerical values whereas the solid lines are fit curves according with Eq. (2.4) (see text).

limit our study to the symmetric perturbation, that is for $|c_1| = |c_2|$ and arg(c_2)-arg(c_1)=-1,

coherently with the experiments below. In Fig. 2.1(a) we report the case of $k = 0.18\ \mu\text{m}^{-1}$. Three FPUT recurrences are clearly evident and their intensity profiles fit well with the squared AB formula (2.4) (details of the fitting method are reported in Paragraph 2.5.1). The profiles and the fit curves are shown in Figs. 2.1(b),(c) (the profile of the third recurrence is not reported). The fit parameters are for both $\theta = 1.019$ and $k = 0.18$, as expected. We note that $X_1 = 19.89$ whereas $X_2 = 17.63$, this indicates that there is a slight shift of the recurrences along the x-axis, as predicted by the theory and also visible in Fig. 2.1(a).

We point out that the simulation are carried out for an arbitrary long propagation. In our experiments, instead, we are limited by the fixed length of the crystal but, as showed below, we are able to overcome this fact rescaling units exploiting the time-dependence of the nonlinearity.

2.4 Experimental Setup

To investigate FPUT recurrences in optical dynamics, we consider the propagation of nonlinear optical waves in a photorefractive crystal. The wavectors of the optical field constitutes the linear modes which are coupled by nonlinear propagation. The transverse crystal size fixes the finite length of the input wave, a condition ensuring a countable set of Fourier modes and a finite recurrence period. Under specific conditions, the system can be described by the NLSE in the spatial domain, with the propagation direction acting as evolution coordinate [100]. The experimental geometry of our setup is shown in Fig. 2.2(a). In detail, a y-polarized optical beam at wavelength $\lambda = 532$ nm from a continuous 30 mW Nd:YAG laser source is split and recombined in the xz-plane to form a symmetric three-wave interferometer, with the two arms having opposite wavevectors and forming an angle θ with the 300 μW central beam. The interference pattern is focused by a cylindrical lens down to a quasi-one-dimensional beam with waist $\omega_0 = 15\ \mu$m along the y-direction and periodically-modulated along the x-direction [inset in Fig. 2.2(a)]. This pattern well satisfy our request of one-dimensional background wave with a coherent single-mode perturbation. It follows that along the transverse x-direction, the relevant one for the dynamics under study, the resulting optical field is $E = E_0 + E_1 e^{i\phi_1} e^{ikx} + E_2 e^{i\phi_2} e^{-ikx}$, with $k = 2\pi \tan(\theta)/\lambda$. The optical intensity normalized to the background I/I_0 ($I_0 = |E_0|^2$) can be expressed as $I/I_0 \equiv |\psi_0(x)|^2 = 1 + A\cos(kx + B)$, which directly maps the initial condition in Eq. (2.2) with $A = 2\varepsilon|\gamma|$, $B = \arg(\gamma)$ and $\gamma = c_1 + c_2^*$. With respect to the experimentally accessible parameters, the amplitude and phase of the perturbation read as $A = 2\sqrt{[I_1 + I_2 + 2\sqrt{I_1}\sqrt{I_2}\cos(\phi_1 + \phi_2)]/I_0}$ and $\tan(B) = (\sqrt{I_1}\sin\phi_1 - \sqrt{I_2}\sin\phi_2)/(\sqrt{I_1}\cos\phi_1 + \sqrt{I_2}\cos\phi_2)$. Therefore, the spatial frequency of the perturbation k can be varied acting on the geometrical angle θ in between the arms of the interferometer, whereas their optical power and phase delay $\phi \equiv \phi_1 + \phi_2 = \arg(c_1) + \arg(c_2)$

set, respectively, the amplitude and phase of the single-mode [Fig. 2.2(b-c)]. The fringe visibility is thus maximum for $\phi_1+\phi_2=0$ and minimum for $\phi_1+\phi_2=\pi$. In the symmetric case $I_1 \simeq I_2$, we have $B \simeq (\phi_1-\phi_2)/2$.

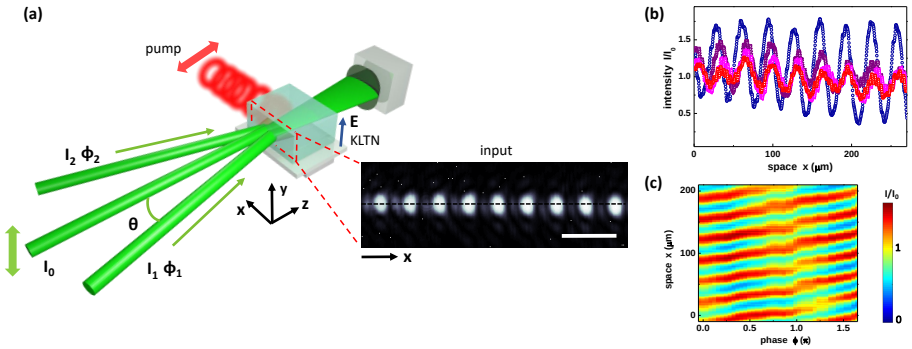

Figure 2.2. Experimental setup. (a) Sketch for the symmetric three-wave interferometric scheme used to generate a quasi-one-dimensional background wave with a single-mode perturbation that propagates in a pumped photorefractive KLTN cystal. The inset shows an example of the detected input intensity distribution (scale bar is 50 μm). (b) Input intensity x-profiles normalized to the background for different amplitudes of the harmonic perturbation ($k=0.019$ μm^{-1}). (c) Phase control of the initial condition: intensity distribution varying the relative phase ϕ between the interfering waves.

The copropagating waves are launched into an optical quality specimen of $2.1^{(x)} \times 1.9^{(y)} \times 2.5^{(z)}$ mm. The crystal, a potassium-lithium-tantalate-niobate (KLTN), is a solid solution of $K_{0.964}Li_{0.036}Ta_{0.60}Nb_{0.40}O_3$ with Cu and V impurities. It exhibits a ferroelectric phase transition at the Curie temperature $T_C=284$ K. Nonlinear light dynamics are studied in the paraelectric phase at $T=T_C+8$ K, a condition ensuring a large nonlinear response and a negligible effect of small-scale disorder [101]. The time-dependent photorefractive response sets in when an external bias field E is applied along y (voltage $V=500$ V). To have a so-called Kerr-like (cubic) nonlinearity from the photorefractive effect, the crystal is continuously pumped with an x-polarized 15mW laser at $\lambda=633$ nm. The pump does not interact with the principal beams propagating along the z-axis and only constitutes a reference intensity larger than the single-mode perturbed background wave. The spatial intensity distribution is measured at the crystal output as a function of the exposure time by means of an high-resolution imaging system composed by an objective lens ($NA=0.5$) and a CCD camera at 15 Hz.

Since the propagation length cannot be varied in our setting and the intensity profile inside the crystal cannot be directly measured [66], nonlinear evolution of the input field is observed by the time the crystal is exposed to the copropagating light beams. The method relies on the nature of the photorefractive nonlinearity, that is noninstantaneous and accumulates in time as a photogenerated space-charge field builds up. Since the process

occurs on a slow time scale compared to wave propagation through the medium, this implies a nonlinear coefficient that depends parametrically on the exposure time. Due to the invariant properties of the wave equation, observations of the intensity distribution at the crystal output at different times correspond to beam propagation for increasing effective distances z_{eff} (see Section 1.3.3 of Chapter 1). This is equivalent to study the dynamics varying the strength of the nonlinearity through an external parameter, in close analogy with FPUT investigations in optical fibers where changes of the input optical power are exploited [84]. Recalling Chapter 1, we can factorize $\delta n = f(t)\Delta n(|A|^2)$. In our system, that is the focusing photorefractive nonlinearity in centrosymmetric media, we have $\delta n = f(t)\Delta n_0/(1+|A|^2)^2$, where Δn_0 include the quadratic electro-optic effect. For $|A|^2 \ll 1$, as occurs in our externally-pumped configuration, we obtain the Kerr-like regime where $\Delta n(|A|^2) \approx 2\Delta n_0|A|^2$, apart from a constant shift. As mentioned above, the evolution in z_{eff} is studied at a fixed value of z (the crystal output) varying the exposure time t. In fact, experimental results obtained in similar photorefractive KTN crystals have verified that the average index change grows and saturates according to $f(t) = 1 - \exp(-t/\tau)$ [102]. The time dependence is well defined through the saturation time τ once the input beam intensity, applied voltage and temperature have been fixed. Using this relation with the measured $\tau \approx 80$ s, observations at the crystal output are rescaled as a function of the effective distance Z. The nonlinear response function $f(t)$ represents the main limitation of the technique in reconstructing the spatial dynamics from time-resolved measurements. Specifically, $f(t)$ is independent of the local intensity only in a first approximation, a fact that affects the accuracy of the obtained field evolution. When the intensity distribution presents large intensity variations or strong spatial inhomogeneities, intensity-dependent corrections to $f(t)$ should be taken into account to have a quantitative reconstruction along the evolution coordinate. These high-order terms are nonlocal in space and time; their main effect is that the time evolution of high-intensity regions slows down [5]. Therefore, in the present case, the method is particularly accurate up to a distance Z_1 (first-appearance time). Small longitudinal deformations appear at longer evolution scales [Fig. 2.3(a-b)] and the relative distance between the observed AB structures can not be accurately evaluated. This fact explains the discrepancy with theory for the value of the recurrent period when measured through the Z-distance between returning intensity maxima. In particular, the recurrent AB seems to appear at an effective distance that is always shorter than expected according to theoretical predictions. Moreover, as the nonlinearity finally saturates in time, the field dynamics at large Z departs from that of the integrable model and evolution towards thermalization is observed.

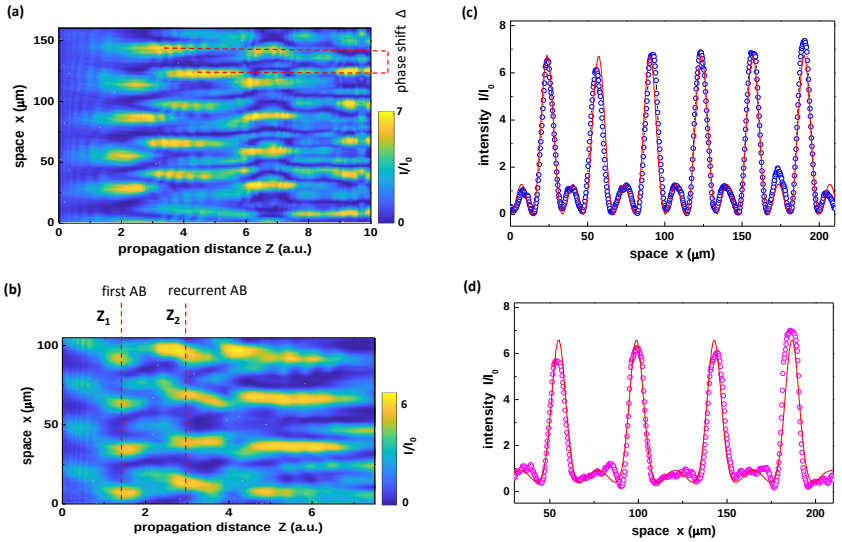

Figure 2.3. Observation of the FPUT recurrence of Akhmediev breathers. (a-b) Evolution of the detected spatial intensity distributions for (a) $k = 0.019$ μm^{-1}, $A = 0.3$ and (b) $k = 0.030$ μm^{-1}, $A = 0.5$. Both observations show the appearance of a high-intensity pattern at a distance Z_1 (red dotted line), its return to the initial state and multiple recurrences with a spatial phase-shift that depends on the experimentally assigned input condition ($\Delta \approx 15$ μm, 2 μm in (a) and (b), respectively). (c-d) Intensity x-profile measured at the first appearance of the localized waves (circles) fitted with the AB profile at its maximum (red line, Eq. (4)) for (c) $k = 0.021$ μm^{-1} and (d) $k = 0.014$ μm^{-1}.

2.5 Experimental Results

The spatial intensity distribution $I(x)/I_0$ detected as a function of the evolution coordinate Z is reported in Fig. 2.3(a) for $k = 0.019$ μm^{-1}, $A = 0.3$. We observe the input perturbation grow on the modulationally unstable background forming a train of large-amplitude localized waves, which decays back to an almost constant background and recurrently reappear from it. The set of linear modes undergoes several return cycles in which energy flows back and forth, passing from the zero and first mode (the initial perturbation) to a spectral distribution in which all the modes are excited, the signature of the FPUT dynamics [103].

At variance with classical and quantum beating, such as Rabi cycles in two-level quantum systems [104], here energy oscillations involve several modes and occur without any driving field. At each cycle the whole field distribution is spatially shifted by an amount Δ, a phenomenon also referred to as broken symmetry of FPUT recurrence [80, 86]. Although a similar phase-shift has been associated theoretically to the specific gain of the seeded wavevector [105] and the effect of dissipation [106], we show hereafter that it results from the sensitivity of the dynamics to the specific initial phase. This phase-shift, as well as the recurrence period detected through the first appearance distance Z_1 of the high-intensity pattern, strongly changes as the input perturbation is varied. For instance, in Fig. 2.3(b) we report the observed FPUT recurrence for $k = 0.030$ μm^{-1} and $A = 0.5$, where no significant phase-shift occurs. The recurrent behavior can be directly related to the excitation from the single-mode input perturbation of an orbit close to the Akhmediev breather [71]. As shown in Fig. 2.3(c-d), the periodic intensity profile detected along x when the amplified modes reach their first maximum is well fitted by the Akhmediev breather solution of the NLSE at its maximum [Eq. (2.4)]. Consistently, throughout the manuscript we refer to these localized states to as AB. The finding of exact solutions indicates that our system remains close to the integrable regime on these effective distances, that is, it can be properly described by the NLSE.

We study the FPUT recurrence by varying the single-mode input condition. Fixing the initial phase of the field through a careful maximization of fringe visibility, we first analyze the recurrence partial-period varying the amplitude of the perturbation A. Results in Fig. 2.4(a) show that the first appearance of the AB occurs at a distance that decrease as the single-mode amplitude becomes larger. An analogous behavior is observed for the recurrent breather (second appearance). In remarkable agreement with the analytic solution of the NLSE, the observed scaling follows Eq. (2.3), which predicts $Z_1 \propto \log(1/A)$. For modes k falling in proximity of the maximum gain, the recurrence period only weakly depends on the input wavevector [Fig. 2.4(b)], a feature well captured by Eq. (2.3) through σ_k. More importantly, the main effect on the recurrence is found to be related to the phase of the initial condition. To investigate its role, we balance the optical power in the interferometer

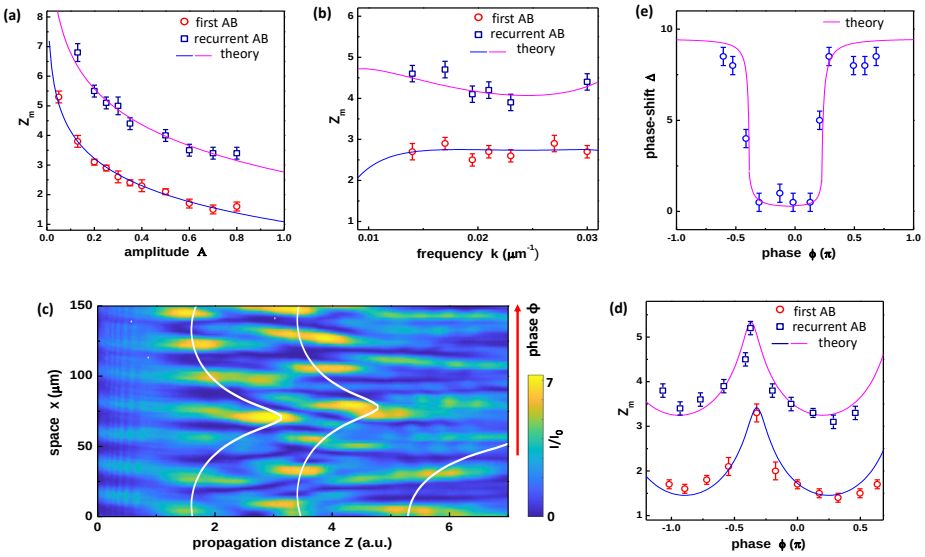

Figure 2.4. Properties of the recurrent behavior. Recurrence partial-period measured (dots) varying (a) the amplitude of the input excitation ($k = 0.023\ \mu\text{m}^{-1}$) and (b) the frequency of the input mode ($A = 0.3$). (c) Evolving intensity distribution detected for an input phase that varies along x ($k = 0.030\ \mu\text{m}^{-1}$). White lines interpolates local maxima and serve as guides. (d) Z_m as a function of the initial dephasing. Blue and magenta lines in (a-d) are fitting functions according with Eq. (2.3). (e) Recurrence phase-shift varying the input phase: measured sharp transitions (dots) and predicted behavior (line).

arms ($I_1 \approx I_2$) and introduce a slight tilt in one of them, so as to have a perturbation with a phase that depends on the spatial point. The observed FPUT dynamics is reported in Fig. 2.4(c); the AB appears and recurs phase-shifted at a propagation distance that varies along the transverse coordinate. As a function of the input phase delay, Z_1 presents an oscillation having a sharp maximum for $\phi \simeq -0.3\pi$ and a broad minimum for $\phi \simeq -0.9\pi, 0.35\pi$ [Fig. 2.4(d)]. This characteristic behavior, which reflects phase-dynamics in each return cycle, is in remarkable agreement with the NLSE theory and represents its main validation. In fact, in Eq. (2.3) the recurrent semi-period critically depends on $|\alpha|$, a quantity that oscillates with the relative phase of the complex amplitudes c_1 and c_2 forming the initial perturbation. Specifically, in the case of symmetric perturbations ($I_1 \approx I_2$), theory predict a sharp maximum in Z_1 for $\phi \simeq -2\vartheta$; from Fig. 2.4(d) we can thus obtain the theoretical parameter $\vartheta \simeq 0.15$, consistent with the one extracted from the AB profile. Moreover, a sharp transition is expected for the recurrent phase-shift as a function of the input phases [86]. In Fig. 2.4(e) we report the measured shift, which sharply passes from $\Delta \approx 0$ to $\Delta \approx 1/2k$ varying the phase delay, a behavior that well agrees with the theoretical condition $\cos(\phi) \gtrless \cos(2\vartheta)$. These effects indicate that the coherence of the field is maintained as energy is exchanged between different modes: phase-locking dominates the nonlinear stage of the unstable dynamics and thermalization slows down.

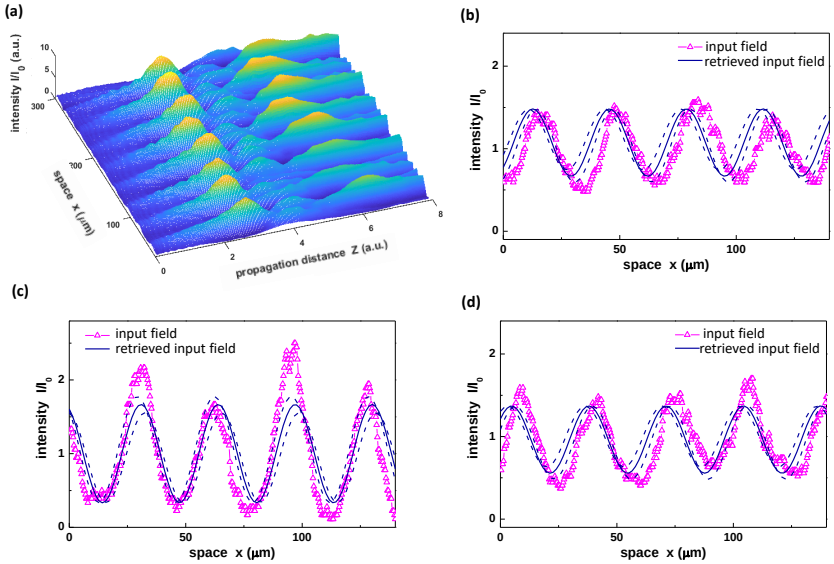

Figure 2.5. Inverse problem. (a) Experimental observation used to test the predictability of the input state from the recurrent dynamics ($k = 0.021\ \mu\text{m}^{-1}$). Measured (dots) and retrieved (line) input field for different initial phases: (b) $\phi \simeq \pi$, (c) $\phi \simeq 0$ and (d) $\phi \simeq 0.3\pi$. Dashed lines indicates the uncertainty of the retrieved condition.

The deterministic properties of the return cycle imply its predictability once the input condition is completely known, and vice-versa. To investigate this integrable character in

experimental conditions we retrieve the actual initial state from the features exhibited by the recurrent stage (inverse problem). We consider the FPUT dynamics reported in Fig. 2.5(a). The phase B of the input perturbation is obtained taking into account that the periodic transverse position X_1 at which the first AB has its maximum intensity strictly depends on ϕ, as well as the specific shift Δ characterizing the return cycle. In fact, according to Eq. (2.5)), we have $X_1 = (\arg(\alpha) - \vartheta + \pi/2)/k$. At each recurrent cycle the breather solution is transversely shifted by $\Delta = \arg(\alpha\beta)/k$. Therefore, when $\vartheta \approx 0$, $\arg\beta \simeq k(\Delta - X_1) + \pi/2$ and the phase of the input excitation can be evaluated as

$$B = \arg(\gamma) \approx k(\Delta - X_1) - \vartheta, \tag{2.6}$$

where k and ϑ are extracted from the first AB profile. The amplitude of the single-mode follows from the observed Z_1 through the scaling in Fig. 2.4(a). As shown in Fig. 2.5(b-d) for different initial dephasing, the field retrieved using this procedure agrees well with the experimental input condition that generates the recurrence: the non-equilibrium dynamics can be accurately traced on the basis of the underlying integrable model.

2.5.1 Analysis of the recurrence

The intensity traces detected as the normalized distribution $I/I_0 = |\psi|^2$ reaches their maxima are compared with the Akhmediev breather profile in Eq. (2.4). In fitting the data in Fig. 2(c-d), the coefficients ξ_m, k, ϑ and X_m are considered as bounded parameters. The detected recurrence partial-period is analyzed according to Eq. (2.3); for the measurements in Fig. 3(a) we consider $a\log(b/\varepsilon)$ as a fitting function, with a and b free parameters. In Fig. 2.4(b) we use $a\log(b(k\sqrt{K_{max}^2 - k^2})^2)/k\sqrt{K_{max}^2 - k^2}$, where a and b are free parameters and $K_{max} \approx 0.03$ μm^{-1} is the wavevector with maximum gain that we independently measure from spontaneous MI of the background wave. In Fig. 2.4(d) the detected Z_m is compared to $\log(a/\sqrt{c_1^2 + c_2^2 - 2c_1c_2\cos(\phi + b)})$, being a, b, c_1 and c_2 bounded parameters. In this case, it is interesting to note that the fitting procedure returns $c_1 \simeq c_2$, that is, a balanced condition for the interferometer arms as experimentally settled. In Fig. 2.4(e) the fitting functions are $a + b/[\cos(\phi) - \cos(c)]$, as predicted for the symmetric case $|c_1| \approx |c_2|$. As for the retrieval of the input perturbation, from the observed recurrences in Fig. 2.5(a-b) we measure, for example, $k = 0.021$ μm^{-1}, $\Delta = 1 \pm 1$ μm, $Z_1' = 2.6 \pm 0.1$, $\vartheta = 0.1$ which, for $X_1 = 208$ μm, gives $B = -40.1 \pm 0.3$ and $A = 0.33 \pm 0.02$. For comparison, $B = -40.9 \pm 0.2$ and $A = 0.34 \pm 0.01$ are the values obtained fitting the experimental initial intensity.

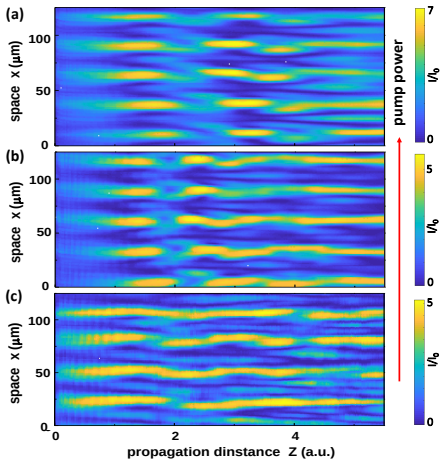

Figure 2.6. From the integrable to the non-integrable regime. Nonlinear evolution detected for $k = 0.021\ \mu\text{m}^{-1}$ and $A = 0.5$ varying the external pump power: (a) $P = 6$ mW, (b)$P = 2$ mW and (c) $P = 0.5$ mW. The recurrent behavior in (a) is superseded by the appearance of spatial solitons (c) as the dynamics is far from integrability (highly-saturated conditions).

2.6 Discussion

The predictability of the FPUT dynamics is a general property of the system and does not depend on the specific input state. However, nonlinear evolution becomes more complex when several harmonics are initially excited. We observe that for two excited input modes recurrent high-intensity patterns still occur but their periodicity is lost and different states are experienced during propagation. Starting with a superposition of a large number of modes, random noise or localized perturbations, wave turbulence sets in [107, 108]. In these complex regimes, disordered nonlinear interactions may play a crucial role with respect to exact solutions of the underlying model [109]. Finally, we note that the observed recurrence gradually disappears as the external pump is weakened, a finding that further corroborates integrability as the basis of the phenomenon. The continuous transition towards the non-integrable regime is reported in Fig. 2.6. Pseudo-recurrent breather structures persist as the nonlinearity approaches the saturable regime and the model departs from the canonical NLSE [110] [Fig. 2.6(a-b)], whereas no return to the initial state occurs in highly-saturated, non-integrable conditions [Fig. 2.6(c)]. Here, interacting spatial solitons form and evolve towards equilibrium compatibly with a soliton turbulence scenario [111].

The optical setting we have introduced, in which the input condition can be in principle arbitrarily shaped, provides a general test-bed for investigating universal nonlinear phenomena. Our findings shed light on the foundations of the FPUT problem and represent a unique test for nonlinear wave theory, with broad implications in hydrodynamics, nonlinear optics, Bose-Einstein condensates and beyond. In the future we plan to extend our analysis

to systems with multi-mode excitation, at least two, to further validate the Grinevich-Santini theory.

Chapter 3

Bessel Beam propagation in self-focusing medium

A Bessel beam (BB) represents an example of a beam that does not suffer diffraction. In this Chapter we present our studies on the effects of a self-focusing nonlinearity. We observed that BBs, at first, undergo to self-trapped oscillations that gradually decay into breathing-like solitons. This resulting wave is analyzed and several peculiar properties are reported, such as their behavior during collisions. Furthermore, we exploit BBs to optically write waveguides in a bulk crystal via the electro-optic effect.

3.1 Nonlinear Nondiffracting Waves: an overview

In Chapter 1, we have first introduced BBs and Airy Beams (AB) as non-diffracting solutions of the linear Schrödinger equation (1.8) and then we have shown how a self-focusing nonlinearity can counterbalance the diffraction for spread waves. Here, our aim is to merge the two phenomena, i.e. we want to investigate how non-diffracting waves respond to nonlinearity.

Without diffraction, self-focusing will generally lead to an unchecked wave distortion: the spatially-resolved intensity pattern causes a spatially-resolved phase-modulation that, on propagation, is transformed into an intensity modulation that is not, in general, balanced by diffraction. The scenario finds confirmation in recent experiments on ABs undergoing strong self-focusing, where off-shooting soliton emission is observed [112, 113]. This intuitive picture, in turn, appears fundamentally different for BBs, where numerical studies reveal an intriguing phenomenon, according to which strong self-focusing generates a signature breathing of the beam that can even partially support self-guiding [114, 115]. Furthermore, energy transfer from the tails to the central lobe along propagation can lead to stationary conical waves in Kerr systems with nonlinear loss [116, 117].

Our work has consisted in predicting and experimentally observing a Bessel-Beam

optical self-trapping, a breather that forms when a BB suffers strong self-focusing and undergoes long propagation distances. The effect emerges through a precise interplay of the residual diffraction associated to the finite-energy physical realization of the BB and the action of distributed lensing on the underlying conical spatial spectrum.

3.2 Numerical Results

In this Section we report the numerical results obtained through the beam propagation method (detailed in Chapter 1). In distinction to previous studies [114, 115, 118–122], we carry out simulations using Kerr-saturated nonlinearities, as this both describes experimentally accessible spatial soliton-supporting mechanisms and avoids catastrophic beam collapse typical of unsaturated Kerr propagation in the inherently 2+1D geometry [123].

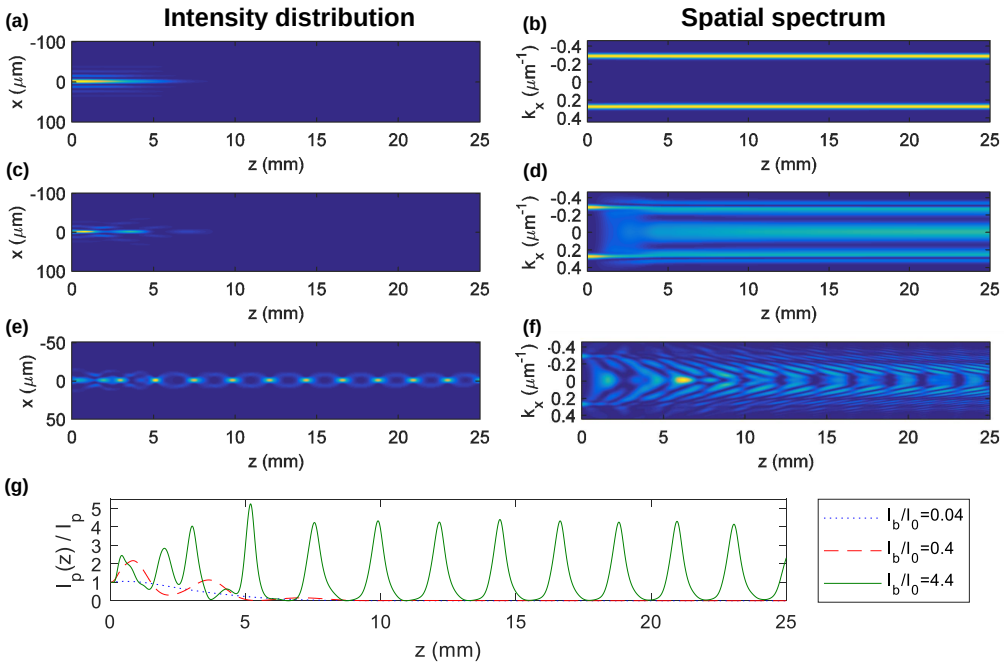

Figure 3.1. Bessel-Beam breather self-trapping. Numerical 2+1D simulated nonlinear propagation of an initial $\lambda = 532$ nm fundamental BB with $k_r = 0.28\ \mu\text{m}^{-1}$ and a gaussian $\sigma = 60\ \mu$m envelope for different input peak intensities I_p/I_s, with $n_0 = 2.3$ and $\Delta n_0 = 5.6 \times 10^{-4}$. (a) x,z section of the intensity distribution (the distribution is symmetric for rotations around the propagation axis) with $I_p/I_s = 0.04$ and (b) corresponding k_x, z section of the transverse spatial spectrum distribution, where the ring structure leads to a propagation-invariant double spot. (c) BB dynamics for $I_p/I_s = 0.4$ and (d) corresponding evolution of the spatial spectrum, with the characteristic generation of low-frequency components and the appearance of a second ring. (e) A breathing self-trapped solution at $I_p/I_s = 4.4$ and (f) corresponding spatial spectrum. The original BB is locked into an oscillating solution that is now localized in the transverse plane and periodic along propagation. (g) Peak-intensity $I_p(z)/I_p$ for the various conditions.

The formation of BB self-trapped state is shown numerically in Fig. 3.1 for an input $\lambda = 532$ nm zero-th order BB of amplitude $J_0(k_r r)\exp[-(r/\sigma)^2]$, with $r = \sqrt{x^2+y^2}$ and where k_r and σ are selected to match experiments (see next Section). Simulations are carried out using the split-step-Fourier-method (or beam-propagation-method [65]) applied to nonlinear spatial wave dynamics [49]. The full 2+1D NLSE is solved, that is, both transverse x and y axes are considered along the propagation axis z while, in the figures, we report only specific sections of the 2+1D intensity distribution. The envelope produces a physically observable finite-energy approximation of the BB (a so-called Bessel-Gauss-Beam) [19]. Specific reported results refer to an exponential nonlinearity $\Delta n = -\Delta n_0 \exp(-I/I_s)$, where Δn_0 and I_s fix its strength and saturation intensity, respectively [47]. This nonlinearity describes the phenomenon of quasi-steady-state self-trapping and solitons in both ferroelectric crystals, such as SBN, and paraelectric crystals, such as KLTN [124–127]. The effect reduces to the Kerr case for negligible saturation, that is, for short exposure times in the quasi-steady-state response and low peak-intensity-to-background-intensity ratios. In Fig. 3.1(a) the intensity distribution in the x, z plane is reported for parameters $\Delta n_0 = 5.6 \times 10^{-4}$ ($n_0 = 2.3$) and an input peak intensity $I_p(z=0) \equiv I_p = 0.04 I_s$. In these conditions the input beam with a 10 μm central lobe evolves linearly with a diffraction length $L_D \simeq 7.5$ mm. The spatial spectrum is the characteristic ring or annular distribution of the linear conical BB and is propagation-invariant, as reported in Fig. 3.1(b). As the peak intensity is increased to $I_p/I_s = 0.4$, propagation is modified (Fig. 3.1(c)) and the spatial spectrum changes, with the appearance of a signature second ring [Fig. 3.1(d)], in agreement with previous studies [114, 119]. In turn, as the nonlinear response increases, for $I_p = 4.4 I_s$, the initial BB becomes a self-trapped breathing solution [Fig. 3.1(e)] with an equally breathing spectrum [Fig. 3.1(f)], i.e., a wave whose energy is localized in the transverse plane xy and oscillates along the propagation z in close analogy with temporal breathers [128, 129]. While the original BB diffracts on consequence of its finite gaussian transverse envelope, in this highly nonlinear regime, the breathing solution is both localized and with a propagation invariant pulsing [Fig. 3.1(g)]. Interestingly, the breathing phenomenology reported appears qualitatively similar to what encountered in Bessel-Beams in systems with nonlinear losses where, however, pulsing occurs on scales connected to the interplay between losses and replenishing from tails [117, 130], i.e., is not governed solely by diffraction, as in our case.

3.3 Experimental Results

Experiments are performed in a compositionally disordered photorefractive KLTN crystal (Potassium-Lithium-Tantalate-Niobate - $K_{0.95}Li_{0.05}Ta_{0.6}Nb_{0.4}O_3$), grown through the top-seeded solution method by extracting a zero-cut optical quality specimen that

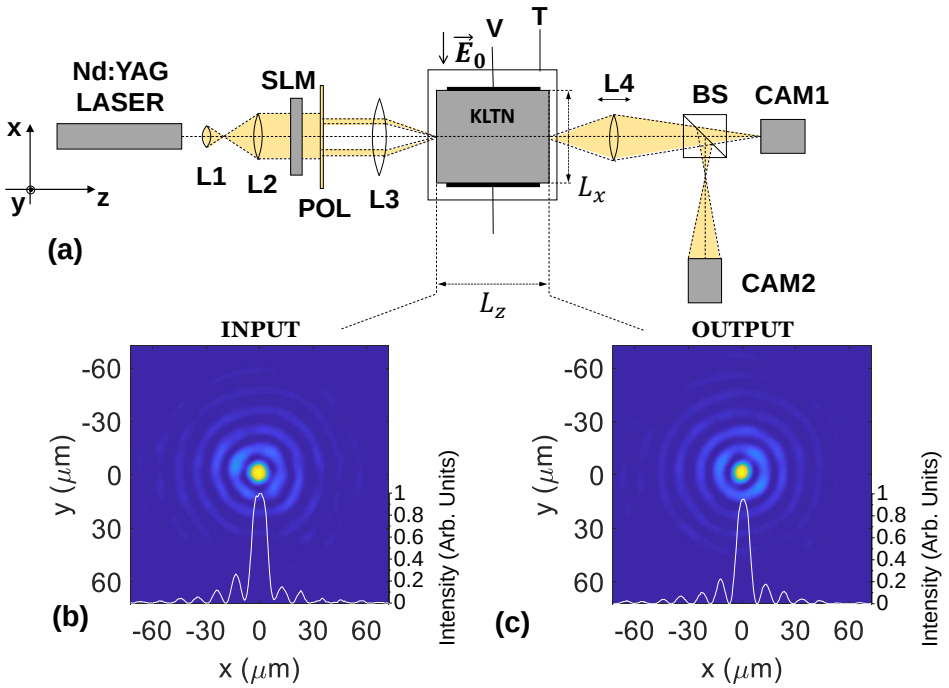

Figure 3.2. (a) Experimental setup. The input BB is generated using a liquid-crystal SLM. The laser beam from a doubled Nd:YAG laser at 532 nm is expanded (lenses L1 and L2) to impinge as a plane wave onto the SLM that, using a polarizer (POL), transmits a ring. The transmitted light is then focused and Fourier-transformed onto the input of a photorefractive KLTN crystal, generating the input BB. Δn_0 is fixed through the x-directed bias electric field $E_0 = V/L_x$ and the Peltier-controlled sample temperature T. CAM1 records the intensity distribution while CAM2 the spatial spectrum. (b-c) Transverse intensity distribution at input (b) and output (c) facets of the crystal with negligible diffraction for the $L_z = 1.8$ mm propagation.

measures $L_x = 2.6$ mm, $L_y = 3.4$ mm , $L_z = 1.8$ mm along the x-y-z axes. The setup of the experiment is sketched in Fig. 3.2(a). The sample is kept at $T = T_C + 9$ K above its ferroelectric Curie point at $T_C = 292$ K using a Peltier cell. The sample manifests a quadratic electro-optic effect and the index of refraction is $n = n_0 + \Delta n$ with $\Delta n(E) = -(1/2)n_0^3 g_{eff}\epsilon_0^2(\epsilon_r(0)-1)^2E^2$, where $g_{eff} = 0.14\text{m}^4\text{C}^{-2}$ is the effective quadratic electro-optic coefficient, ϵ_0 is the vacuum permittivity, $\epsilon_r(0) \simeq 1.0 \times 10^4$ is the quasi-static relative permittivity of the medium, and E is the low-frequency electric field. BBs can be engineered in various ways, using intensity masks [17], axicon lenses [131, 132] or holograms [24]. In our experiment, the launch BB is obtained from a continuous-wave $\lambda = 532$ nm doubled Nd:YAG laser that is enlarged and made to propagate through a Spatial-Light-Modulator (SLM) that transmits a ring [133]. The modulated 600 nW x-polarized beam is now focused onto the input facet of the sample, made to propagate along the z axis, and its intensity distribution in the transverse x,y plane is imaged onto a CCD camera. A zeroth-order Bessel-Gauss beam with $k_r = 0.28\ \mu\text{m}^{-1}$ and $\sigma = 60\ \mu$m [Fig. 3.2(b)] is launched into the $L_z = 1.8$ mm long sample and suffers negligible distortion for linear propagation [Fig. 3.2(c)]. Note that our choice of σ allows us to inspect at least one breathing oscillation for the finite length of the sample. Numerical simulations indicate that larger envelopes, characterized by more extended ring-like tails, lead to analogous phenomenology but require stronger nonlinearity. The case with $\sigma = 120\ \mu$m is reported in Fig. 3.3.

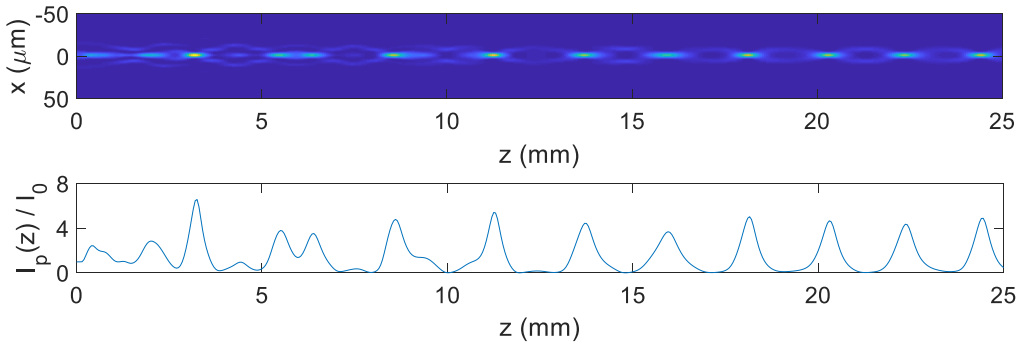

Figure 3.3. Nonlinear propagation with $\sigma = 120\ \mu m$ in an exponential nonlinearity ($\Delta n_0 = 5.65 \times 10^{-4}$, $I/I_s = 4.4$).

Experiments aimed at investigating nonlinear dynamics of initially non-diffracting waves pose the basic challenge of requiring long propagation distances. To inspect the formation of the breather self-trapped state keeping the propagation distance L_z constant, we make use of the quasi-steady-state response, typical of photorefraction [47, 134], i.e.,

$$\Delta n(I,t) = -\Delta n_0 e^{-I/I_s(t)}. \tag{3.1}$$

Here t is the interval of time from the beginning of optical exposure, $\Delta n_0 = \Delta n(E_0)$, $I_s(t) = I_d t_d/2t$, I_d and t_d are constants, the dark-illumination (that can be changed using a background illumination) and dielectric relaxation time, respectively, while the factor 2 stems from the use of a quadratic electro-optic response [47]. Hence, as t increases, for a fixed I_p and L_z, we are able to observe beam propagation for progressively stronger nonlinearity associated to higher values of normalized intensity I_p/I_s.

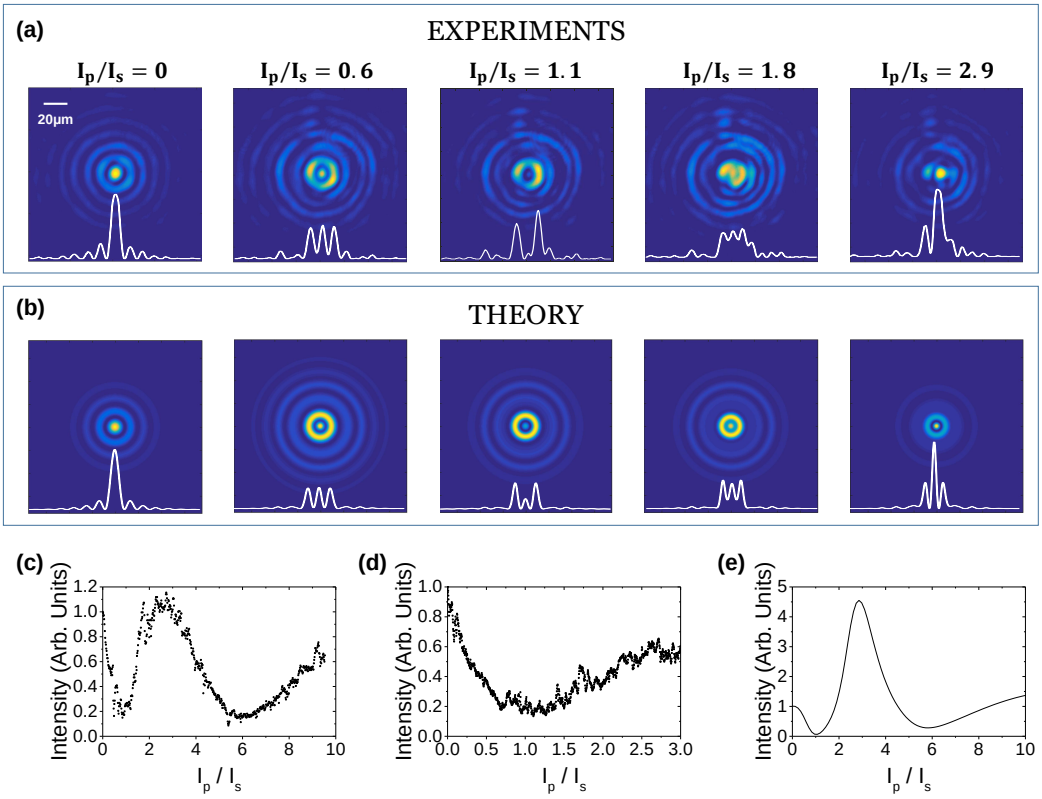

Figure 3.4. Observation of a Bessel-Beam breather. Transverse profile for (a) Experiments and (b) numerical simulations. Experimental central lobe complete oscillation and partial one for (c) I_{d1} and (d) I_{d2}, where $I_{d2} \simeq 10 I_{d1}$ is achieved using an illuminator. A complete oscillation is also reported for numerical simulation (e). The intensity reported in plot (c-d-e) is spatially averaged on a 6 μm radius circular region around the geometric central lobe. The agreement between observations and numerical simulations not only validates the quasi-steady-state model , for which $I_s \propto t$, but also the general physical picture of a breathing self-trapped state. In turn, differences in the fine details in the x-directed profiles are due to the fact that anisotropy is not considered in the model (see text).

The observation of a BB breathing in conditions of strong self-focusing ($I_p/I_s > 0.4$) is reported in Fig. 3.4. The sample is first cleaned of spurious photorefractive space-charge using a white light microscope illuminator that causes a homogeneous conductivity. The illuminator is now switched off, and a constant $V = 450$ V is applied to the x-facets of the sample. In these conditions $E_0 = V/L_x = 1.7$ kV/cm and $\Delta n_0 \simeq 5.24 \times 10^{-4}$.

Starting from the linear propagation at $t = 0$, the response accumulates, I_p/I_s grows and the breathing feature becomes manifest. The breathing behavior is reported in Fig. 3.4(a) in the transverse plane and is compared with the predicted beam intensity distribution, reported in Fig. 3.4(b). The slight anisotropy observed in the beam and the lateral asymmetric distortion are the effects of underlying response anisotropy. In turn, no beam bending is observed, suggesting a negligible role of nonlocal effects that are absent in the Kerr-like model of Eq.(3.1) [5]. Breathing is observed for different values of input parameters for sufficiently strong nonlinearity. According to Eq. (3.1), I_s determines the strength of the nonlinearity. In Fig. 3.4(c,d) we report the behavior for different values of nonlinearity, experimentally controlling $I_s(t = 0)$ via the dark-illumination I_d and keeping I_p fixed. For the higher nonlinearity $I_p/I_s \simeq 100$ of Fig. 3.4(c), we are able to explore a full period of the breathing. For the weaker (but, in any case, strong) nonlinearity of Fig. 3.4(c), with $I_p/I_s \simeq 9$, a partial breathing oscillation is also visible, while Fig. 3.4(e) reports the numerical prediction.

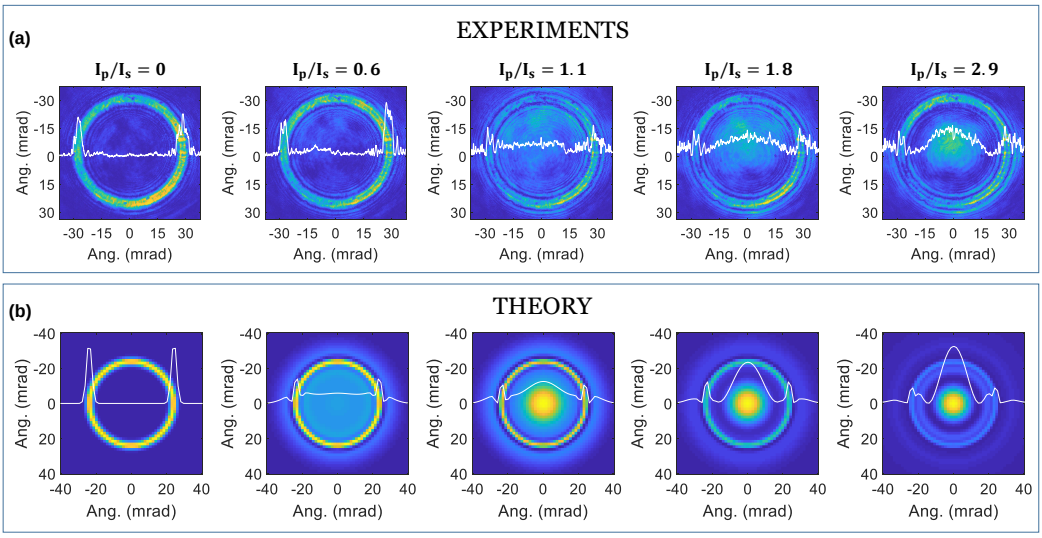

Figure 3.5. Bessel-Beam breathing spectrum. The intensity of the ring is progressively reduced and a central lobe appears (a) in agreement with numerical simulations (b) (see text).

To understand the physical underpinnings of Bessel-Beam self-trapping we consider the dynamics of the spatial spectrum, reported in Fig. 3.5. In the first panel of Fig. 3.5(a) the input spectrum shows a ring structure, typical of a BB, but with a finite width, the spectral footprint of the gaussian envelope. As self-focusing sets in, the ring spectrum is progressively transformed into a more elaborate structure with multiple concentric rings and a central lobe, similar to a BB, but now in the spatial spectrum. This reflects the fact that, while self-focusing can compensate the diffraction associated to the finite width of the ring, no balancing can exist for the ring itself, that is inherently non-diffractive. Consequently, while the gaussian enveloped is trapped into what would be a spatial soliton, the discrete

annular portion of the spectrum suffers a distributed lensing effect and is Fourier-transformed at each equivalent diffraction length of the gaussian envelope, i.e., passes from a ring to a BB-like distribution [see second and third panels of Fig. 3.5(a)]. The picture is further validated by numerical predictions reported in Fig. 3.5(b).

3.4 Bessel self-trapping interaction

We saw in Chapter 1 that solitons have a peculiar behavior during interactions. In this Section we want to further characterize BBs self-trapping by studying nonlinear BBs collision. We show that they behave differently from standard solitons.

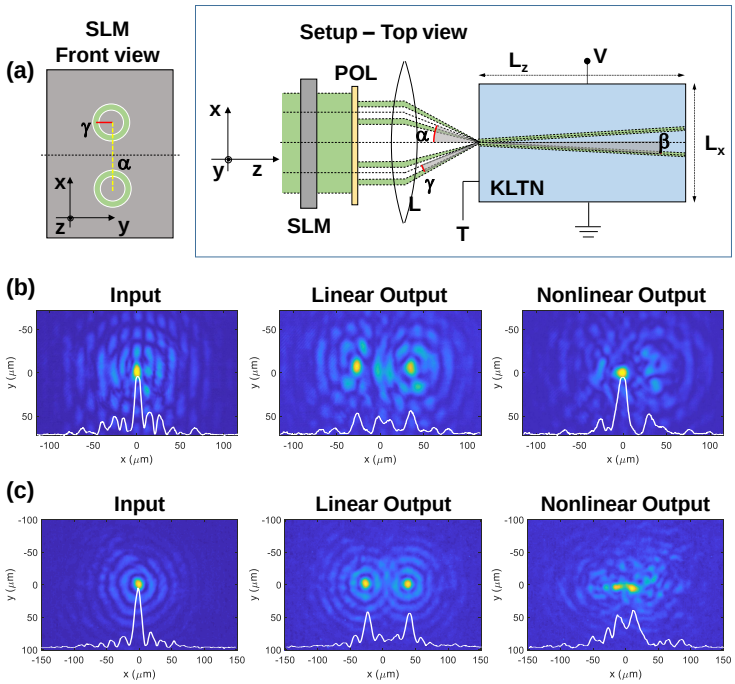

Figure 3.6. Nonlinear BBs interaction. (a) Sketch of the experimental setup for half-collisions, we use this configuration to have a good beams separation after the 1.8 mm sample propagation. By governing the size and position of the rings on the SLM we are able to control the Bessel vector k_r (associated with the angle γ) and the external collision angle α that correspond to the internal angle $\beta = \alpha/n_0$ with n_0 the linear refractive index of the sample. For further details of the setup refer to the caption of Fig. 3.2. (b)-(c) Collision between (b) coherent in-phase and (c) incoherent BBs ($k_r = 0.28$ μm^{-1} and gaussian envelope of FWHM=110 μm). (b) A $E_0 = 1.7$ kV/cm electric field makes the interaction nonlinear and generates an off-shooting bright beam with FWHM=15 μm that does not correspond to the centres of the parents BBs. (c) The $E_0 = 1.7$ causes the attraction between the centres of the original BBs without fusion.

For experiments we use almost the same setup of Fig. 3.1, in which we sent two Bessel, instead one, so that they can collide on the input facet of the crystal as detailed in Fig. 3.6(a).

Moreover, thanks to the SLM homemade interface, we can send the two BBs at the same time or alternating to have a coherent or incoherent collisions.

For mutually coherent in-phase BBs, we observe the emerging of an off-shooting soliton as in Fig. 3.6(b). Even if soliton fusion is a well-known phenomenon in saturable media, the behavior of BBs is a bit surprising respect to what occurs for gaussian beams in the same conditions. Indeed, we send two gaussian beam with FWHM$\simeq$ 10 μm, the same value of the central core of the BBs in Fig. 3.6(b) and with the same collision angle α and we observe only attraction and no fusion (not reported).

The BB interaction is governed by the mutual coherence and the angle α. To understand the importance of the first we make the two BBs mutually incoherent. We observe that they evolve independently with negligible attraction [Fig. 3.6(c)]. In fact, a single BB of the pair evolves irrespectively of the other and we can obtain the same BB self-trapping reported above (not showed).

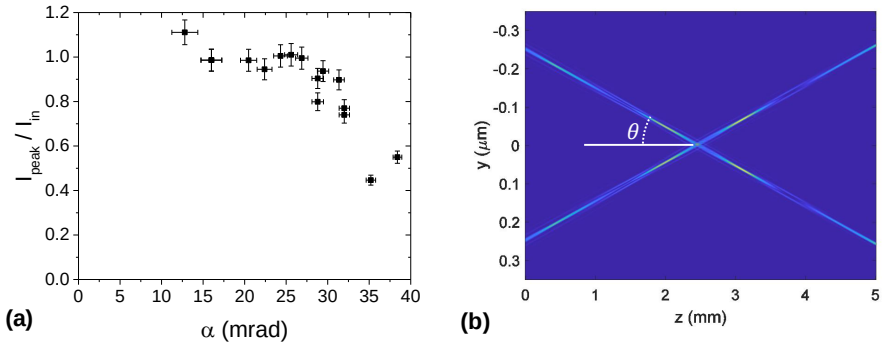

Figure 3.7. Study of the angle $alpha$ collision dependence. (a) Plot of the experimental normalized intensity of the off-shooting soliton versus the $alpha$. (b) Numerical simulation for $\alpha = 100$ mrad.

The collision angle dependence is studied repeating the experiment for various angles and taking the intensities of the off-shooting beams. The data are reported in Fig. 3.7(a). They show that the intensity decreases as angle α increase. The asymptotic behavior is studied through numerical simulations since we are limited by our setup to $\alpha < 40$ mrad. In Fig. 3.7(b), we show the propagation for $\alpha = 100$ mrad : the off-shooting beam is absent.

These results deserve a deep investigation. It seems that BBs have a stronger interaction than solitons due to their bigger extension in space. We believe that, for coherent BBs, the system has a sort of resonance so that the off-shooting beam exists for $\alpha \sim 28$ mrad, that is the value of the BB Fourier spectrum as in Fig. 3.5.

3.5 Discussion

We note that the breathing self-trapped state here investigated is stable on accessible distances, while numerical simulations indicate that weak radiation ultimately causes it to decay into a conventional breathing soliton state [135–137]. In Fig. 3.8(a), for example, this

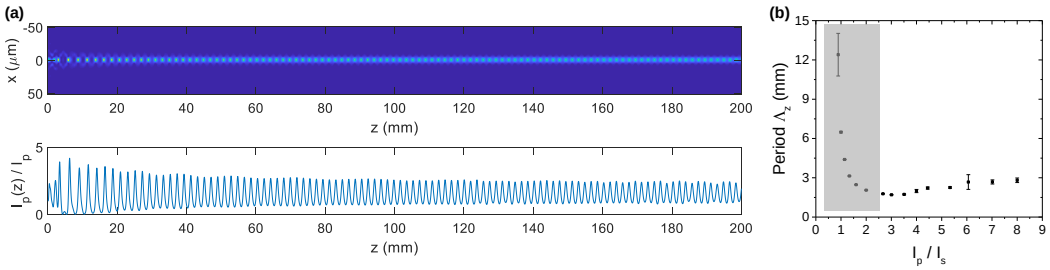

Figure 3.8. (a) Long propagation ($L_z = 300$ mm) of a Bessel-Gauss beam with $k_r = 0.28\ \mu m^{-1}$ and $\sigma = 60\ \mu m$. The numerical simulations are performed with the exponential nonlinearity with $I/I_s = 4.4$ and $\Delta n_0 = 4.87 \times 10^{-4}$. (b) Breathing period Λ_z versus I_p/I_s. The gray area indicates values of I_p/I_s that give rise breathing soliton without Bessel self-trapping. The values of Λ_z are obtained averaging on more than three periods, disregarding the first four oscillations.

transition occurs in our experimental conditions for $L_z = 30$ mm. We note that for a given set of launch parameters (k_r, σ), breathers and self-trapping are found to occur for a specific range of values of Δn_0 and I_p/I_s. Within this range, the actual values of Δn_0 and I_p/I_s fix the breathing period Λ_z. Congruently with what expected from a pure Kerr-like model, where no self-trapped BB state is possible, for lower saturation ratios the soliton breathing regime appears before the BB self-trapped regime emerges. For example, in Fig. 3.8(b), we report the predicted Λ_z with the two different behaviours, for several values of I_p/I_s and $\Delta n_0 = 5.6 \times 10^{-4}$. The breather soliton that appears for lower I_p/I_s has a Λ_z that decreases increasing I_p/I_s while, for the self-trapped state, Λ_z increases as I_p/I_s increases. Values of launch I_p/I_s outside this range cause the BB to spread (low I_p/I_s) or collapse (high I_p/I_s).

The phenomenology reported is general because it emerges also for other saturated nonlinearities, such as for $\Delta n(I) = -\Delta n_0(1 + I/I_s)^{-1}$ and $\Delta n(I) = -\Delta n_0(1 + I/I_s)^{-2}$. Evidence of the nonlinear propagation supported by the latter law is given in Fig. 3.9. These are local approximate models for experiments in biased ferroelectric and paraelectric photorefractive crystals, respectively [138, 139]. Indeed, comparing Fig. 3.8(a) and Fig. 3.9, they both qualitatively describe the same phenomenon, that is, the initial self-trapping state and the following breather soliton. The unsaturated Kerr case $\Delta n = n_2 I$, instead, does not lead to stable self-trapping, as expected.

Concluding, solitons and non-diffracting waves share similar phenomenology but have a profoundly different nature. Solitons stem from the balance between diffraction and

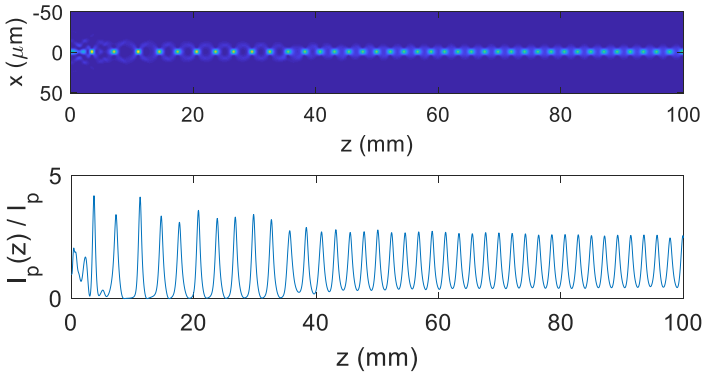

Figure 3.9. An $L_z = 100$ mm propagation of Bessel-Gauss with $k_r = 0.28\ \mu m^{-}1$ and $\sigma = 60$ μm evolving according to the saturable Kerr nonlinearity law. The other parameters of this simulation ($I/I_s = 4.4$, $\Delta n_0 = 4.87 \times 10^{-4}$) are the same as in Fig. 3.8(b).

self-focusing, while non-diffracting waves are volume interference patterns. We have demonstrated numerically and experimentally that a Bessel-Beam propagating in a strongly self-focusing medium undergoes relevant propagation dynamics that ultimately cause it to self-trap into a periodic breather. The oscillating spatial spectrum appears as a sequence of periodic Fourier transformations of the original beam from an annular to a Bessel-like distribution. Findings indicate a new form of nonlinear construct in which an interference pattern locks together with a diffracting wave, shedding light into the physics of non-diffracting waves and their behavior in materials.

3.6 Bessel beams waveguide induction

Since now, we have addressed Bessel beam nonlinear evolution in a self-focusing medium. For some applications, such as optical writing, it is preferable to handle with linear phenomena because this guarantees the scalability of the process, a key ingredient to build miniaturized photonic 3D circuits that are fundamentally to develop innovative optical devices. Indeed, while present achievements are based on planar photonic circuits [140–142], in principle operating in a fully three-dimensional volume increases the achievable number of interlinked gates and devices and this requires specific fabrication tools, such as direct optical writing or 3D printing [143–148]. At present, direct writing involves a step-by-step fabrication that becomes increasingly cumbersome as circuit complexity grows. Furthermore, as the details of the circuitry are scaled down to the optical wavelength, the requirement that the writing beam focus be ever smaller increases the impact of diffraction and introduces limitations on the effective available volume. Previous studies have attempted to overcome diffractive distortion in optical writing and achieve scalability using nonlinear effects, by which the beam carrying out the writing is self-guided by the waveguide it is

creating, a phenomenon related to spatial solitons known as self-writing [127, 149–152]. In turn, the nonlinearity introduced by the self-writing fundamentally limits the circuit capability, so that writing two waveguides in close proximity follows the physics typical of soliton-soliton interaction [153–155]. The result is a method that does not have writing linearity, a potentially crucial feature by which the writing of a given component does not affect and is unaffected by other previously written components. At present no optical writing technique based solely on linear waves has been demonstrated in a full macroscopic volume that is scalable, i.e., unaffected by diffraction.

In what follows, we want to demonstrate the use of Bessel beams to optically write patterns unaffected by diffractive distortions able to guide and route light, in the form of localized modes, through a volume. In our experiments, the method also maintains writing linearity allowing us to fabricate waveguides in increasingly complex geometries, integrated multi-port splitters and miniaturized functional electro-optic gates.

3.6.1 Theoretical Background

We optically induce the BB pattern in a photorefractive crystal. Writing is carried out using a Bessel-Gauss beam with $A_w = A_{w0} J_0(k_r r) \exp[-(r/\sigma)^2]$, with k_r and σ chosen so that Rayleigh length $z_R = \pi n \sigma^2/\lambda \gg L_z$, where L_z is the length of the sample along the propagation axis [19]. The photoexcitation of deep in-band impurities and charge transport lead to the formation of an optically-induced space-charge field $E_{sc}(I_w, t)$ given by [5]

$$E_{sc}(I_w, t) = E_{0w} \left(e^{-\left(1+\frac{I_w}{I_d}\right)\frac{t}{t_d}} - 1 \right). \tag{3.2}$$

Here $I_w = |A_w|^2$ is the writing intensity distribution, t is the duration of writing process, I_d and t_d are constants, the dark-illumination (that can be changed by also illuminating the sample with a plane wave) and the dielectric relaxation time, respectively [5]. $E_0 = E_{0w}$ is, in turn, the constant external bias field applied to the sample along one transverse axis, say the x axis, during the writing phase. The electric field $E = E_{0w} + E_{sc}$ now changes locally the sample index of refraction through the electro-optic effect. Since the sample is heated above its room-temperature Curie point T_C, in the paraelectric phase, it manifests a quadratic electro-optic effect according to which $\Delta n = -(1/2) n_0^3 g_{eff} \epsilon_0^2 (\epsilon_r(T) - 1)^2 E^2 \equiv -\Delta n_{0,T} (E/E_0)^2$. Here, g_{eff} is the effective electro-optic coefficient, ϵ_0 is the vacuum dielectric constant, $\epsilon_r(T)$ is the low-frequency sample relative dielectric constant at the writing temperature T, and $\Delta n_{0,T} \equiv (1/2) n_0^3 g_{eff} \epsilon_0^2 (\epsilon_r(T) - 1)^2 E_0^2$ is the characteristic scale of the response for the given temperature and bias field E_0. The presence of the dielectric anomaly at $T = T_C$ implies that the dielectric constant in the paraelectric phase is strongly temperature dependent, following the Curie-Weiss law $\epsilon_r(T) = C/(T - T_C)$ [44]. Hence, heating the sample to a sufficiently high temperature $T_w > T_C$ causes the

electro-optic response to drop and renders nonlinear beam effects and self-writing negligible [2, 116, 117].

The light-induced E_{sc} of Eq. (3.2) can now be used as a blue-print for the electro-optic activation of a waveguide. This is achieved by cooling the sample closer to the Curie point to T_g ($T_g < T_w$), leading to a strongly enhanced $\epsilon_r(T_g) > \epsilon_r(T_w)$, and applying an appropriate bias guiding electric field $E_0 = E_{0g}$. The resulting index pattern is

$$\Delta n(E_{0g}) = -(1/2)n_0^3 g_{eff}\epsilon_0^2(\epsilon_r(T_g) - 1)^2(E_{0g} + E_{sc})^2. \tag{3.3}$$

This index pattern can be used to guide and route an optical field A_g (Eq.(1)) with no further light-induced changes in E_{sc}. This can be achieved either using attenuated light ($I_g \equiv |A_g|^2 \ll I_w$), effectively halting the build-up process, or using longer wavelength light, for which the photoexcitation process becomes inefficient. For $E_{0g} = E_{0w}$ and for unsaturated conditions (i.e., $t \ll t_d$), Eqs. (3.2) and (3.3) give $\Delta n \propto I_w$, reproducing the process analyzed in Fig. 1 (with $A_g(r, z = 0) = A_0 \exp[-(r/\sigma_G)^2]$). More generally, $E_{0g} \neq E_{0w}$ leads to a varied family of different guiding, routing, and antiguiding structures described by Eq. (3.3) and the NLSE [Eq. (1.7)]. This allows fast electro-optic control of the index of refraction pattern with no nonlinear propagation and without involving the slow charge migration processes required to alter the space-charge density [156–158].

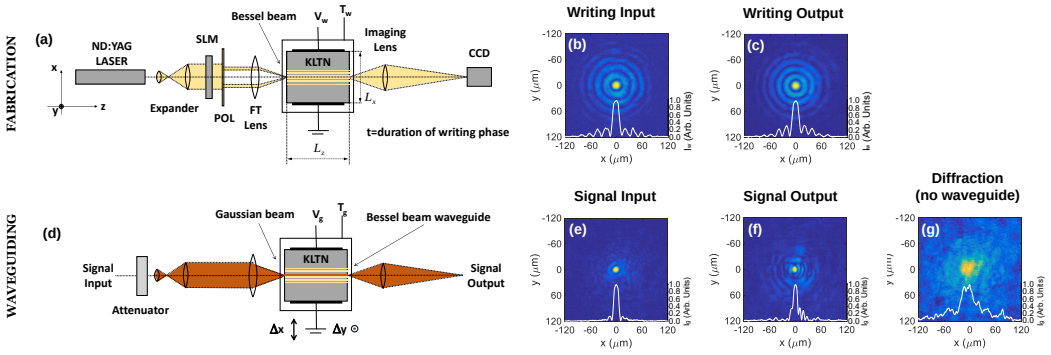

Figure 3.10. Demonstration of a BB waveguide in photorefractive KLTN. Fabrication : (a) scheme of the optical writing stage; (b) input and (c) output intensity distribution of the writing beam ($k_r = 0.16\ \mu\text{m}^{-1}$ and $\sigma = 110\ \mu$m). Waveguiding: (d) scheme of the optical guiding stage; (e) input and (f) output of a Gaussian guided beam (input FWHM $= 12\ \mu$m, $\sigma_G = 10\ \mu$m) compared to (g) the diffracted output distribution with no waveguide (output FWHM $= 39\ \mu$m).

3.6.2 Experiments

The setup for writing is the same used for studying the BB self-trapping, as can be easily understood comparing Fig. 3.2(a) with Fig. 3.10. The main difference, as explained above, it that now we operate at high T, namely $T_w \sim T_C + 20$ K to avoid the electro-optic effect.

Indeed, we do not appreciate any evolution of the BB profile between the input facet, Fig. 3.10(b), and the output facet of the crystal, Fig. 3.10(c), even after 6 minutes of exposing the sample to 2.5 kV/cm writing field E_w. This setup for the reading is modified sobstituting the SLM-polarizer pair with an attenuator as shown in Fig. 3.10(d), so that we pass from $I_w = 1.5$ μW BB power intensity in writing to $I_r = 40$ nW gaussian beam in reading. In this conditions, the waveguide is activated without further modification induced by light and we can see that the x-polarized gaussian beam of FWHM$= 12$ μm is guided inside the 1.8 mm length of the crystal [Figs. 3.10(e),(f)]. For comparison, in Fig. 3.10(g) we report the same output intensity distribution if no fabrication stage is enacted and the BB waveguide is absent, where the beam spreads to an output FWHM of 39 μm.

To demonstrate the capability of our waveguide induction method, we show in Fig. 3.11, some of the most significant results that we got. In Fig. 3.11(a)-(e) we report the use of writing linearity, that is, the ability to write structures independently in the same sample in close proximity. In our specific demonstration, we fabricated two parallel waveguides at different distances. For a distance of 15 μm, the waveguide pair acts as a mutual phase-dependent direction-coupler [Fig. 3.11(a)-(c)]. For a larger interwaveguide distance 20 μm, each waveguide acts independently and no mode coupling is detected for the length of the sample L_z [Fig. 3.11(d),(e)].

In Fig. 3.11(f)-(n) we demonstrate the use of BB waveguide writing to achieve 1×2, 1×3, and 1×4 splitters launching multiple angled BB during the fabrication stage. The BBs are rendered mutually incoherent using a specific SLM time sequenced mask that turns on only one BB at a given time. This demonstrates how fabrication of complex circuitry can also be achieved in a single illumination stage without having to mechanically shift and move the sample, as instead is required in direct writing scanning techniques.

With these last experiments, we have demonstrated the use of single and multiple Bessel beams to optically write waveguides and electro-optic circuits in a bulk crystal. Our method represents the first scalable method able to realize reprogrammable optical networks in a full 3D setting.

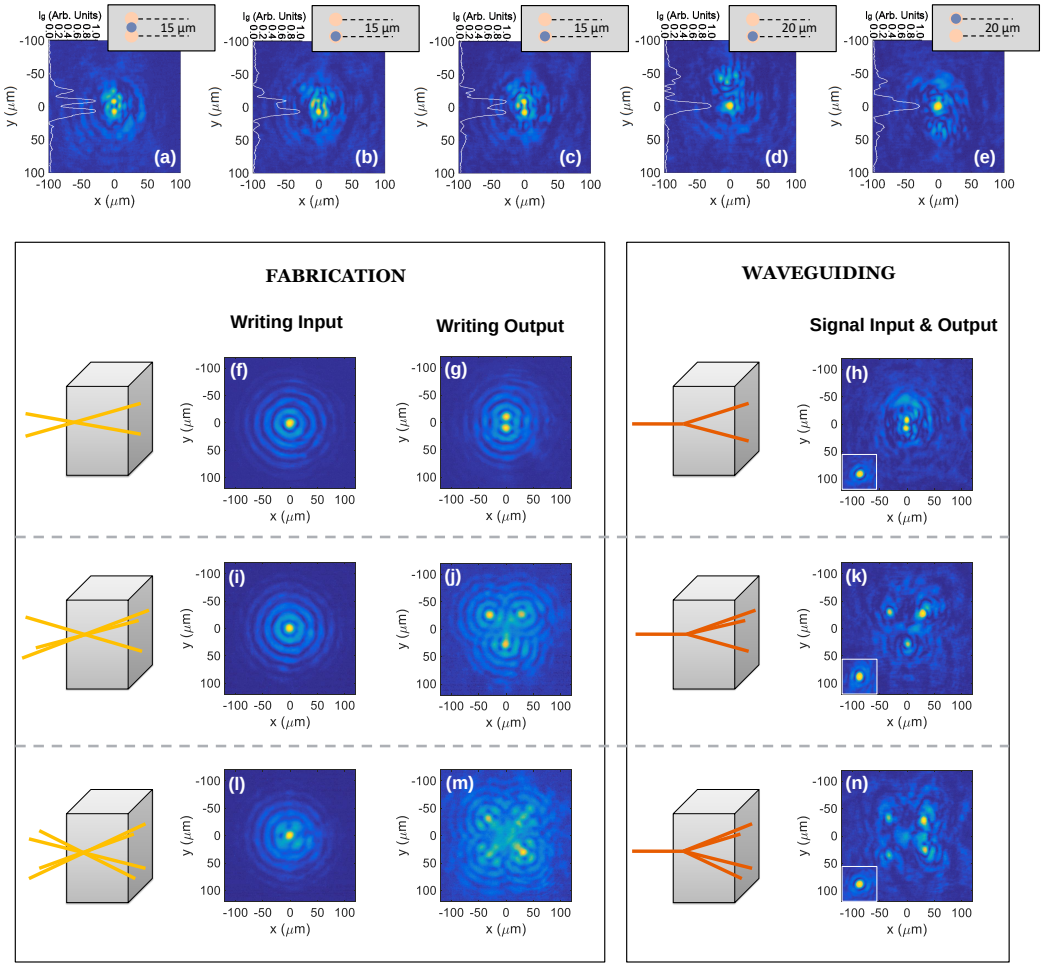

Figure 3.11. Examples of multi-waveguide structures achieved using BB writing. BB waveguide directional coupler (a)-(e). (a) Output intensity distribution when the signal input is launched inbetween two parallel BB waveguides ($\Delta y = 0$), 15 μm apart. (b),(c) Directional coupling from one waveguide to the other when the signal input is launched into one of the waveguides ($\Delta y = -7.5$ μm). Coupling is found to be strongly dependent on the effective optical length of the coupler, leading to different coupling efficiencies for slightly different values of T and V_g ((b) and (c) differ by $\Delta T \simeq 0.5$ K). For $L_z = 1.8$ mm, coupling becomes negligible for waveguides 20 μm apart, as reported in (d) and (e), with $\Delta y = -10$ μm and $\Delta y = 10$ μm respectively. In the insets, yellow points represent the BB waveguides while red points indicate the input position of the Gaussian beam. Multi-splitters writing and testing (f)-(n). (Left) Fabrication of a 1×2 (top), 1×3 (center), and 1×4 (bottom) splitter. 1×2: (f) Input and (g) output intensity distributions of an incoherent superposition of two BBs with a mutual angle of 8.9 mrad. Fabrication writing input and output intensity distributions for a 1×3 (i),(j) and 1×4 (l),(m), where three and four incoherent BBs are launched at the input forming splitters with angles of 33.6 mrad and 35 mrad inside of the crystal, respectively. (Right) Output intensity distribution indicating the splitting of an input launch Gaussian beam at the center of the multi-beam pattern (see inset) for the 1×2 (h), 1×3 (k), and 1×4 (n) structures.

Chapter 4

Continuous Soliton in a Lattice Nonlinearity

Until now, we have studied the nonlinear propagation of different light patterns in a bulk self-focusing medium. In this Chapter we deal with gaussian beams, either one or two dimensional, that propagate in patterned self-focusing nonlinearity, a periodic pattern that both affects and is strongly affected by the wave. Observations are carried out using spatial photorefractive solitons in a volume microstructured crystal with a built-in oscillating low-frequency dielectric constant. The pattern causes an oscillating electro-optic response that induces a periodic optical nonlinearity. On-axis results in potassium-lithium-tantalate-niobate (KLTN) indicate the appearance of effective continuous saturated-Kerr solitons, where all spatial traces of the lattice vanish, independently of the ratio between beam width and lattice constant. Decoupling the lattice nonlinearity allows the detection of discrete delocalized and localized light distributions, demonstrating that the continuous solitons form out of the combined compensation of diffraction and of the underlying periodic volume pattern.

4.1 Physical Context

The coupling between different and matched spectral components of the optical field is one of the fundamental effects governing propagation through periodic systems [159]. The interplay between this coherent effect and nonlinearity has been extensively investigated allowing diffraction control [160, 161] and giving rise to self-localized states, such as discrete and gap solitons [6, 162–166]. Experiments on discrete trapping are generally based on photonic lattices made from etched waveguide arrays [6, 165] or created through optical induction in photorefractive media [164, 167]. Studies have spanned a wide variety of physical mechanisms affecting solitons, such as nonconventionally biasing [168, 169], PT-symmetry [170], and disorder [171]. At present, however, the soliton has always evolved

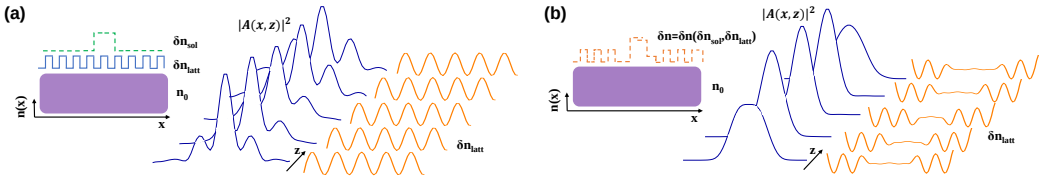

Figure 4.1. Nonlinear propagation in periodic systems. (a) Trapping in photonic lattices: the periodic pattern δn_{latt} affects the spatial propagation but is not affected by the wave. (b) Trapping in lattice nonlinearity: optical field and lattice are mutually coupled and δn_{latt} depends on the waveform.

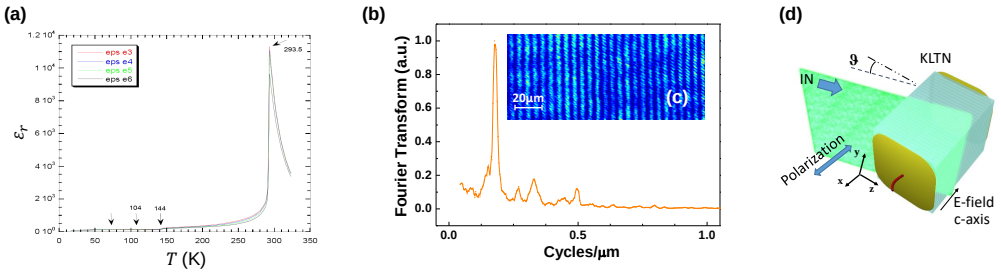

Figure 4.2. Details of the experimental conditions. (a) Dielectric spectroscopy of the KLTN for low-frequencies electric filed. The clear peak indicates the phase-transition at $T = 293.5$ K. (b) Fourier analysis of (c) the trasmittance image of the KLTN that reveal a well-defined peiod of $\Lambda = 5.5 \pm 0.3$ μm. (d) Scketch of the experimental setup.

in a fixed linear/nonlinear pattern, i.e., in conditions in which the lattice is not appreciably affected by the wave [161, 172].

We here study an entirely opposite condition: spatial solitons that form in a lattice nonlinearity. A lattice nonlinearity is a periodic variation in the nonlinear response that is in turn negligible in the linear response. This means the lattice itself depends on the soliton, and both lattice and soliton are strongly interacting during propagation. This fundamental difference with respect to previous experiments is schematically illustrated in Fig. 4.1, where the optical propagation in a photonic lattice is compared with that in a lattice nonlinearity. In general, the standard physical condition [Fig. 4.1(a)] consists in a media with a periodic index of refraction variation δn_{latt}, affecting parametrically the superimposed soliton nonlinearity δn_{sol}. So, while the nonlinear waves evolve into a lattice-dependent trapped state, δn_{latt} remains almost completely unaffected by the waves dynamics. On the contrary, if the beam and lattice are mutually nonlinear, $\delta n = \delta n(\delta n_{sol}, \delta n_{latt})$, the nonlinear propagation modifies spatially the underlying periodic pattern itself (Fig. 4.1(b)).

4.2 Experimental Environment

The experiments are performed in a compositionally disordered photorefractive KLTN crystal, $K_{1-\alpha}Li_{\alpha}Ta_{1-\beta}Nb_{\beta}O_3$ with $\alpha = 0.04$ and $\beta = 0.38$, grown through the top-seeded solution method by extracting a zero-cut $2.4^{(x)}$x$2.0^{(y)}$x$1.7^{(z)}mm$ optical quality specimen. The Curie point at the temperature $T_C = 294$ K is measured and characterized through low-frequency dielectric spectroscopy, reported in Fig. 4.2(a), that also signals the absence of large deviations from the mean-field behaviour, typical of other near-transition disordered ferroelectric samples [62, 173]. The sample is grown so as manifest a sinusoidal variation in the low-frequency dielectric constant [174–176]. An electric field can turn this volume microstructure into a periodic index of refraction modulation $\Delta n(x)$ through the quadratic electro-optic effect [177]. The lattice nonlinearity arises when this electric field is optically-induced, as occurs for the photorefractive screening nonlinearity [5, 178]. The leading terms are

$$\Delta n(x) = \delta n_0 \cos(Kx) - \frac{1}{2} n_0^3 g_{eff} \varepsilon_0^2 \varepsilon_r^2 \left[1 + \frac{2\delta T_c}{T - T_C} \cos(Kx)\right] \left(\frac{E_0}{1 + u(x)^2}\right)^2 , \quad (4.1)$$

where δn_0 contains the contribution of the Sellmeier's refractive index grating, n_0 is the unperturbed average index of refraction, g_{eff} the appropriate electro-optic coefficient, δT_c the amplitude of the nonlinear grating, $K = 2\pi/\Lambda$ the grating number, being Λ the grating period, $E_0 = V/l_x$ ($l_x = 2.4$ mm) the bias field amplitude and $u(x) = \sqrt{I(x)/I_B}$ the beam intensity normalized to that of background.

In Fig. 4.2(c) we report the image of the linear part of the grating, the transmitted light is optically detected with a plane wave for the resonant Bragg condition $\vartheta = \vartheta_B$. We compute the Fourier transform of Fig. 4.2(c) and the result, showed in Fig. 4.2(c), reveals a well-defined grating period $\Lambda = 5.5 \pm 0.3$ μm. We note that Eq. (4.1) states that the spatial period of the nonlinear part is the same of the linear part but the latter only weakly affects propagation. It is central to our present study that, in turn, the field-dependent lattice term is not at all a perturbation to the screening nonlinearity. Indeed, in our sample we obtain from the measured Bragg diffraction efficiency [175] $\delta n_0 \approx 5 \times 10^{-5}$ and $\delta T_C \approx 1$ K, working at $T = T_C + 4$K as in our experiments. Other parameters are $n_0 = 2.4$ (experimentally measured), $\varepsilon_r = 0.91 \times 10^4$ [see Fig. 4.2(a)] and $g_{eff} \sim 0.16$ m^2/C^4, considering the value of Ref. [175].

The experimental geometry in which focused beams are launched into the microstructured KLTN is shown in Fig. 4.2(d); μW cylindrical waves at $\lambda = 532$ nm propagate in a transmission configuration with respect to the grating, with the main wavevector $\mathbf{k} = \mathbf{k}_z$ orthogonal to the grating vector $\mathbf{K}$ and to the bias field (on-axis, $\vartheta = 0$). Light beam polarization is chosen to maximize the external field effect.

4.3 Numerical Simulations

Before exposing the experimental results, it is convenient to discuss some numerical analysis. We perform the simulations evolving a gaussian beam through the NLSE exploiting the saturable Kerr nonlinearity of Eq. (4.1). Details of the integration method, that is the BPM, can be found in Chapter 1. Our model cannot take into account the cumulative nature of photorefractive response but, despite this, we can get several informations about the steady state, especially the index of refraction pattern.

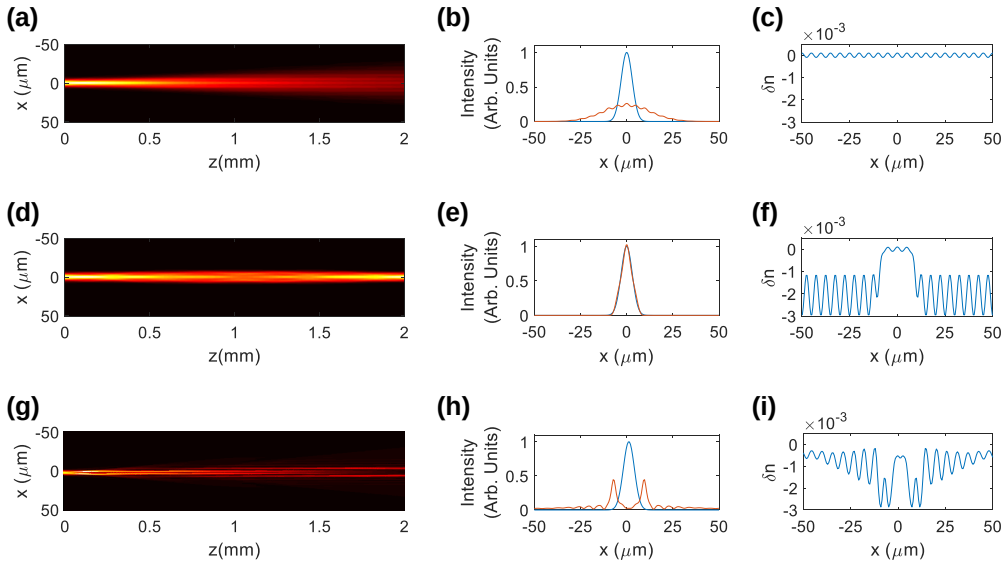

Figure 4.3. Numerical simulations of the gaussian beam propagation with FWHM= 8 μm. (a),(d),(g) Intensity distribution along $z = 2$ mm medium for linear, nonlinear ($E_0 = 4.1$ kV), zero-field-read-out propagation respectively. (b),(e),(h) Associated transverse intensity profiles for input (blu) and output (orange) and (c),(f),(i) index modulation patterns. The parameters of the simulation are $\lambda = 532$ nm, $n_0 = 2.4$, $I/I_b = 60$, $\delta n_0 = 10^{-4}$, $\epsilon_r = 1.3 \times 10^4$, $g_{eff} = 0.16$, $T_C = 21$ K, $T = 25$ K, $\delta T_C = 1$ K. Further details are in the text.

In Fig. 4.3, we show the propagation of a gaussian beam of FWHM= 8 μm. In the absence of the external field E_0, the beam diffract to FWHM= 30 μm after a linear propagation along 2 mm medium [Figs. 4.3(a),(b)]. The output profile of Fig. 4.3(b) has only a small modulation due to the little linear component of δn in Eq. (4.1) [Fig. 4.3(c)]. Applying $E_0 = 4.1$ kV/cm, the nonlinearity sustains the soliton propagation with the absence of periodic features [Figs. 4.3(d),(e)]. The phenomenon can be understood observing the δn pattern of Fig. 4.3(f): the modulation is almost absent in the area where the beam propagates, apart from the little linear contribution. To further understand the role of δn we study the case of which the δn is bigger where the light intensity is higher as in Fig. 4.3(i). Now the propagation is characterized by the presence of evident periodic structures

[Figs. 4.3(g),(h)]. Experimentally, this can be achieved by the so-called zero-field-read-out, a technique described below.

4.4 Experimental Results

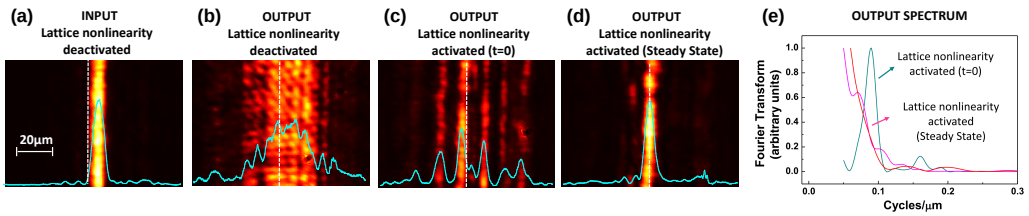

Figure 4.4. Observed beam dynamics from the starting delocalized discrete pattern to the continuous soliton. (a) Input and (b) output beam when the lattice nonlinearity is deactivated. (c) Output discrete spatial distribution as soon as the lattice nonlinearity is enabled at $V = 400$ V and (d) continuous soliton at the steady state. (e) Intensity Fourier transform of (b) (red line), (c) (cyan line) and (d) (magenta line).

The observed beam propagation dynamics inside the microstructured nonlinear lattice is shown in Figs. 4.4(a)-(d). When the electro-optical response is not activated through the bias field, the input Gaussian beam with full width at half maximum FWHM$= 7\ \mu$m experiences quasi-linear diffraction, resulting in an FWHM$= 26\ \mu$m output distribution [Figs. 4.4(a),(b)]. In these conditions, only the weak linear part of the lattice is involved in the beam propagation and, analyzing the spectrum [Fig. 4.4(e)], its affect on the beam is negligible. However, when the beam is exposed to the lattice nonlinearity, that is, the sample is biased, it instantaneously (at fast electro-optic response times) rearranges itself over the periodic index of refraction pattern. Considering the μW power used in the experiments, the photorefractive response begins changing the pattern only approximately 10-20 seconds after this initial stage. The discrete light distribution emerging in the first instants, before the light is able to produce the space-charge field, is shown in Fig. 4.4(c), for $u_0 = \sqrt{I_{peak}/I_B} \simeq 8$ and $V = 400$V, and appears delocalized compared to the input beam distribution. The operational temperature in this case is $T = T_C + 2$K, so that, from Eq. (4.1), we expect a nonlinear lattice with the same amplitude of the "homogeneous" photorefractive nonlinearity (Δn of the order of 10^{-3}). The build-up of the space-charge field causes the progressive local screening of the periodic lattice until the continuous steady-state soliton forms after few minutes [Fig. 4.4(d)]. The soliton transverse profiles have no trace of a periodic feature, so the lattice nonlinearity allows the transition from a discrete delocalized pattern to a continuous soliton. In Fourier space (transverse spatial spectrum), the spectrum of the output intensity distribution passes from having a dominant peak compatible with the lattice spatial frequency to a monotonous decaying behaviour without dominant resonances [Fig. 4.4(e)].

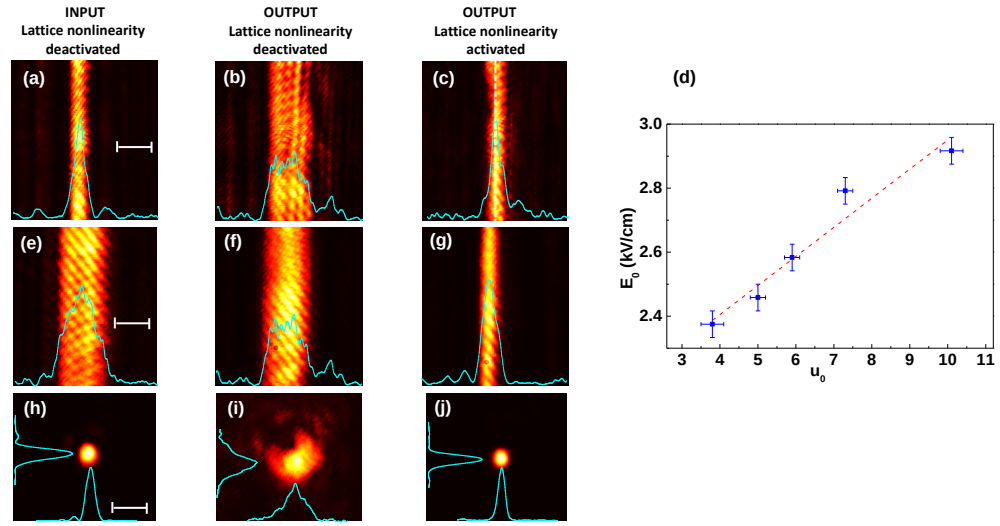

Figure 4.5. Experimental observation of the nonlinear propagation of 1D beams, with (a-c) FWHM= 7 μm and (e-g) FWHM= 22 μm, and 2D beams, with FWHM= 8 μm (h-j). Applying a bias field of 2.4 kV/cm the diffraction (b)(f)(i) associated to every inputs (a)(e)(h) is counterbalanced by the photorefractive nonlinearity of Eq. (4.1) and the continuous localization emerges (c)(g)(j). e) Experimental relation between normalized intensity and external field for the 1D solitons with linear fit.

The continuous soliton behaviour in the lattice nonlinearity is further demonstrated in Fig. 4.5. When no bias field is applied the input beam with FWHM= 7 μm experiences homogeneous diffraction resulting in an FWHM= 24 μm output distribution [Figs. 4.5(a),(b)]. Applying a V= 580 V static potential a steady-state soliton propagation is obtained for an intensity ratio $u_0 \simeq 5$. Fig. 4.5(c) demonstrates the absence of discrete features in the soliton state. This effect is independent both of the grating amplitude and of the beam width. The first statement is verified spanning the experimental soliton parameters (u_0, E_0) [Fig. 4.5(d)] and changing the operational temperature; in particular, we note that even when the lattice amplitude is larger than the standard photorefractive term the continuous picture remains unchanged. In fact, although we are not able to investigate this regime experimentally because close to T_c the external field needed for soliton formation induces the ferroelectric phase-transition, numerical simulations consistently indicate the formation of continuos solitons. Independence from the beam waist is demonstrated launching beams whose size covers several grating periods (weak-binding). As reported in Figs. 4.5(e)-(g), a FWHM= $22\mu m$, $u_0 = 2.5$ input beam weakly diffracts when unbiased; it self-focuses up to $8\mu m$ in the nonlinear case. Even in this case the output lacks marked discrete features, as numerically verified. We also demonstrate that what has been achieved occurs in the same spatial lattice geometry for two-dimensional solitons; a 2D continuous soliton, $8\mu m$ sized, is shown in Figs. 4.5(h)-(j) at $u_0 = 8.5$. Fig. 4.5(d) reports the relation between normalized intensity and external field for observed 1D solitons; the linear behaviour is

coherent with the general relationship in centrosymmetric media, even though the slope observed is considerably reduced, this underlining the fundamentally different nature of our present continuous solitons compared to conventional screening solitons [5].

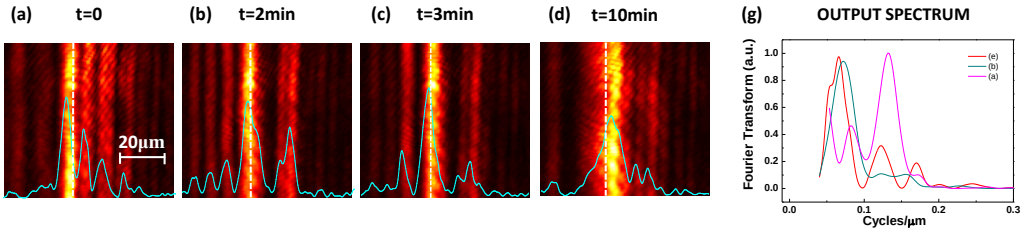

Figure 4.6. Zero-field discrete dynamics after the soliton formation. (a-d) Measured time evolution: (a-b) discrete delocalized pattern,(c) localization with discrete features and (d) relaxation to the equilibrium. (e) Comparison of the spectral properties of (a) (magenta line), (b) (cyan line) with those of the numerical output of Fig. 4.3(h) (red line).

This picture is expected to change if the electro-optical lattice can be decoupled from the photorefractive nonlinear response. Since these two responses act on different time scales, being the electro-optic modulation instantaneous with respect to the photorefractive one, the grating can be decoupled dynamically. This decoupling appears in the first stages of propagation into the lattice nonlinearity and leads to a discrete pattern, as discussed and reported in Fig. 4.4. However, this happens also for transient states after the soliton formation, when then bias field is removed. To further characterize the underlying nonlinear response, we carried out a zero-field-readout, as reported in Fig. 4.6. As the bias field is switched off after the steady-state is reached, previously guiding features become anti-guiding and vice-versa [5]. The effect evolves in time as the now diffracting beam washes out the original soliton-supporting space-charge distribution. So, in our case, removing the bias field causes the lattice to drop to zero everywhere except for in the region in proximity to the original soliton, where the space-charge field remains unshielded. The beam experiences the local nonlinear lattice and discrete features are now observable. We show the phenomena in Fig. 4.6, for the dynamics subsequent to the soliton propagation in Fig. 4.5(a). In the first stages [Figs. 4.6(a)-(b)] a discrete delocalized pattern takes place with some “waveguides” more excited than others. After this phase, the beam begins to modify the local index pattern and its propagation and interesting transient states can emerge. In Fig. 4.6(c) we show a transient discrete localization occurring 3 minutes after the bias field was removed. The nonstationary dynamics cause the localized pattern to spread, ultimately reaching its final equilibrium state, where normal diffraction is almost restored [Fig. 4.6(d)]. We also perform the spectral analysis of the zero-field evolution and we obtain the spectra of Fig. 4.6(e). Comparing the last with Fig. 4.4(e), we observe a similar evolution that is the spectrum progressively sheds off its peaks, show a consistent transfer of spectral content to the lower

frequency component. The characteristic frequencies are identified as the first harmonics of the lattice K and the spatial scale introduced by the beam waist [179].

In conclusion, we have demonstrated continuous on-axis soliton propagation in a lattice nonlinearity. The nonlinear photonic lattice is characterized by the electro-optic coupling with the soliton supporting nonlineariy and varies depending on the beam features. These results point out how the periodic properties of a media can be made to not emerge in the propagating waveform if they are filtered out by a strong interplay between the nonlinear waves and the nonlinear lattice.

On the other hand, this work opens new perspectives in condensed matter physics. The nonlinear embedded grating causes several new phenomena at the paraelectric-ferroelectric phase transition because it represents a constraint for the size and orientation of the ferroelectric domains. Probably the most evident effect is the conversion at T_C of the one-dimensional grating into a fully three-dimensional periodic structure that we call super-crystal. This phenomenon will be extensively discussed in the next Part of this Thesis.

Part II

Optics in nanodisordered ferroelectrics

In this Part 2 we focus our interest on the characteristics of the our materials. Unlike Part 1, here light is no more our matter of study but represents a probe to disclose the optical properties and ultimately the intrinsic structure of these crystals. In other words, in this Part 2, we mostly study the linear propagation, excluding some relevant exceptions, because we want to compare the response of our materials with well-known ones to underline the peculiarities of ours.

Our results are published in Ref. [180] and Ref. [181].

Chapter 5

Super-crystals in composite ferroelectrics

In this Chapter we discuss the peculiar properties of nanodisordered ferroelectrics often associated to their compositional disorder. In particular we introduce the super-crystal [101], a 3D lattice that emerges from the interplay between material order and disorder.

5.1 Ferroelectric Perovskites

The crystals that we use in this Thesis belong to the class of perovskites. The perovskite, properly speaking, is a mineral whose minimum chemical formula is $CaTiO_3$. In literature, any material that has the chemical formula of ABO_3 is called perovskite. In Fig. 5.1(a), we report the 3D structure of the cubic unit cell: there is one oxygen per each six face centres, the element A occupies the eight vertexes and the element B is placed in the center of the cube [182]. In general, element A is an alkaline metal or a rare earth whereas B is a transition metal. The chemical bonding is ionic with oxygens as anions and A and B as cations.

Perovskites play a relevant role in optics because they are transparent ferroelectric media, dielectric or semiconductor, that manifest a strong electro-optic and nonlinear response [173, 183, 184]. Ferroelectricity is the property of materials to have a spontaneous and reorientable electric polarization. Moreover, ferroelectric perovskites have two main phases, the Paraelectric Phase (PP) and the Ferroelectric Phase (FP), that are characterized by different behaviors and crystal symmetries [185].

Defining the Curie temperature, T_C, as the temperature of the phase transition, for $T < T_C$ we are in the FP whereas for $T > T_C$ we are in the PP and the crystal behaves like a common isotropic dielectric, e.g. without hysteresis. From a microscopic point of view, the phase transition corresponds to a structural rearrangement of the elementary cell from the centrosymmetric cubic PP to a noncentrosymmetric orthorhombic FP. To minimize the free

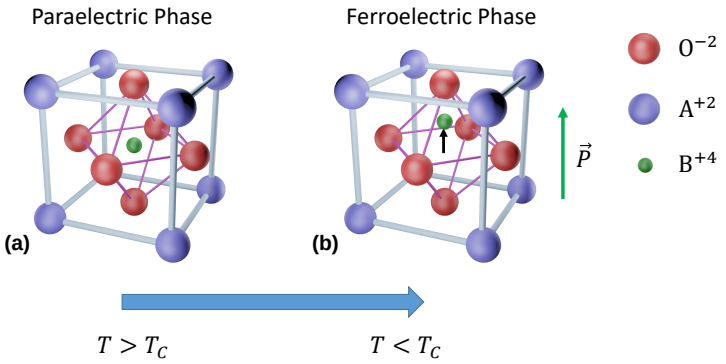

Figure 5.1. Three-dimensional structure of the perovskite unitary cell. (a) Structure for the paraelectric phase. (b) Structure for the ferroelectric phase with the displacement of the central cation that causes the spontaneous polarization $\vec{P}$.

energy, the transition to PF is accompanied by the displacement of the central cation towards the center of one of the six faces of cubic cell , see Fig. 5.1(b). The broken symmetry leads to the appearance of a local spontaneous dipole moment strongly influenced by the polarization of the neighbours. The net effect is the creation of macroscopic polarization clusters. This phase transition can be ascribed as both first and second order transition according to Ehrenfest classification [186]. To take into account the spontaneous polarization, we can consider the electric susceptibility χ_r as the order parameter and, as expected, it diverges as the temperature approaches T_C (from PP) according to the Curie-Weiss law:

$$\chi_r = \frac{C}{T - T_C}, \tag{5.1}$$

where C is the material-specific Curie constant. Eq. (5.1) states that for $T \gg T_C$ the polarization of the system is globally zero. For $T \sim T_C$, χ_r diverges and values of $\chi_r > 10^5$ are actually measured; the phenomenon is associated with the divergence of correlation length, that is the system has a strong collective response. An important consequence of this is that the material, at the transition, manifest the so-called critical opalescence, i.e. a huge scattering caused by border of the domains whose size is comparable to wavelength, impeding the light propagation. For this reason, usually experiments are performed some degree above T_C to have a transparent medium and to exploit the elevated χ_r [1–3, 44].

5.2 Polar Nano Regions and Relaxors

The introduction of compositional disorder can change the properties of the crystals, e.g, preventing the long-range correlations of ferroelectric domains and allowing propagation also upon the phase transition. The disorder turns an ordinary ferroelectric crystal into a relaxor ferroelectric or, simply, relaxor [187, 188]. From a microscopical point of view, the disorder is produced by the chemical substitutions of ions of different valences than the host ions leading to the formation of lattice defects or also substitutions of ions with other with the same valence but different size generating an asymmetry of the cubic cell that causes a dipole moment. The final effect is the the existence of a unique polar structure made by polar nanometer-size regions (PNRs) that enhances the response of the material to external stimuli [185]. PNRs, indeed, are known to form the basis for remarkable optical responses of both fundamental and technological interest, such as randomly-matched second harmonic generation [189–191], the giant photorefractive nonlinearities [42, 61, 100, 108, 192, 193], giant quadratic electro-optic coefficients [62, 183, 194–196], strong electromechanical coupling [197] and the anomalous electro-optic effect [173, 198, 199].

Relaxors properties are governed by the crystal temperature. For temperature $T \gg T_C$ relaxors behave like ordinary ferroelectrics in their PP. Cooling the system to the so-called Burns temperature T_B, with $T_B > T_C$, the PNRs appear. This is a glassy state, with randomly distributed directions of dipole moments, and ergodic behavior [200]. Even if we are formally in the PP (at T_B there is not an actual structural phase transition), the unique physical properties of this state often induce to consider the medium at $T_C < T < T_B$ in a new phase, different from the PP [188]. An evidence of this is that, for $T < T_B$, the material does not follows the Curie law [Eq. (5.1)] and this fact is used to define T_B itself as done in Fig. 5.2. Here we report an example of the χ_r vs T plot obtained through the dielectric spectroscopy performed on a relaxor sample, specifically a sodium-potassium-tantalate-niobate (KNTN) crystal. As previously mentioned for ordinary ferroelectric, we observe values of $\chi_r > 9 \times 10^3$ but here we also note two of the main characteristic of relaxor: the broad PP-FP transition and its frequency dependence.

The broad phase transition makes it possible to exploit the high χ_r in the transparent PP. On the other hand T_C (the value estimated from the Curie law in PP) is no longer suitable to describe the transition and, usually, the temperature T_{max} of the peak is adopted, as illustrated in Fig. 5.2. The temperature T_{max} is only approximately, indeed, as we can see in the inset, measurements taken with different electric field frequencies change the peak χ_r value and the actual T_{max}. This phenomenon is described by the Vogel-Fulcher law:

$$f = (2\pi\tau_0)^{-1} e^{\frac{-E_a}{k_B(T-T_{VF})}}, \tag{5.2}$$

where f is the measurement frequency and τ_0, E_a and T_{VF} are fitting parameters [201].

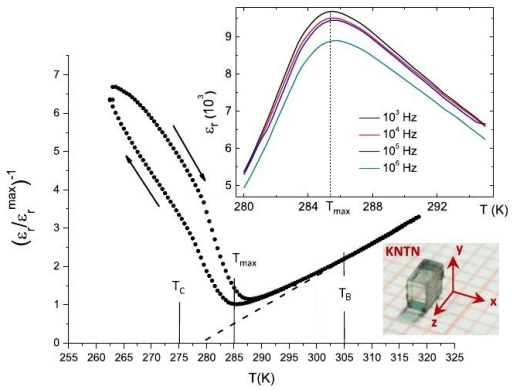

Figure 5.2. Experimental measurements of $\varepsilon_r = \chi_r + 1$ through dielectric spectroscopy for a relaxor ferroelectric KNTN. The position of the temperatures T_C, T_B, T_{max} are in agreement with the definitions provided in text. In the inset is reported a magnification of the broad relaxor transition around T_{max} to emphasize the dependence of ε_r to the electric-field frequency. (From Ref. [62]).

The Vogel-Fulcher law is known to hold for spin-glasses and, associated to relaxors, makes them test beds for the experimental study of dipole glasses [188].

Another useful parameter to describe relaxors is the freezing temperature T_f, with $T_C \lesssim T_f < T_B$, that is the temperature under which the ergodic regime ceases and PRNs remain in a frozen state. The dipole relaxation time τ is strongly temperature dependent and the modified Arrhenius law holds [188]:

$$\tau = \tau_\infty e^{\frac{E_b}{k_B(T-T_f)}} \tag{5.3}$$

where τ_∞ and E_b are parameters and for $T_f = 0$ the proper Arrhenius law is recovered. Eq. (5.3) establishes that τ grows when $T \sim T_f$ and tends to $\tau = \infty$ for $T = T_f$. This mean that the system at $T < T_f$ cannot reach the equilibrium state but remains in a metastable state. We remark that this metastable state is not always the same but is correlated by the previous history of the sample, i.e. thermal cycles, electric field application or observation time. A direct consequence of this is, in Fig. 5.2, the existence of a hysteresis loop, that is, different values of χ_r are obtained in cooling and in heating. We note that although Eq. (5.2) and Eq. (5.3) have similar structure, the connection between them is not straightforward and still debated [188].

A last noteworthy feature of many relaxors is their peculiar anisotropic response, that is, different behaviors for propagation along the three crystalline axes [202]. An example of this is reported in Fig. 5.3, here the dielectric spectroscopy on a KNTN crystal shows directional anisotropy also in the nominally cubic phase. These observations are attributed to the alteration of polarization and internal strain induced during the sample growth. Moreover,

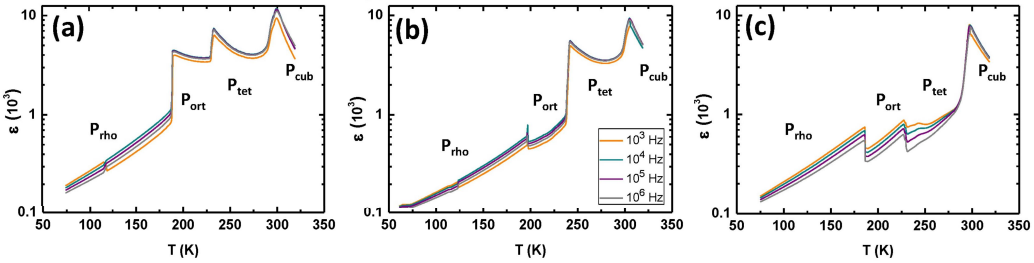

Figure 5.3. Relative permittivity as function of the measured temperature for several electric field frequencies (we recall that $\varepsilon_r = \chi_r + 1$). The experiment is performed during the heating stage along the three crystalline axes: a (a), b (b) and c (c). (Adapted from Ref. [202]).

the slightly different transition temperature is associated to a hysteretic effect [202].

In the following Chapters we optically study the relaxor features of our samples. We provide evidences of crystal anisotropy, with direction-dependent linear and nonlinear propagation. Furthermore, we report the anomalous behaviors in proximity or just below the PP-FP transition, i.e. the giant refractive index and the polarization modulation.

5.3 Spontaneous Ordered Phase Transition

In the last section we have observed evidence of the anisotropic response of a ferroelectric relaxor, a spontaneous symmetry breaking that depends on the crystal axis and temperature. Furthermore, we have shown that the PP-FP transition generally leads to a disordered mosaic of polar domains that permeate the finite samples [203].

Here we report a different phase transition associated with coherent and ordered ferroelectric domains. In detail we discuss the spontaneous formation of an extended coherent three-dimensional (3D) superlattice in the nominal ferroelectric phase of specifically grown potassium-lithium-tantalate-niobate (KLTN) crystals [3]. Visible light propagation reveals a polarization pattern with a micrometric lattice constant, a counterintuitive mesoscopic phase that naturally mimics standard solid-state structures but on scales that are thousands of times larger and, for these reasons, we call it Super-Crystal (SC).

5.3.1 Super-Crystal Observation

The phenomenon is achieved using a compositionally disordered ferroelectric crystal with an oscillating composition along the growth axis achieved using an off-center growth technique in the furnace [175, 204]. The sample, the same of Chapter 4, has the grating period $\Lambda = 5.5$ μm [Fig. 4.2(b),(c)].

When the crystal is allowed to relax at $T = T_C - 2$ K, i.e., in proximity of the spatially averaged room-temperature Curie point $T_C = 294$ K, laser light propagating through

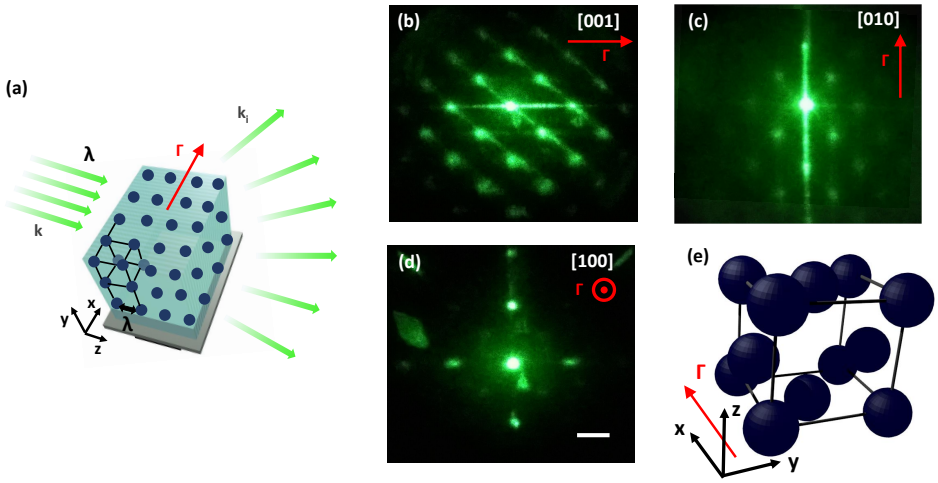

Figure 5.4. Super-crystal patterns. (a) Sketch of the light propagates inside the periodic KLTN. (b)-(c) SC light distribution obtained from a plane wave that propagates inside the KLTN at $T = T_C$. The images represent the Fourier transform of the micrometric domains organization. (Adapted from Ref. [101]).

the sample suffers relevant scattering with strongly anisotropic features [see Figs. 5.4(a)-(d)]. Typical results are reported in Fig. 5.4(b)-(d), and appear as an optical analogue of x-ray diffraction in low-temperature solids. This optical diffractometry provides basic evidence of the 3D SC at micrometric scales. Probing the principal crystal directions reveals several diffraction orders that map the entire reciprocal space. The large-scale SC, that permeates the whole sample, overlaps - along the x-direction - with the built-in compositional oscillating seed. The SC extends in full three-dimensions, with the same periodicity $\Lambda = 5.5$ μm of the x-oriented compositional oscillation, also along the orthogonal y and z-directions. In particular, Fig. 5.4(d) indicates that in the plane perpendicular to the built-in dielectric microstructure $\mathbf{\Gamma}$ vector, i.e., where spatial symmetry should be unaffected by the microstructure in composition, the ferroelectric phase-transition leads to a spontaneous pattern of transverse scale Λ. The corresponding elementary structure on micrometric spatial scales is reported in Fig. 5.4(e); it can be represented as an fcc-cubic structure in which the occupation of one of the three faces ($z - y$ face) is missing [205]. The structure can be reduced to an simple cubic structure with a three-fold basis and lattice parameter $a = \Lambda$.

As the crystal is brought below the average Curie point, it manifests a metastable (super-cooled) and a stable (cold) phase, as analyzed in Fig. 5.5 both in the reciprocal (Fourier) and direct (real) space. In the nominal paraelectric phase, at $T = T_{\mathrm{C}} + 2\mathrm{K}$ [Fig. 5.5(a)], we observe the first Bragg diffraction orders (± 1) consistent with the presence of the seed

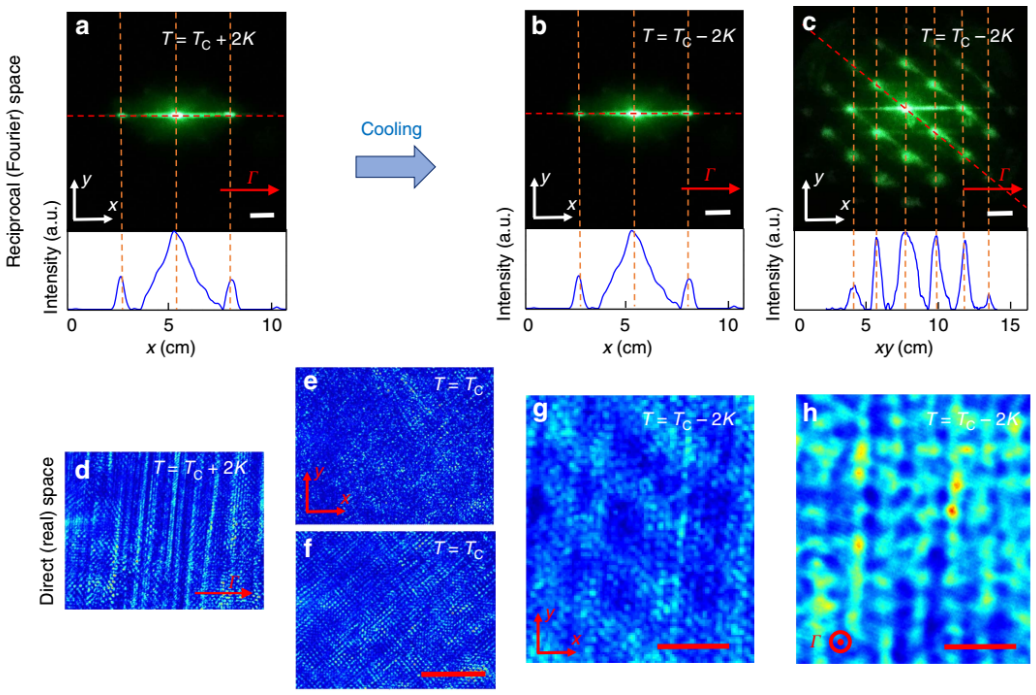

Figure 5.5. Light diffraction above and below T_C. (a) Reciprocal space probed at $T = T_C + 2$ K (hot paraelectric phase), showing the first diffraction orders due to the one-dimensional sinusoidal compositional modulation. Cooling below the critical point results at $T = TC - 2$ K (super-crystal ferroelectric phase) in (b) a supercooled (metastable) 1D superlattice with the same diffraction orders that relaxes at the steady state into (c) the cold (stable) super-crystals. In both b,c the direction of incident light is othogonal to $\vec{\gamma}$, as in a. (d–h) Corresponding transmission microscopy images revealing (d) unscattered optical propagation, (e,f) scattering at the phase transition, (g) unscattered optical propagation in the metastable superlattice and (h) periodic intensity distribution underlining the 3D superlattice. Metastable and stable (equilibrium) phases are inspected, respectively, at times $t \approx 1$ min and $t \approx 1$ h after the structural transition at $T = T_C$. Bottom profiles in a–c are extracted along the red dotted line. Scale bars (a–c), 1.2 cm, (d–f), 100 μm and (g,h), 10 μm.(From Ref. [101]).

microstructure, a one-dimensional transverse sinusoidal modulation acting as a diffraction grating; the distance from the central 0-order fulfils the Bragg condition,that is, scattered light forms an angle $\theta_{\mathrm{B}} = \lambda/2n_0\Lambda \simeq 7^\circ$ with the incident wavevector $\mathbf{k}$. Crossing the ferroelectric phase-transition temperature T_{C} we detect a supercooled metastable state that has an apparently analogous diffraction effect [Fig. 5.5(b)] that is dynamically superseded by the stable and coherent cold SC phase [Fig. 5.5(c)], in which spatial correlations are extended to the whole crystal volume. In real space, transmission microscopy shows unscattered optical propagation through the paraelectric sample at $T = T_{\mathrm{C}} + 2$ K [Fig. 5.5(d)], that turns into critical opalescence and scattering from obliques random domains at the structural phase transition [Fig. 5.5(e)-(f)], and in unscattered transmission in the metastable ferroelectric phase at $T = T_{\mathrm{C}} - 2$ K [Fig. 5.5(g)]. After dipolar relaxation has taken place, the cold SC appears in this case as a periodic intensity distribution on micrometric scales, as shown in Fig. 5.5(h).

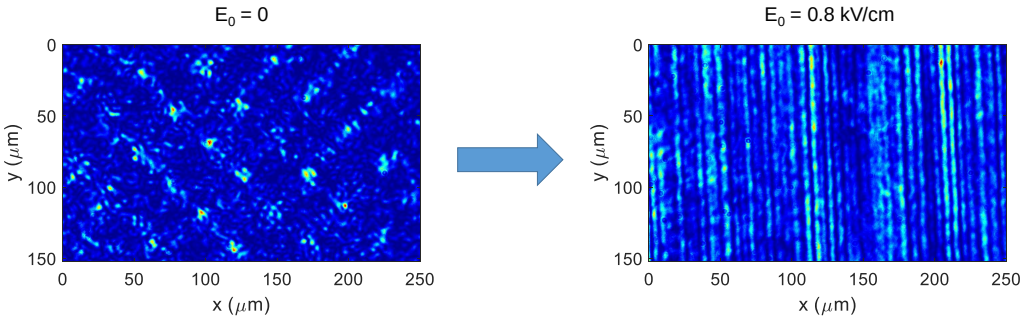

Figure 5.6. Direct space images of the super-crystal at $T = T_C - 3$ K (left) before and (right) after the application of $E_0 = 0.8$ kV/cm external electric field along the x-axis.

The metastable SC state survives only around the critical temperature T_C. In fact, the brightness of the SC spots decreases cooling the sample and for $T \sim T_C - 10$ K the SC disappears. Furthermore, also an external electric field $E_0 \simeq 0.8$ kV/cm can induce the SC a transition to the PP, as showed in Fig. 5.6. We point out that, removing $E_0 = 0$, the SC does not restore.

5.3.2 Super-Crystal Model

An interesting point arising from the experimental results and analysis is how the periodically-ordered polarization state along the x-direction leads to the SC. Since we pass spontaneously from a metastable to a stable mesoscopic phase, polar-domain dynamics in presence of the fixed spatial scale Λ play a key role. In fact, we note that the 1D super-lattice sketched in Fig. 3(c) involves the appearance of charge-density and associated strains between polar planes, so that the ferroelectric crystal naturally tends to relax into a more

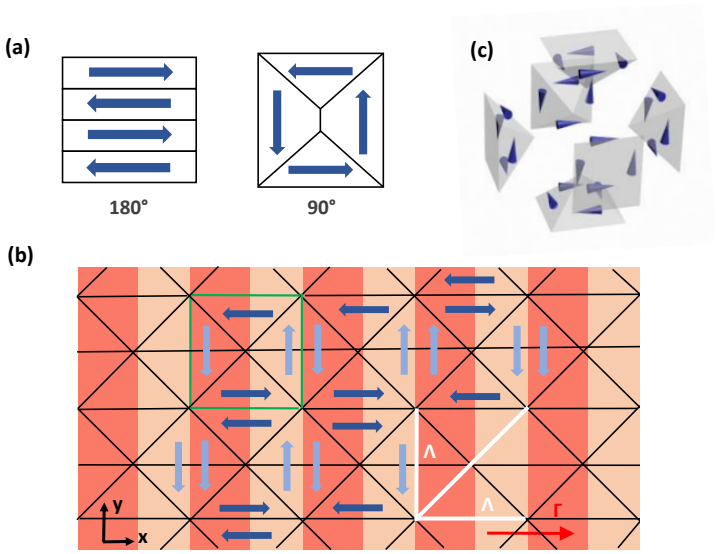

Figure 5.7. Polar-domain configuration underlying the 3D superlattice. (a) Typical 180° and 90° domain configurations in perovskites ferroelectrics. (b) Planar domain arrangement scheme in the stable super-crystal phase obtained with elementary blocks of 90° configurations (green cell). In this periodically-ordered ferroelectric state the compositional modulation (as for Fig. 3(c)), other domain walls ruling optical diffractometry (black lines), and periods along x,y and xy-axis (white bars) are highlighted. Vertical polarizations have a lighter color to stress their weak optical response in our KLTN sample. (c) Extension of the single unit-cell (green cell in (b)) in three dimensions.

stable configuration. In standard perovskites, equilibrium configurations are mainly those involving a 180° and 90° orientation between adjacent polar domains, as schematically shown in Fig. 5.7(a). To explain the 3D polar-state and its periodical features underlying the SC, we consider the 90° configuration, which is characterized by 45° domain walls that we observe in a disordered configuration during the ferroelectric phase transition at T_{C} [Fig. 5.5(f)]. Due to the periodic constraint along the x-axis, this arrangement has the unique property of reproducing our observations, minimizing energy associated to internal charge-density, and transferring the built-in 1D order to the whole volume with the same spatial scale Λ. We illustrate the domain pattern in Fig. 5.7(b) for the $x-y$ plane, whereas in Fig. 5.7(c) the elementary cell is shown in the three-dimensional case, where it maintains its stability features in terms of charge-density energy. In particular, in Fig. 5.7(b), domain walls resulting in the diffraction orders of Fig. 5.4(b) are marked, as well as the 45° correlation period, that agree with optical observations of the reciprocal space. We further stress that vertical domains [light blue in Fig. 5.7(b)] are optically analogous to paraelectric regions; moreover, 180° rotations in the polarization direction in each polar region has no effect on the optical response. In view of the symmetry of this arrangement, the observed diffraction anisotropy [Fig. 5.4(d)] is then associated to the absence of grating-planes in the $y-z$ face.

In the next chapters we illustrate other peculiar properties of the SC. We extensively use the 3D structure developed here to explain most of the observed phenomena.

Chapter 6

Observation of polarization-maintaining light propagation in depoled compositionally disordered ferroelectrics

Here the super-crystal is studied from the point of view of the optical birefringence. We report experimental measurements of both global and local Stokes parameters, varying the input light polarization and the temperature. Results indicate the existence of a polarization grating that gradually disappears as the ferroelectric state reduces to a disordered distribution of polar nanoregions above the critical point. This analysis represents an important step to understand the proprieties of ferroelectric domains and makes birefringence as an important tool to reveal the phase transition.

6.1 Light Polarization in Anisotropic Media

The polarization of light is strongly affected by anisotropy, the paradigm being the birefringence observed in non-centrosymmetric crystals, such as ferroelectrics [203], where the index of refraction depends on the polarization and propagation direction. In a full three-dimensional scenario, birefringence can also affect wave propagation, not only introducing coherent scattering [206], but even engendering localized guided modes.

PNRs, in relaxor material, generally form a disordered three-dimensional mosaic for which optical birefringence experiments indicate average local symmetry breaking, providing a tool for the study of possible non-ergodic behavior and dipolar-glass dielectric relaxation

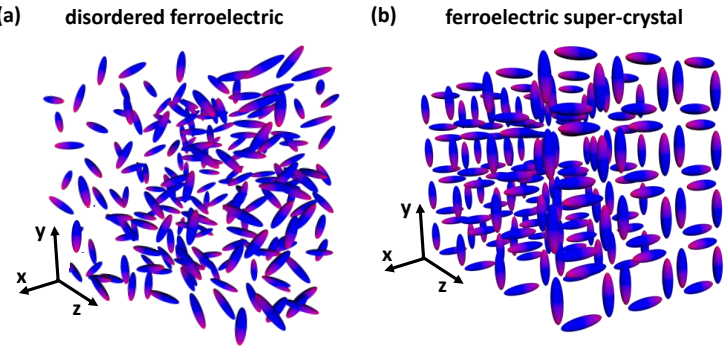

Figure 6.1. Schematic of different spontaneous ferroelectric states. (a) Three-dimensional disordered distribution of polar domains. (b) Example of a volume polar structure underlying a ferroelectric super-crystal.

[207–210]. In turn, the presence of large polar domains below the Curie point or in the paraelectric phase under high electric field [194], causes complete depolarization of propagating optical fields, a result of multiple interference of random scattered waves. This complicates the use of giant ferroelectric response in photonic applications, whether these be based on quasi-phase-matching and nonlinear electronic susceptibility or simply the electro-optic response [158, 211–214]. In recent studies, conditions have been found in which the polar-nanoregion mosaic spontaneously settles into a three-dimensional coherent and periodic structure, a ferroelectric super-crystal with intriguing optical diffraction properties [101]. In this case, interesting effects are expected to emerge in light-polarization dynamics from the interplay of mesoscopic domain ordering and anisotropy, all this in a volume scenario.

Here, spontaneous polarization leads to a periodic three-dimensional polar lattice with strong inhomogeneity and anisotropy at the micrometer scale. Polarimetric experiments indicate that, in distinction to pure depoled ferroelectrics, light propagates fully polarized for a linear polarization along the super-crystal principal axes. Analyzing the wave spatial distribution, we found the effect to be associated with the formation of speckle distributions of alternating orthogonally polarized states that spatially separate the input polarization into its linear polarization components parallel to the principal super-crystal axes. Precursors of the phenomenon are observed also above the Curie point, where the ferroelectric super-crystal vanishes, thus indicating preferred orientations of polar-nanoregions.

To grasp the physics underlying the polarization dynamics reported, we note that a three-dimensional disordered mosaic of anisotropic domains, as schematically shown in Fig. 6.1(a), dephases the components of an incident optical field according to the local random optical axis, so as to scatter and depolarize the transmitted light irrespective of its input polarization state. In turn, an ordered volume pattern of polar domains, such as the one encountered in a ferroelectric super-crystal and illustrated in Fig. 6.1(b), where each

lattice cell may host a so-called Kittel-like vortex [101], leads to a qualitatively different polarization evolution. In fact, in this case ferroelectric anisotropy is inhomogeneous but the local optical axis is on average aligned along the super-crystal structure.

6.2 Experimental Setup

In our experiments we used super-crystals formed in two different composite ferroelectrics to demonstrate the generality of the polarization-maintaining scenario. The sodium-potassium-tantalate-niobate (KNTN) super-crystal was obtained allowing a $K_\alpha Na_{1-\alpha} Ta_\beta Nb_{1-\beta} O_3$ ($\alpha = 0.85$, $\beta = 0.63$) solid-solution crystal to equilibrate for approximately 30 minutes below its ferroelectric-paraelectric Curie point $T = T_c - 3$ K, with $T_c = 293.5$ K. The crystal

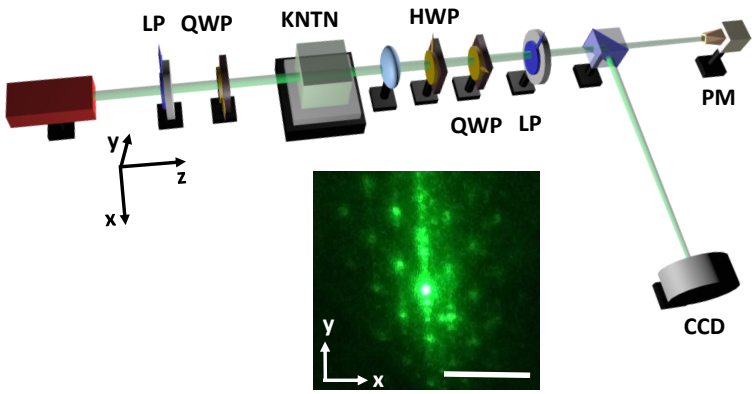

Figure 6.2. Sketch of the experimental setup: linear polarizer (LP), quarter-wave plate (QWP), half-wave plate (HWP), power meter (PM) and imaging camera (CCD). The inset shows the optical diffraction pattern of the ferroelectric super-crystal embedded in the KNTN sample. Scale bar is 5 mm.

is grown through the top-seeded solution method by extracting a zero-cut optical-quality 2.1 mm by 2.5 mm by 2.6 mm specimen (along the x,y,z axes). The lithium-potassium-tantalate-niobate (KLTN) super-crystal emerged from the equilibration of a 2.4 mm by 2.0 mm by 1.58 mm $K_\alpha Li_{1-\alpha} Ta_\beta Nb_{1-\beta} O_3$ ($\alpha = 0.96$, $\beta = 0.62$) with $T_c = 294$ K. Dielectric response for both samples is detailed in Refs. [202, 215] and the super-crystal formation process is reported in Ref. [101]. In Fig. 6.2 we show the optical diffraction pattern observed for the KNTN super-crystal: discrete spots fill the Fourier space and signal a periodic micrometric order on large scales (≈ 25 μm) in the sample volume.

Polarization evolution in ferroelectric super-crystals is investigated through conventional Stokes parameter measurements [216, 217], performed using the setup shown in Fig. 6.2. A beam from a Nd:Yag laser ($\lambda = 532$ nm, 150 mW) is expanded so as to form a plane wave propagating along the z direction and whose input polarization state is fixed using

a linear polarizer and a half-wave plate. The output polarization state is analyzed using a half-wave plate, quarter-wave plate, and a linear polarizer placed after the sample. This allows the decomposition of the field into its Stokes components, i.e., horizontal (parallel to the x axis) S_H, 45 degrees S_{45} and right-circular S_R from the optical intensity detected through a power meter and a CCD camera.

6.3 Global Stokes Parameter Measurements

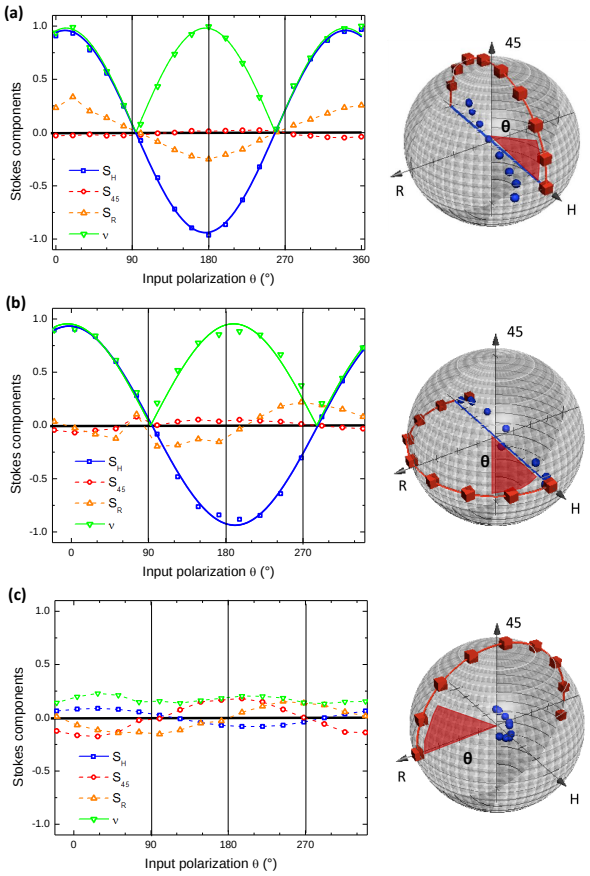

Figure 6.3. Light-polarization dynamics in the KNTN super-crystal. (a-c) Stokes parameters measured varying the input polarization state along equators of the Poincaré sphere through the angular coordinate θ. Blue squares indicate the horizontal component of the polarization, red circles the $45°$ one, orange and green triangles are, respectively, the right-handed part and the degree of polarization ν. Solid lines are fitting functions (see main text) and dashed lines serves as guides. Insets show the corresponding input (red cubes) and output (blue spheres) states in the Poincaré space.

Results for the KNTN super-crystal are reported in Fig. 6.3 varying the input polarization state along different trajectories on the Poincaré sphere. In Fig. 6.3(a) is shown the behavior of a linear polarization; the degree of polarization $\nu = \sqrt{S_H^2 + S_{45}^2 + S_R^2}$ is observed to

strongly depend on the polarization direction θ of the field. In particular, light remains fully polarized and ν is maximum for a field parallel to the x or y axis ($\theta \simeq 0°, 180°$), whereas complete depolarization occurs in the conjugate points ($\theta \simeq 90°, 270°$). For intermediate values of θ, evolution of the horizontal component is well fitted by $S_H(\theta) = \cos\theta$ (blue line in Fig. 6.3(a,b)). Moreover, the transmitted light maintains a polarized fraction that almost coincides with S_H, that is, $\nu(\theta) = |\cos\theta|$ [green line in Fig. 6.3(a,b)]. An analogous evolution is observed for an elliptical input state oriented along the x axis [Fig. 6.3(b)]. In this case, the circular components completely depolarize whereas the linear horizontal and vertical ones propagate unaffected in the spatially inhomogeneous ferroelectric structure. Moreover, the output field is always depolarized ($\nu \simeq 0$) along a trajectory on the Poincaré sphere orthogonal to the H axis [Fig. 6.3(c)]. The whole picture is observed in both super-crystals, is found to be independent of the laser wavelength (532-633 nm) and crystal orientation, and occurs equally for light propagating along the x and y directions of the sample. This suggest a strong connection between the observed depolarization and the one reported in electro-optic experiments in similar crystals in proximity of T_c under large electric field [62, 183, 193, 194], an effect that has been only partially understood.

6.4 Spatially Resolved Experiments

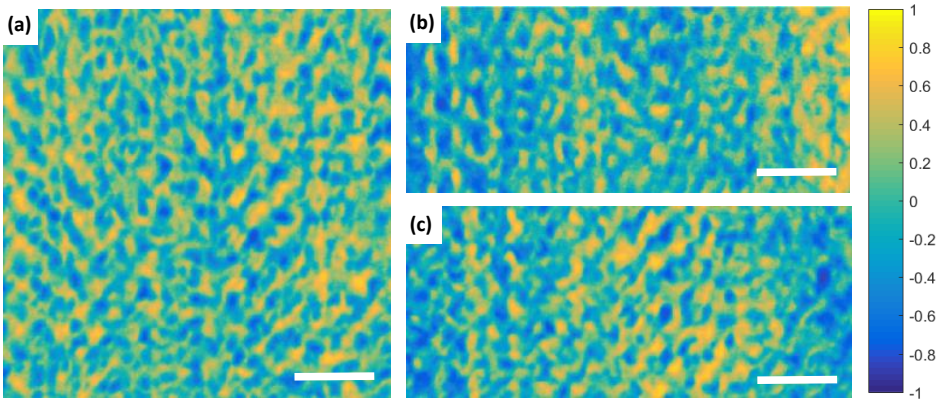

Figure 6.4. Evidence of a locally-polarized speckle lattice. Stokes parameter maps showing the transmitted (a) S_H (b) S_{45} and (c) S_R local components for a linear input polarization with $\theta = 90°$. Scale bar is 20 μm.

To pinpoint the underlying mechanism we perform spatially-resolved Stokes parameter maps of the transmitted light. In Fig. 6.4(a) we report the detected S_H for the significant case of a linearly polarized [$\theta = 90°$ in Fig. 6.3(a)] input wave from a He-Ne laser ($\lambda = 633$ nm, 15 mW) propagating along the z direction of the KLTN super-crystal. We observe a speckle-like distribution arising from scattering during propagation. However, in

contrast to what is expected for depolarized light from scattering, speckles distribute on a periodic lattice with approximately 6 μm lattice constant that coincides with the super-crystal structure. A similar speckle lattice is found for the S_{45} and S_R map, Fig. 6.4(b) and Fig. 6.4(c), respectively. Interestingly, while the global degree of polarization is $\nu \simeq 0$, the degree of polarization measured averaging on each spatial point is $\nu \simeq 0.7$. Therefore, the output polarization state consists of a mixture of spatially-separated polarized states. This indicates how inhomogeneity of the medium introduces a local phase difference between orthogonal polarization components that strongly varies in space. A macroscopic Stokes measure (Fig. 6.2) averages out these local phases so that the field appears as depolarized although horizontal and vertical components are maintained during propagation. The optical polarization lattice closely follows the super-crystal, and this demonstrate a principal role played by the underlying ferroelectric state [see Fig. 6.1(b)].

6.5 Temperature Varying Measurements

To further test the role of ferroelectric domains, we perform polarimetric transmission experiments varying the crystal temperature, so as to introduce strong fluctuations in super-crystal order, ultimately crossing the Curie temperature to restore global inversion symmetry in the paraelectric phase. As reported in Fig. 6.5(a) for the dynamics of a linearly polarized

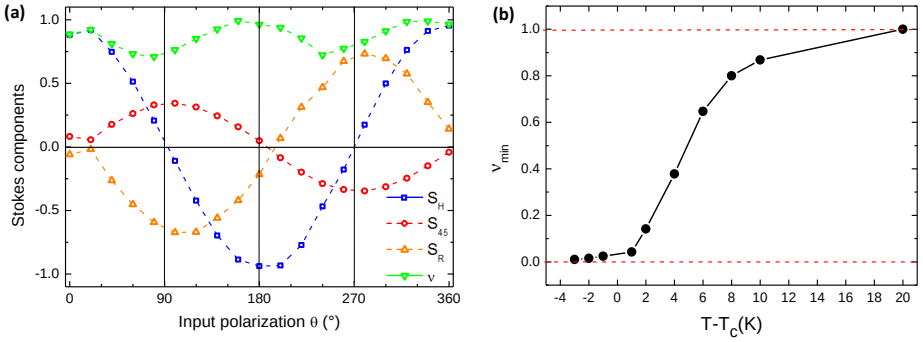

Figure 6.5. Partial depolarization from polar-nanoregions. (a) Stokes parameters measured in the nominal paraelectric phase ($T = T_c + 6$ K) for propagation along the x direction of the KNTN crystal. Inputs are linearly polarized, that is, θ varies along the equator of the sphere in Fig. 6.3(a). (b) Minimum degree of polarization ν_{min} for measurements as in (a) versus $T - T_c$.

input state in KNTN (see Fig. 6.3(a) for a comparison), the average depolarization of the input wave appears less pronounced at $T = T_c + 6$ K. Although ν still depends on θ, its minimum at $\theta \approx 90°$ no longer vanishes. Although the main Stokes component remains S_H, other components become significant. Polarization evolution now is found to depend on the length of the sample along the propagation axis and on λ, suggesting a macroscopic

birefringence of the hosting paraelectric medium. This is consistent with the fact that above the Curie point the super-crystal is superseded by a disordered distribution of PNRs [173, 196–199] that acts as a precursor of the macroscopic phase transition, so that no macroscopic index of refraction periodic lattice emerges. As reported in Fig. 6.5(b), the corresponding minimum degree of polarization (ν_{min}) increases as temperature moves away from the critical point, an order parameter further underlining the role of the ferroelectric inhomogeneous structure. At $T = T_c + 20$ K, where the crystal appears no longer affected by polar-nanoregions (proper paraelectric phase), $\nu = 1$ for all input polarizations.

in conditions for which an ordered three-dimensional polar-lattice is embedded in the material. Experiments above the Curie temperature, then, suggest that polar nanoregions have preferred orientations along the crystal axes, a fact that may play a crucial role in phenomena involving the giant electro-optic and giant piezoelectric effect. Our results demonstrate how ordered polar domains can coherently modify the polarization of light, possibly enabling the use of the unconventional ferroelectric properties in photonic applications based on polarization control.

Chapter 7

Second Harmonic Generation in nanodisordered ferroelectrics

Second Harmonic Generation (SHG) is one of the paradigmatic effects in nonlinear optics. It is fundamental in many applications from SHG microscopy [218] to laser sources, allowing laser emission for frequencies not accessible from high-efficiency electronic transitions [216]. In this Chapter we illustrate the very recent findings about SHG, made on nanodisordered perovskites and the role that SHG can play to unveil the hidden structure of these materials.

7.1 Second Harmonic Generation

SHG represents the conversion of a field E_1, the pump, with frequency $\omega_1 = \omega$ into a field E_2, the signal, with frequency $\omega_2 = 2\omega$. SHG is a second-order effect and only materials with the proper symmetry, and polarization, allow it. Indeed, we have to recall that, in general, the *i*-th component of the second-order polarization vector with frequency $\omega_n + \omega_m$ is connected with the fields with frequency ω_n and ω_m by the the susceptibility tensor [219]:

$$P_i(\omega_n + \omega_m) = \varepsilon_0 \sum_{jk} \sum_{(nm)} 2 d_{ijk} E_j(\omega_n) E_k(\omega_m), \tag{7.1}$$

where we use the contracted notation for the susceptibility tensor d_{ijk} and $\sum_{(nm)}$ is to consider all the possible permutation of the indexes.

To derive the formulas of the SHG, we solve the Maxwell equations (1.1) releasing the constraint of monochromatic field. After some simply considerations, we obtain the wave equation [219]:

$$\nabla^2 \vec{E}_n(\vec{r}) + \frac{\omega_n^2}{c^2} \varepsilon^{(1)} \vec{E}_n(\vec{r}) = -\frac{\omega_n^2}{\varepsilon_0 c^2} \vec{P}_n^{NL}(\vec{r}), \tag{7.2}$$

where the subscript $n = 1, 2$ indicates the components with frequency $\omega_n = \omega_1, \omega_2$

respectively and P_n^{NL} states for the nonlinear part of the polarization vector. We have written $\varepsilon^{(1)}$ to recall that this is the linear contribution of the dimensionless relative permittivity.

Assuming to be in a lossless medium, the solution of Eq. (7.2) for $\vec{P}_n^{NL}(\vec{r}) = 0$, is the plane wave $E_n(z, y) = A_n \exp(ik_n z - \omega_3 t)$ with $k_n = n_n \omega_n / c$ and $n_n^2 = \varepsilon^{(1)}(\omega_3)$. To extend this solution to the complete Eq. (7.2), we can replace the constant wave amplitude A_n with a slowly varying function of z that is $A(z)$ and we obtain $E_n(z, t) = A_n \exp(ik_n z) \exp(-i\omega_n t) + (c.c.)$. In this hypothesis there is no more dependence on the transverse coordinates x and y and we can replace ∇^2 by d^2/dz^2. Now we focus our attention on the equations for the field at frequency ω_2. Following Eq. (7.1), the polarization can be expressed through the effective value of the susceptibility tensor d_{eff} [219]:

$$P(2\omega) = 2\varepsilon_0 d_{\text{eff}} E^2(\omega). \tag{7.3}$$

From all of the previous considerations and performing the slowly varying amplitude approximation (SVEA)[1], we can handle Eq. (7.2) as follows:

$$\frac{dA_2}{dz} = \frac{i\omega_2^2 d_{\text{eff}}}{k_2 c^2} A_1^2 e^{i(2k_1 - k_2)z}. \tag{7.4}$$

For the field E_1 we can repeat all the above passages and we obtain:

$$\frac{dA_1}{dz} = \frac{2i\omega_1^2 d_{\text{eff}}}{k_1 c^2} A_2 A_1^* e^{-i(2k_1 - k_2)z}. \tag{7.5}$$

The term $\Delta k = 2k_1 - k_2$ is the so-called momentum mismatch.

7.1.1 Phase-Matching

The Phase-Matching (PM) condition plays a crucial role in establishing the availability of a nonlinear process. To understand PM, we simplify the discussion introducing the undepleted-pump approximation, i.e. A_1 constant; this is particularity true for low-conversion efficiency as in our experiments. In this approximation, we see from Eq. (7.4) that, for $\Delta k = 0$ (perfect phase-matching), the amplitude A_2 can grow linearly (Fig. 7.1 red line) with z and consequently the SHG intensity can grow quadratically. On the other hand, when the PM condition is not fully achieved, the SHG field oscillates along the propagation and the efficiency remains low, as reported in Fig. 7.1 black line.

[1] The SVEA means

$$\left| \frac{d^2 A_2}{dz^2} \right| \ll \left| k_2 \frac{dA_2}{dz} \right|.$$

This condition requires that the fractional change in A_3 in a distance of the order of an optical wavelength must be much smaller than unity [219].

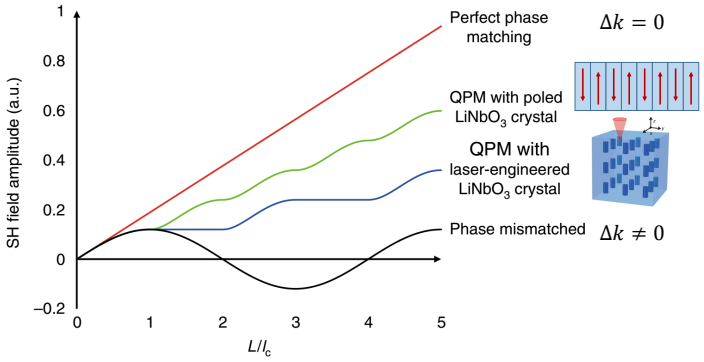

Figure 7.1. Amplitude of the SHG for different PM mechanisms as function of the length of the crystal L normalized to the coherence length of the nonlinear interaction l_c. (Adapted from Ref. [220])

The PM condition for SHG explicitly means that:

$$\frac{n_2\omega_2}{c} = \frac{2n_1\omega_1}{c} \Rightarrow n(2\omega)2\omega = 2n(\omega)\omega \Rightarrow n(2\omega) = n(\omega). \tag{7.6}$$

No material can directly satisfy condition (7.6) because of the frequency dispersion of the refractive index [221]. The usually adopted solution is to exploit the intrinsic birefringence of media, that is the dependence of the refractive index on the polarization direction. The crystal has, then, two refractive indexes, the ordinary and the extraordinary, with two different dispersion relations and it could happen that, for certain values of frequencies, the Eq. (7.6) is satisfied. There are two possibilities:

- Type 1 PM: the two waves of the pump have the same polarization and the SHG is orthogonally polarized;
- Type 2 PM: the two waves of the pump are orthogonally polarized and the SHG is ordinary (extraordinary) if the medium is a positive (negative) uniaxial crystal.

We point out that not all crystals display birefringence, in particular centrosymmetric media are optically isotropic and then do not manifest birefringence. Furthermore, it may possible that the noncentrosymmetric medium does not possess enough birefringence to compensate the refractive index dispersion for the desired wavelengths. All these circumstances reduces the availability of phase-matchable materials and other solutions are necessary.

7.2 Phase Matching In Periodic Structures

We have seen that an efficient SHG requires the noncentrosymmetric medium to fulfil the PM constraints. In nature, only few material are directly available so that other techniques

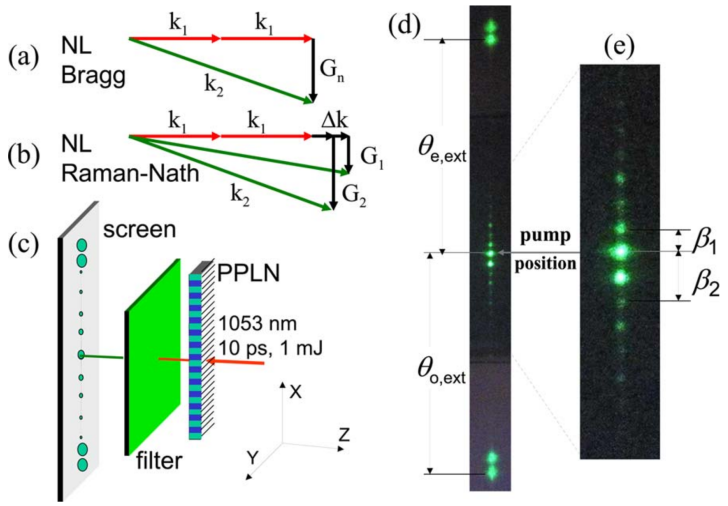

Figure 7.2. Example of the SHG in a periodic medium. (a) Scheme of the nonlinear Bragg diffraction. (b) Scheme of the Raman-Nath diffraction. (c) Sketch of the SHG setup. (d)-(e) Actual experimental observations. (From Ref. [222])

are adopted to overcome PM limitations. One of these is the so-called Quasi Phase Matching (QPM) that is achieved by a structural periodicity built into the nonlinear medium that corrects the phase mismatch [223]. As illustrated in the inset of Fig. 7.1, the QPM material is periodically poled so that the orientation of the crystalline axis flips every coherence length $l_c = \lambda(\omega)/4[n(2\omega) - n(\omega)]$ [224]. The inversion of the crystalline axis is associated with the change of the sign of the nonlinear coupling coefficient d_{eff} that can compensate the nonzero wavevector mismatch [219]. It happens that the SHG is crescent in the length l_c and after that, instead of decreasing as normal PM establishes (black line of Fig. 7.1), it grows again due to inverted d_{eff} as shown by the blue and green curves of Fig. 7.1 [220].

The concept of QPM can be extended in 2 and 3 dimensions in the so-called nonlinear photonic lattices. We consider now the simplest case with constant linear susceptibility ($\varepsilon_r^{(1)}$ =const) in the whole material so that the periodic pattern is attributed only to $d_{\text{eff}}(\vec{r})$, i.e.

$$d_{\text{eff}}(\vec{r}) = \sum_{\vec{G}} \kappa_{\vec{G}} \exp(-i\vec{G} \cdot \vec{r}), \tag{7.7}$$

where $\vec{G} = (\pi/\Lambda)\vec{n}$ is one of the vectors of the reciprocal lattice along the $\vec{n}$ direction and $\kappa_{\vec{G}}$ are coefficients. Inserting Eq. (7.7) in Eq. (7.4), we obtain the PM expression for nonlinear photonic lattices [224]

$$\Delta\vec{k} = 2\vec{k}_1 - \vec{k}_2 + \vec{G}. \tag{7.8}$$

We note that the found expression is a relation between vectors and not simply between

scalar quantities as for the one dimensional case. This means that the PM constraints has to be satisfied both in the longitudinal and transverse directions. In particular the transverse PM condition states that $\sin\alpha_m = m|\vec{G}|/k_2$. The resulting SHG has a discrete emission that can lead to the so-called nonlinear Bragg diffraction [224, 225] that is illustrated in Fig. 7.2(a). Moreover, another SHG discrete mechanism belongs to nonlinear photonic lattices: the so-called Raman-Nath nonlinear diffraction. Here, the PM is fulfilled thanks to a phonon which provides the reciprocal lattice vector $\delta\vec{k}_{ph}$ and the associated PM relation becomes $\Delta\vec{k} = 2\vec{k}_1 - \vec{k}_2 + \vec{G} + \delta\vec{k}_{ph}$ [222, 226] as sketched in the scheme of Fig. 7.2(b).

An experimental example of the combined effect of the nonlinear Bragg and the nonlinear Raman-Nath on SHG, is provided in Figs. 7.2(d),(e). In detail, the small spots near the pump position are associated to the nonlinear Raman-Nath instead the farther spots refer to the nonlinear Bragg. The one dimensional emission along the x-axis is coherent with the experimental setup of Fig. 7.2(c).

7.3 Random Phase Matching

By its own nature, QPM suffers important limitations: the SHG is allowed only for the frequency to which the material is designed. Furthermore, there is a high angular and temperature sensibility so that also a small variation can cause an appreciable reduction in the conversion efficiency due to the slight change in the actual period. Most of QPM restrictions can be overcome by Random Phase Matching (RPM) [190, 227]. This method exploits the disorder inside some materials to fulfil the PM conditions. The principle is the same of QPM but it is available for an infinite number of wavevectors due to the random photonic nonlinear structure of the material.

In the bottom panels of Fig. 7.3 there are illustrated two possible random microscopic crystal configurations: the two fractal patterns are made by domains of different size. The mechanism of QPM can be understood looking at the Fourier spectra in the top panels of Fig. 7.3. We see that for each configuration is associated a continuous of reciprocal vectors $\vec{G}$ that corresponds to the various periodicities Λ embedded in the fractal structure. In analogy with nonlinear photonic crystals, such vectors $\vec{G}$ can be exploited to fulfil the PM condition of Eq. 7.8 [190]. In Fig. 7.3(a) it is shown a possible situation where the SHG is expected to be emitted in the angular direction α. This is the so-called Čerenkov-type PM[2] and in isotropic media it manifest in a continous conical emission with $\alpha = \arccos(n_\omega/n_{2\omega})$ [222, 229–231].

[2] Some authors refer to the nonlinear Bragg diffraction as nonlinear Čerenkov emission [228].

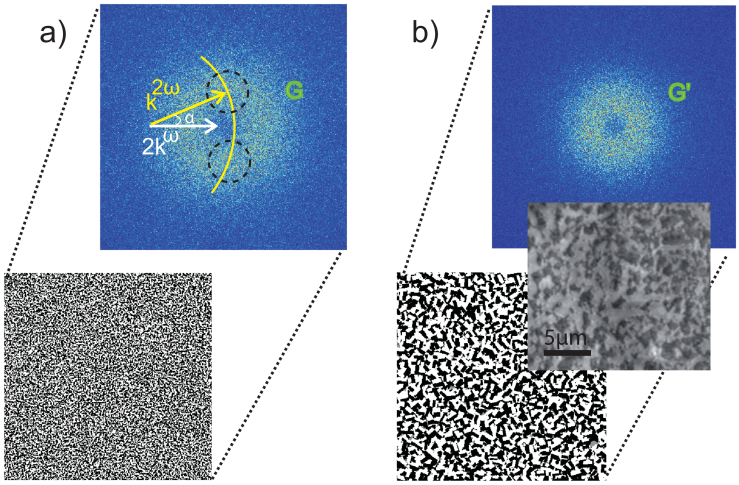

Figure 7.3. Illustration of QPM in ferroelectric perovskite. Bottom panels: simulation of random domains distributions with (a) smaller and (b) bigger grain size. The black and white colors indicate opposite signs of the d_{eff}. Top panels: Fuorier spectra of the corresponding fractal pattern of the bottom panels. Brighter the color, higher the Fourier component. (From Ref. [191])

7.4 Preliminary Results

Many Perovskites, in the orthorhombic (non-centrosymmetric) ferroelectric phase, have been demonstrated to be eligible to achieve RPM due to the random distribution of the ferroelectric domains [191, 227]. In the same materials, furthermore great efforts are made to study and obtain nonlinear photonic lattices.

In particular two recent works, Ref. [220] and Ref. [232], concerning three-dimensional photonic crystals renew the interest on the structured SHG. They, independently and at the same time, demonstrate that ferroelectric perovskites can be turned into fully 3D nonlinear photonic crystals. They both reach their results with material engineer, laser writing a periodic structure with few layers along the propagation axis.

In our work we have studied the SHG in a lithium-potassium-tantalate-niobate (KLTN). The measurements are performed in both unpoled and field cooled sample. The field cooling process is achieved first heating the sample and than cooling it applying a strong electric field [191]. We note that this method provides an uniform directional strain that does not modify locally, i.e. periodically, the domains sizes and orientations.

Specifically, here, we report the preliminary results obtained exploiting the KLTN crystal at $T = T_C - 25$ K. All measurements are performed with a $\lambda = 820 \pm 10$ nm pump with average power of $\simeq 500$ mW and pulse duration of $\simeq 70$ fs. The observations for poled sample are reported in Figs. 7.4(a)-(b), 7.5(a), 7.6(a). They indicate the existence of a periodic features in the SHG that reveal a grating-like spatial distribution of the nonlinear coefficient according to the QPM theory. We point out that the linear cross-polarizer

imaging of the crystal input-facet [Figs. 7.4(c), 7.5(b), 7.6(b)] shows periodic features that are incompatible with the observed SHG as verified by Fourier analysis (not reported). This is particularly true for the SHG that rise from the speckle image of Fig. 7.6(b) that we believe is caused by the random organization of dipoles along the field-application direction. To understand the effect of poling we report the SHG obtained from the unpoled KLTN in Figs. 7.4(d), 7.5(c), 7.6(c) . The observed SHG cannot be connected to any periodic structure. On the other hand these kind of patterns are very similar to those reported for RPM in ferroelectric crystal [190, 191]. In particular, in the Fig. 7.5(c) configuration we measure a conversion efficiency of 0.5% that is comparable with the highest observed for RPM SHG [227].

The experiments are not definitive but they are enough to illustrate the possibilities of SHG in nano-disorder ferroelectric crystals. The periodic feature observed for the poled crystal pushes us to connect this structured SHG with the linear super-crystal since the samples have essentially the same structure. From an applicative point of view these studies represents an important advantage in search of new and more feasible sources. We observed, indeed, a wide angular and spectral acceptance that is it seems that the structured SHG is not susceptible to variation of $\pm 45°$ and ± 30 nm of the pump. From theoretical point of view, these studies demonstrate that the SHG can be used as an important tool to disclose the microscopic structure of the nano-disorder ferroelectric perovskites.

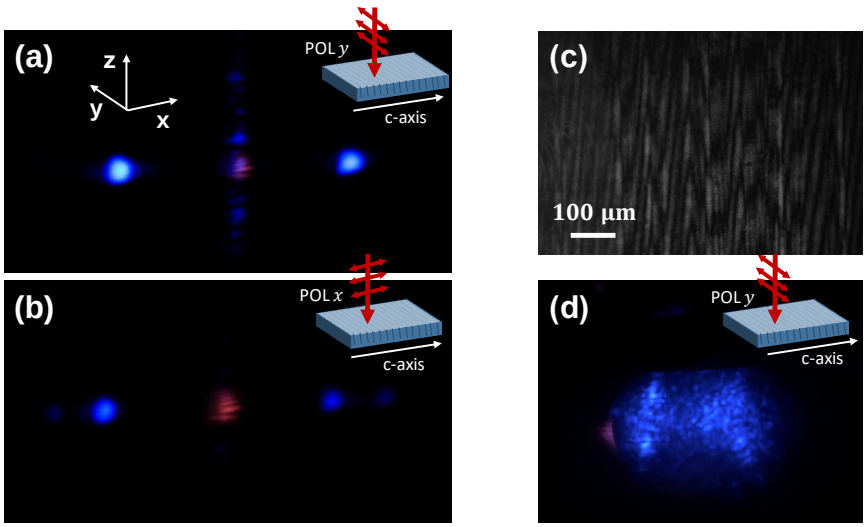

Figure 7.4. Experimental observation of $\lambda = 410$ SHG in the KLTN crystal. In the poled sample the $\lambda = 820$ nm pump propagates along the z-direction and it is (a) y-polarized or (b) x-polarized. (c) Corresponding cross-polarizer linear propagation. (d) SHG from the unpoled KLTN obtained by the x-polarized pump, the case with y-polarized pump is not reported because it manifest the same feature with lower visibility.

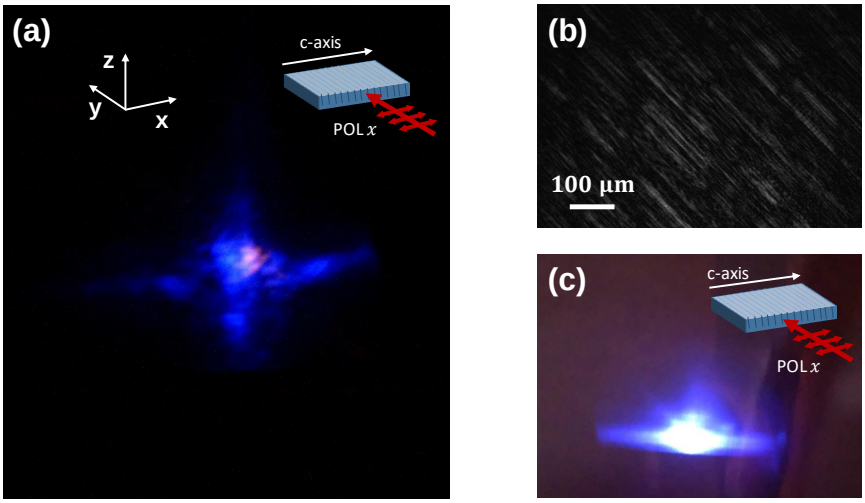

Figure 7.5. Experimental observation of $\lambda = 410$ nm SHG in the KLTN crystal. The $\lambda = 820$ nm pump propagates along the y-direction and it is x-polarized. Reported Fourier space images for (a) poled and (b) unpoled sample. The pump polarization is chose only to maximize the conversion efficiency and same SHG distribution, but lower, is observed also with z-polarized pump. (b) Linear cross-polarizer imaging for poled crystal.

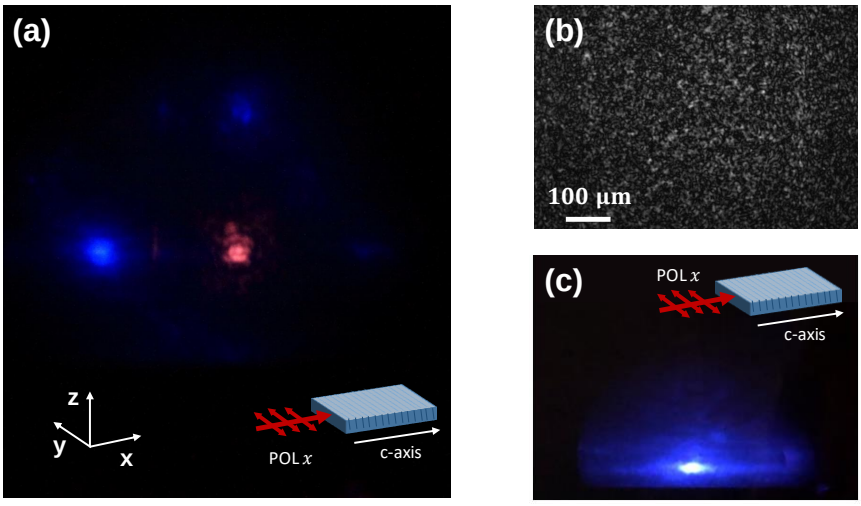

Figure 7.6. Experimental observation of $\lambda = 410$ nm SHG in the KLTN crystal. The $\lambda = 820$ nm pump propagates along the x-direction and it is y-polarized. Reported Fourier space images for (a) poled and (b) unpoled sample. The pump polarization is chose only to maximize the conversion efficiency and same SHG distribution, but lower, is observed also with z-polarized pump. (b) Linear cross-polarizer imaging for poled crystal.

Chapter 8

Giant broadband refraction in the visible in a ferroelectric perovskite

In this Chapter we report our observation of Giant index of Refraction (GR). In principle, materials with a broadband giant index of refraction ($n > 10$) overcome chromatic aberration and shrink the diffraction limit down to the nanoscale, allowing new opportunites for nanoscopic imaging [233]. They also open new avenues for the management of light to improve the performance of photovoltaic cells [234]. Here we report a ferroelectric perovskite with an index of refraction $n > 26$ across the entire visible spectrum and demonstrate its behaviour using white-light and laser refraction and diffraction experiments. The sample has a natural-occurring room temperature phase that propagates visible light along its normal axis without significant diffraction or chromatic dispersion, irrespective of beam size, intensity, and angle of incidence.

8.1 Fresnel Refraction Theory

In conditions of validity of the macroscopic Maxwell Equations, the optical electric field $\mathbf{E}$ obeys $\nabla^2\mathbf{E} - (n/c)^2\partial_{tt}\mathbf{E} = 0$, where n is the wavelength-dependent index of refraction of the material and c the speed of light. Light entering a material with index of refraction n suffers refraction according to Snell's law, i.e., $\sin\theta_1 = n\sin\theta_2$, where θ_1 and θ_2 are the angles formed by the beam with the normal to the boundary of the material. Once inside the material, diffraction causes the beam to have an angular spread $\Delta\theta \propto \lambda/nw_0$, where λ is the wavelength and w_0 is the input size of the beam, and this limits the spatial resolution of transmitted waveforms. Since n is wavelength-dependent, both refraction and diffraction are chromatic, i.e., different wavelengths follow different paths (chromatic aberration) and have a different angular spread. A giant refraction (GR) with $n \gg 1$ across the visible spectrum implies that refracted beams propagate along the normal to the material boundary, with a vanishing $\theta_2 = \sin^{-1}\left((1/n)\sin\theta_1\right)$, and a vanishing chromatic aberration $d\theta_2/d\lambda \simeq$

$-\sin\theta_1(1/n)^2(dn/d\lambda)$. Furthermore, since each spectral component of wavelength λ obeys a different Helmholtz Equation $\nabla^2\mathbf{E}_\lambda + (k_0 n(\lambda))^2\mathbf{E}_\lambda = 0$ [235], where $k_0 = 2\pi/\lambda = \omega/c$ and ω is the corresponding angular frequency, each plane-wave component of wave-vector $\mathbf{k}$ obeys $k_x^2 + k_y^2 + k_z^2 = k_0^2 n^2$. Angled components with $k_x, k_y \neq 0$, fixed by their values outside the material, manifest a different phase-velocity along the propagation axis $k_z = \sqrt{k_0^2 n^2 - k_x^2 - k_y^2}$. The dephasing of these components, i.e., diffraction, is thus associated with the value of $\partial k_z/\partial k_x = -k_x/\sqrt{k_0^2 n^2 - k_x^2 - k_y^2} \sim (1/n)$ that vanishes, along with $\partial k_z/\partial k_y$, as $n \gg 1$. Analogously, also the angular spread vanishes for $n \gg 1$, $\Delta\theta = |k_\perp|_{max}/k_z \sim 1/w_0 k_0 n$, where $|k_\perp|_{max} = |\sqrt{k_x^2 + k_y^2}|_{max} \sim 1/w_0$ is the size of the transverse angular spectrum at the boundary. In other words, for all wavelengths, $\theta_2 \simeq 0$ for all launch θ_1, (no chromatic aberration) and we have a vanishing angular spread $\Delta\theta \simeq 0$ for all beam sizes w_0 (no diffraction). In terms of imaging, GR causes the material to project the input optical field directly to the output of the sample as if the space occupied by the material itself were absent. While GR is generally inaccessible in an isotropic material because an $n \gg 1$ implies that the Fresnel reflection coefficient at the input (and output) boundary is $R \simeq 1$ [236], i.e., no light ever enters or leaves the material, it becomes accessible in an anisotropic material. Strong anisotropy together with a giant dielectric response is found in critical disordered ferroelectric perovskites [173, 183, 202].

8.1.1 Giant Refraction and Anisotropy

Giant Refraction implies refraction along the normal to the boundary of the medium, no chromatic aberration, and no diffraction. In turn, the boundary conditions for an isotropic material with GR also imply that very little light can actually enter or leave it, as rendered explicit by the standard Fresnel equations. For example, in the case of normal incidence, the coefficient $R = |(1-n)/(1+n)|^2 \to 1$ as $n \to \infty$. An analogous anomalous reflection also occurs on exiting the material, where now the relative index of refraction is $(1/n) \ll 1$. Fresnel reflection, in turn, does not hamper GR in anisotropic systems [237]. In Fig. 8.1 we report (1+1)D FDTD numerical results for reflection and refraction for the TM and TE modes, where $\mathbf{u}_t$ is the unit vector parallel to the boundary in the incidence plane, $\mathbf{u}_n$ is the unit vector normal to the boundary, and $\mathbf{u}_p$ is the one normal to the incidence plane. In Fig. 8.1(a) standard refraction and reflection can be found for a homogeneous $n = 2$ TM case, while, as reported in Fig. 8.1(b), for $n = 5$, both refraction and reflection are stronger. In Figs. 8.1(c),(d) we report the cases with $n_{tt} = 2, n_{nn} = 5, n_{pp} = 2$ and $n_{tt} = 2, n_{nn} = 2, n_{pp} = 5$, respectively. The picture is radically modified in Fig. 8.1(c) where the diagonal index matrix has $n_{tt} = 2, n_{nn} = 5, n_{pp} = 2$: enhanced refraction is found without the enhanced reflection. The TE case is reported in Fig. 8.1(e)-(h), where enhanced refraction is observed in the case of $n_{tt} = 2, n_{nn} = 2, n_{pp} = 5$ [Fig. 8.1(h)] and, as for the homogeneous case of Fig. 8.1(f), also enhanced reflection is found.

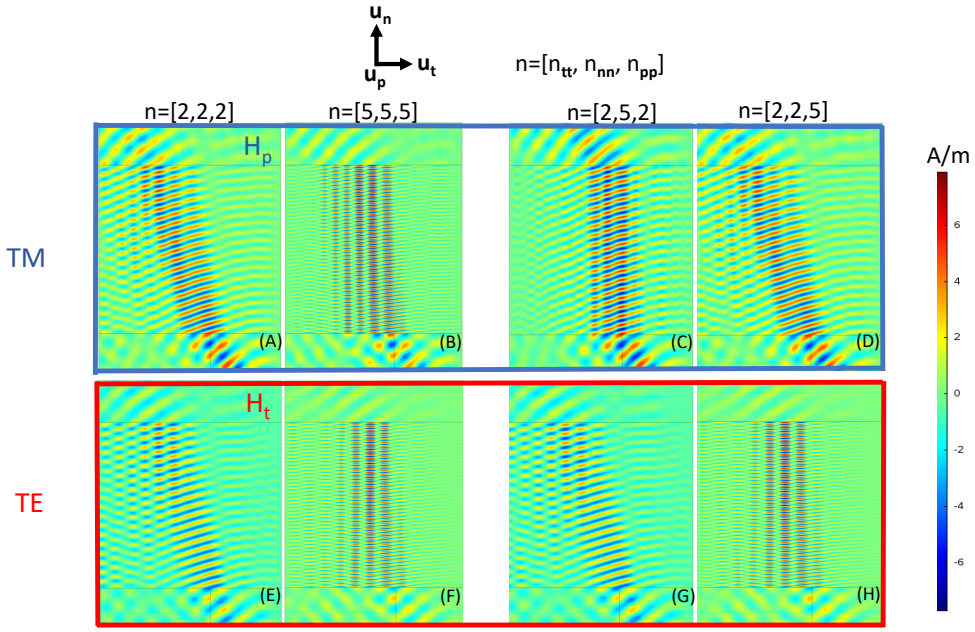

Figure 8.1. Numerical analysis (using an FTDT algorithm) of refraction and reflection in various conditions (see text). The wave has λ=632.8 nm, an input width of 1.75 μm, θ_1=45°, and is allowed to propagate in the refracting material that is 6 μm in length along $\mathbf{u}_n$.

In the TM case refraction is associated to the matching of the wave-vector across the boundary along $\mathbf{u}_t$, and this involves the component of the optical electric field that oscillates along $\mathbf{u}_n$ so that, in order to have GR, $n_{nn} \gg 1$ is required. In turn, the Fresnel equations involve the susceptibility along $\mathbf{u}_t$, so that a standard n_{tt} leads to standard reflection. In the TE case, GR involves the optical component of the electric field that oscillates along $\mathbf{u}_p$, so that $n_{pp} \gg 1$ is needed. Since, however, in this case the Fresnel equation involves n_{pp}, GR is accompanied by strong reflection.

8.2 Experimental Setup

The key ingredient of out experiment is our nano-disorder ferroelectric perovskite which we report a picture in Fig. 8.2(a). The sample we have grown is a zero-cut polished lithium-enriched solid-solution of potassium-tantalate-niobate (KTN:Li) with an average composition $K_{0.997}Ta_{0.64}Nb_{0.36}O_3$:$Li_{0.003}$. It measures in the three directions $6.0^{(x)}$ x $2.6^{(y)}$ x $3.0^{(z)}$ mm and has a pale green hue (with an absorption of 2 cm^{-1} in the visible) caused by a small component of Cu impurities. The unit cell manifests random substitutions, a compositional-disorder that, on consequence of the structural flexibility typical of perovskites, leads to locally modified polarizabilities and temperature-dependent nanoscale dipolar structures (nanodisordered ferroelectricity). The result is a modified ferroelectric

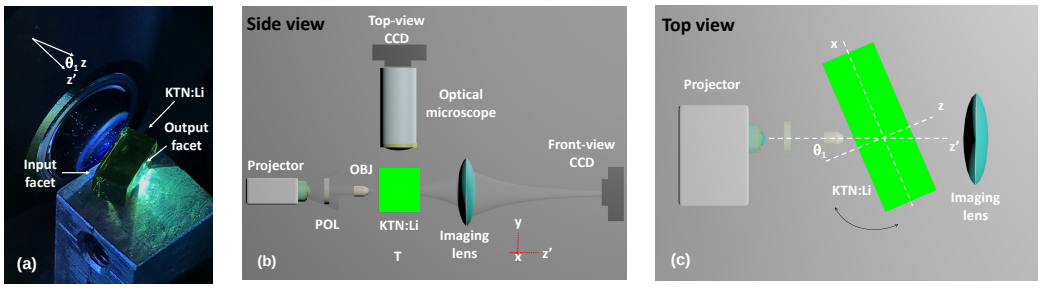

Figure 8.2. Sample and apparatus sketch. (a) Image of the KLTN crystal during GR experiment. Strongly diffracting white-light from a projector is focused onto the sample, propagates through it, and appears to exit as if it had been focused directly onto the output facet, 3mm away. The sample projects the input light beam to the output as if not only the sample is absent, but also the space occupied by it. (b) Side-view and (c) top-view of the experimental setup.

behavior dominated by so-called polar-nanoregions (PNRs), characterized by dielectric dispersion and out-of-equilibrium behavior (relaxor ferroelectricity) [185, 238]. In our present case, this disorder is itself not homogeneous, manifesting a spatially-periodic micrometric oscillation along a specific crystal axis. This is because the sample is grown into a bulk through the top-seeded method, a technique that entails a slight time oscillation in the temperature of the solidifying melt that, in turn, translates into a characteristic periodic pattern along the growth (or pull) axis. This pattern conditions the nanoscale dipolar structures that, at the room-temperature Curie point (T_C=288 K), form a three-dimensional mesh of spontaneous polarization, the super-crystal [101, 180]. We note that samples of KTN:Li can be grown as films and thin films using vapor deposition or be tailored into waveguides using ion amorphization. While a lower-dimensional super-crystal can potentially emerge in a film, at present no GR experiments have been performed in a film of thin-film sample.

The experimental setup is sketched in Figs. 8.2(b)-(c). The source is a commercial projector (NEC-VE281X, XGA, 2800 lumens). Light exiting a bright screen image is sent through a linear polarization filter (POL) that allows the passage of light polarized along the x axis (TM mode) or along the y axis (TE mode). Light is collected using a high-aperture long-working distance microscope objective (OBJ, Edmund Optics - 100X - 3mm working distance -achromatic - NA =0.8) positioned approximately 30 cm from the output lens of the projector. An important parameter in experiments is the rotation angle of the KTN:Li sample around the vertical y axis, θ_1 (see Fig. 1c), i.e., the angle between the normal to the sample input facet (z) and the experiment propagation axis (z'). Images and movies are obtained using an Apple iPhone7 either directly or through one eyepiece of a high-aperture optical microscope (Nikon, NA=0.8) positioned on top of the sample, along the y axis. Higher resolution images are attained placing in the eyepiece a high-resolution black-and-white charged-coupled-device CCD (PCO Pixelfly, 14 bit, 1392$\times$1060 pixels). Transmitted light

is collected by an imaging lens with numerical aperture 0.35 and focal length 75 mm. This lens forms an image of a desired plane onto the front-view CCD (Thorlabs BC-106VIS, 12 bit). Sample temperature is fixed by a current-controlled Peltier junction and is positioned and rotated using micrometric stages.

8.3 White Light Propagation

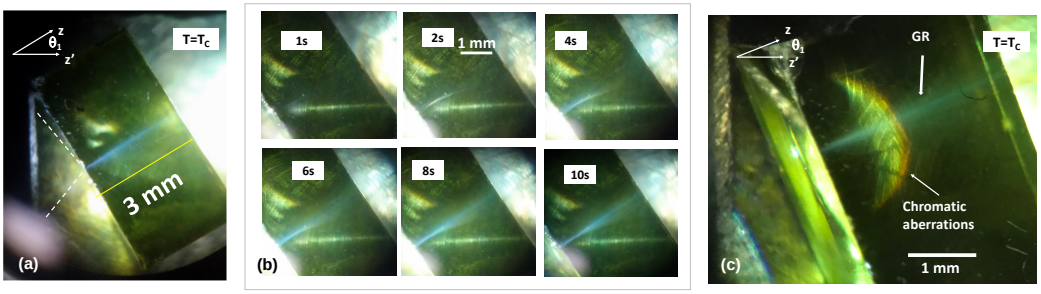

Figure 8.3. Low resolution color images of the GR inside the KLTN sample. (a) Top view of the behavior of light inside the sample and (b) the manifestation of GR as the sample thermalizes at the Curie point. (c) Achromatic nature of GR compared to colored scattering.

The basic GR phenomenon is reported in Fig. 8.2(a), where stray light indicates that while light is focused onto the input facet, it appears to emerge directly from the output facet, 3mm away from the input. In Fig. 8.3(a) the top view image shows light undergoing GR: the beam is transmitted orthogonal to the sample facets, irrespective of the actual tilt angle. In fact, for $T = T_C$, a distinct white beam forms that extends from the input of the sample to the output. This beam propagates with $\theta_2 = 0$, is white, and does not spread, even though it originates from a white incoherent focused spot from the microscope objective. We underline that, normally, the white beam diffracts so as to engulf the entire sample and some chromatic aberrations are seen.

The GR beam forms on consequence of thermalizing the crystal to T_C, as can be appreciated in Fig. 8.3(b), where the sample originally at 303 K is brought to $T = T_C$ and progressively thermalizes in time. Intervals of time measure the delay between the moment in which the image is captured and that for which the sensor measuring the temperature of the sample first reaches T_C. The phenomenon depends solely on T and is independent of beam intensity, size, launch angle θ_1, and position in the sample. As expected, GR also occurs when the white-light is focused before and after the input facet, but with a correspondingly larger width in the GR component. Specifically, in Fig. 8.3(b), the focus is formed inside the sample and, as the GR regime emerges, the actual focus disappears and leads to a slightly enlarged GR transmission. The GR beam does not manifest the chromatic dispersion that can, in turn, be directly observed in conventional scattering from the crystal

support, as reported in Fig. 8.3(c).

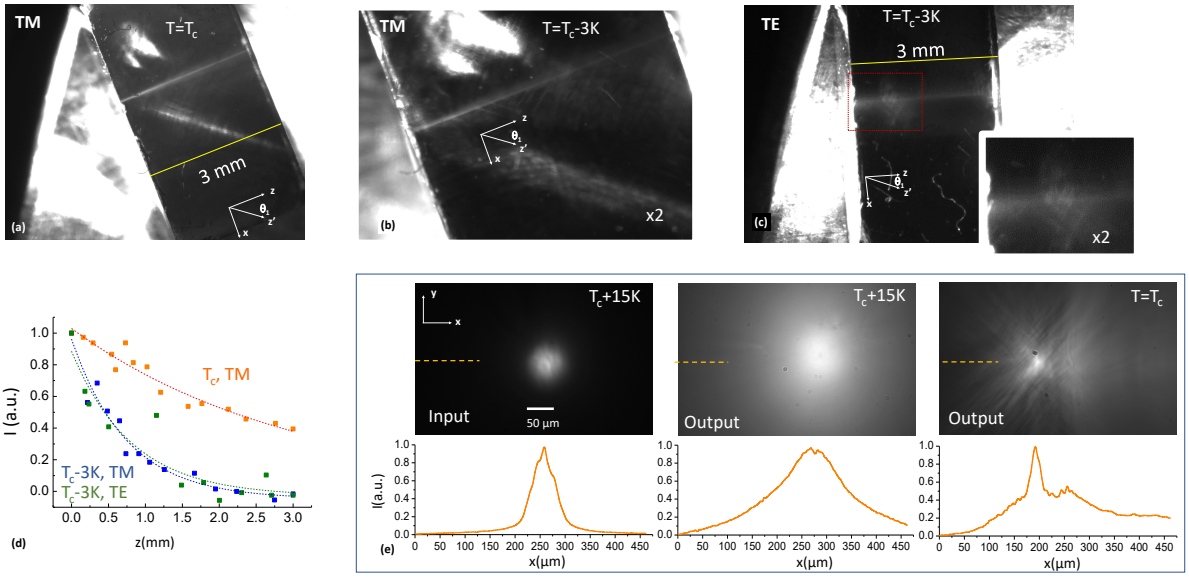

Figure 8.4. (a) High resolution top-view of the beam suffering GR at $T = T_C$ and (b) at $T < T_C$, an increased scattering is evident. (c) GR for the TE mode ($T < T_C$). (d) Intensity of scattered light along propagation for different polarization states and temperatures. (e) Input and output transverse intensity distribution when the sample manifests standard refraction ($T > T_C$) and GR ($T = T_C$). The broad background at $T = T_C$ is the original diffracting Snell component that is, in the present case, angularly superimposed with the GR beam.

Higher-resolution images of the effect are reported in Figs. 8.4(a)-(c). Figure 8.4(a) reports the GR effect as the sample is kept at the ferroelectric Curie point, while Fig. 8.4(b) reports the phenomenon when the sample is kept at a lower temperature (T_C-3 K). Compared to the GR case, increased scattering causes light to decay along the normal to the input facet. Enhanced scattering appears in the path of the beam. At this same temperature, also light polarized in the orthogonal TE mode suffers GR, along with a similar scattering [Fig. 8.4(c)]. The intensity of scattered light, as deduced from scattered intensity, is reported in Fig. 8.4(d) (where background noise has been subtracted). Orange squares refer to data from the $T = T_C$ GR and indicate an exponential decay with a decay rate of 3.8 cm^{-1} while blue and green curves refer, respectively, to the TM and TE modes at $T = T_C$ -3K, with a decay rate of 11.2 cm^{-1}. Front images of the projector light are reported in Fig. 8.4(e) at the input and output at $T = T_C + 15K$ and $T = T_C$. Light is focused to a 52 μm spot, and the sample is rotated by an angle of $\theta_1 = 35°$. When GR emerges, the output Full-Width-at-Half-Maximum (FWHM) is 35 μm, while without GR the FWHM is larger than 142 μm, as the output diffraction image is a convolution of the actual spread out beam with the limited optical transfer function of the output imaging lens.

Because no refraction and diffraction are observed at T_C (Fig. 8.4), the estimated value of n across the visible spectrum descends from the experimental uncertainty. In terms of the angle of refraction, spatial resolution is limited by the width of the beam ($\sim$ 50 μm) and the length of the sample (L_z = 3 mm), so that the minimum observable θ_2 is $\delta\theta_2 = 50/3000 = 0.017$. Consequently, the minimum observable index of refraction is $\delta n = \sin\theta_1/\sin\delta\theta_2 = 34$ ($\theta_1 = 35°$), hence $n > 34$ for the spectrum of the projector lamp.

8.4 Laser Light Propagation

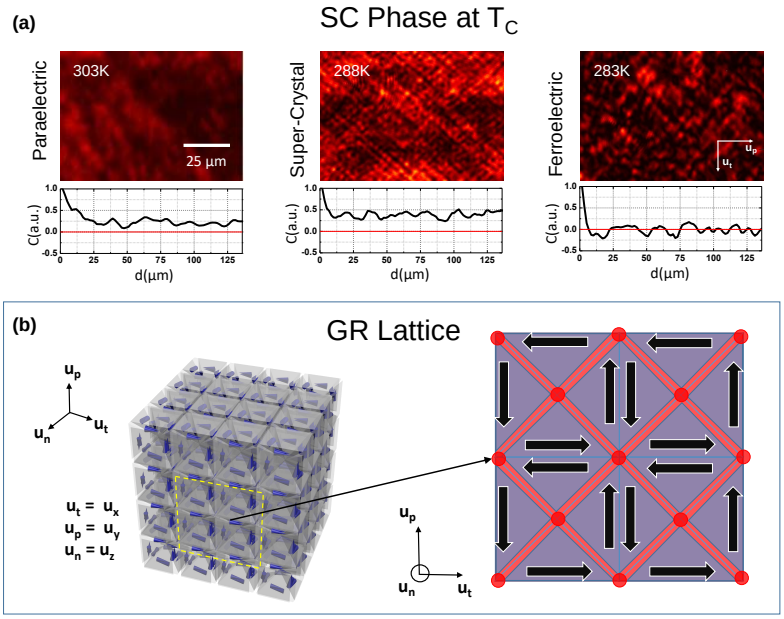

Figure 8.5. Physical origin of GR. (a) Optical characterization of the ferroelectric SC (the correlation coefficient $C(d)$ is calculated between a portion of the intensity distribution transmitted by the sample 35×35 μm^2 and a portion shifted by d along the $\mathbf{u}_p$ axis). (b) Spontaneous polarization mesh in the perovskite tetragonal SC phase with a blow-up of the regions (red) supporting TM GR.

To further investigate the GR effect we have performed experiments with laser light substituting the projector with a 5 mW He-Ne laser operating at λ=632.8 nm and linearly polarized along $\mathbf{u}_t$. The monochromatic light transmission is reported in Fig. 8.5(a) for $T > T_C$ (303 K), $T = T_C$ (288 K), and $T < T_C$ (283 K). At T_C the emergence of a coherent spatial structure, typical of the ferroelectric SC [101, 180], leads to a finite correlation in the intensity distribution, absent in the paraelectric transmission and in the subcooled ferroelectric state, where relevant domain disorder is observed. Optical

diffraction experiments indicate that the SC is compatible with the three-dimensional mesh of spontaneous polarization (blue arrows) illustrated in Fig. 8.5(b) (left). Here the anisotropy required for GR, as explained in Sec. 8.1, occurs on a subset of regions in the sample that forms a characteristic lattice illustrated in Fig. 8.5(b) (right, red). In detail, the blue-shaded regions contain spontaneous polarization prevalently along $\mathbf{u}_t$ and $\mathbf{u}_p$, while the red-shaded regions also contain spontaneous polarization along $\mathbf{u}_n$. In conditions in which the optical susceptibility is enhanced along the direction of spontaneous polarization, these regions have the principal components of the index of refraction tensor that allow TM GR, i.e., $n_{nn} \gg n_{tt}, n_{pp}$ along $\mathbf{u}_n$, $\mathbf{u}_t$, and $\mathbf{u}_p$, respectively. The GR for the TE mode, in turn, is supported by the regions with a prevalently $\mathbf{u}_p$ directed spontaneous polarization (not illustrated). Only the component of the input beam that impinges on the regions that allow the correct anisotropy can actually manifest GR, while the remaining component of light suffers standard Snell refraction.

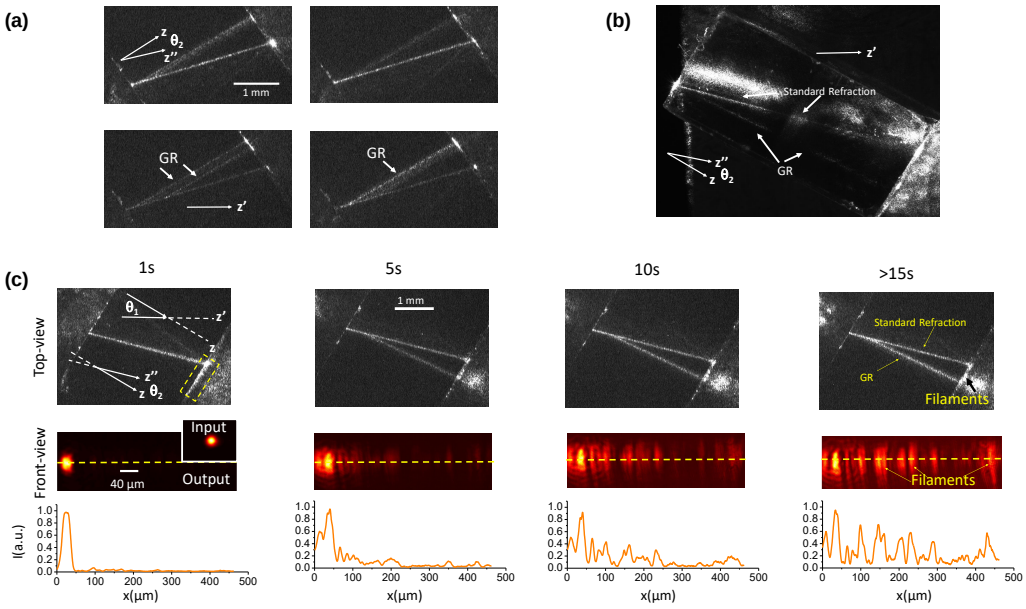

Figure 8.6. GR for low aperture laser light. (a) Low aperture laser light showing the decay of the standard refraction component into multiple GR beams at $T = T_C$ along with the standard refraction component (see text). (d) The top-view snapshot reports GR along the long 6 mm side of the sample. (e) Detailed analysis of laser light propagation seen from a top-view (top) front view (central) and as a profile along the dashed line (bottom) as the sample relaxes to $T = T_C$. Time intervals are measured starting from when the temperature gauge reaches T_C.

The presence of the two components is confirmed using low-aperture laser light, as reported in Figs. 8.6. For this kind of experiments, the beam is first expanded using two confocal lenses to a plane-parallel 10 mm radius beam. The beam is then focused using a 150 mm focal length lens onto the input facet of the sample. The beam numerical aperture

is NA=0.1 (in air). The input beam has a FWHM of 18 μm and is TM polarized. Top view images are captured in a fashion similar to that used for white-light [scattered light leads to an estimated monochromatic 632.8 nm decay rate along propagation at T_C of 4.6 cm^{-1} for the steady-state of Fig. 8.6(c)]. Thanks to this procedure, we are able to study the component of the light beam that undergoes standard refraction and diffraction, not observable in the white-light experiments of Figs. 8.3 and 8.4. Moreover, as expected from the wholly three-dimensional nature of the SC, the effect occurs along all three directions of the underlying SC [see Fig. 8.6(b) for GR with $\mathbf{u}_n$ along the 6mm long side of the sample]. Front view images and intensity profiles of transmitted light reported in Fig. 8.5(c) indicate that the GR suffers a filamentation with a characteristic scale of tens of micrometers, compatible with the scale of the SC. Close inspection reveals that this filamentation is also marginally visible in the top-view images of the output facet, but at lower resolution, as caused by the coherent speckle dominated laser scattering (indicated as "Filaments" in the top-view image). The image is further distorted by the finite depth of focus of the imaging system, as this only allows a portion of the filaments [dashed yellow box in Fig. 8.5(a)] to be in focus at a time in the strongly tilted geometry.

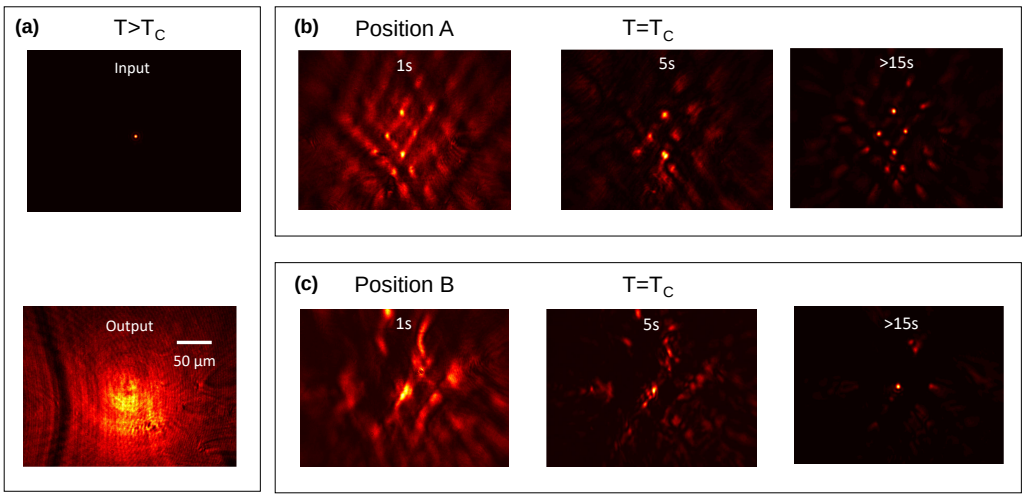

Figure 8.7. GR for high aperture laser light. (f) Input and output beam distribution for $T > T_C$. (g),(h) Output intensity distributions as the crystal settles to T_C for two different launch positions, Position B corresponding to a GR that involves only a micrometric section of the sample that coincides with a single polarization vertex.

In Figs. 8.7 we analyze laser light propagation in conditions of high-aperture: the expanded laser light is strongly focused onto the input facet using the microscope objective (NA=0.8). The experiments are carried out with $\theta_1 = 35^\circ$ and the two reported sequences in Figs. 8.7(b),(c) differ in the actual position of the sample relative to the fixed input launch beam. In high aperture experiments, the component not undergoing GR diffracts to 81 μm,

so that its intensity is too low to be detected when the GR component forms with its highly localized spots [Figs. 8.7(b),(c)]. This means that, as the sample thermalizes at $T = T_C$, only the GR beam is visible. Front-view images reported in Fig. 8.7(b) indicate a spatial structure that reproduces the GR supporting structure (red-shaded regions) illustrated in Fig. 8.5(b) (right). Congruently, the GR pattern is rigidly locked to the sample, it is found to move and rotate following the sample itself. In fact, while the SC [see Fig. 8.5(a)] for $\theta_1 = 0$ is isotropic in the x and y directions, the images of the guided tilted cases for $\theta_1 = 35°$ manifest an anisotropy compatible with a rotation of the SC structure of Fig. 8.7(b) by $\theta_1 \simeq 35°$. The extreme consequence is that the whole GR process can even be confined to a single micrometric section of the sample, corresponding to a single vertex in the red-shaded region of Fig. 8.5(b) (right), if the input launch beam is sufficiently focused down and appropriately aligned, as reported in Fig. 8.7(c) ["Position B" as opposed to the generic input "Position A" in Fig. 8.7(b)]. As expected, not only does the beam propagate along the normal of the input facet irrespective of the launch angle, but the beam itself does not spread on consequence of diffraction.

Experiments in Fig. 8.7 allow an estimate of n (at the laser wavelength) analyzing beam diffraction. Comparing the output intensity FWHM in the steady-state case of Fig. 8.7(c), where only one polarization-vertex is involved and the distortion associated with filamentation is absent, to the input FWHM [Fig. 8.7(a)], we find that the beam spreads from 4.7 μm to 6.8 μm after a $L_z = 3$mm propagation, leading to an estimate of $n > 26$ as explained below. This confirms the huge values of n already encountered in the white-light refraction experiments, huge values that suggest that at T_C local fields play a principal role. We point out that, physically, in a system where the dielectric susceptibility is dominated by weakly-interacting atoms or molecules, an $n \gg 10$ across the visible spectrum appears incompatible with the constraints on atomic/molecular polarizability. In these conditions, GR would require operation in proximity of a resonance, where, however dispersion and absorption make imaging unfeasible. In turn, in the strongly correlated perovskite where susceptibility is dominated by local fields, n can be anomalously enhanced through self-action. In a simplified isotropic approximation, a description is given by the Lorentz-Lorenz relation $n^2 = (1 + (8/3)\pi N\alpha)/(1 - (4/3)\pi N\alpha)$, where N is the density of atoms and α is the atomic polarizability: conditions in which $(4/3)\pi N\alpha \sim 1$, as would occur in proximity of a phase-transition, then allow GR [236, 239].

The giant index value here reported is noticeably lower than giant refraction reported at microwaves[240], as the longer wavelengths involve more components to the susceptibility and lead to a larger linear response. Numerical simulations indicate that rescaling a microwave giant index of refraction to the near-visible spectrum leads to a giant refraction comparable with the one reported here, and what is termed giant will depend on the region of the spectrum investigated [240].

8.4.1 Index of refraction evaluation from diffraction

Experiments in Fig. 8.7(f),(h) report beam propagation in conditions of elevated numerical aperture where non-paraxial corrections become relevant. However, if we self-consistently assume that $n \gg 1$, then the non-paraxial regime ceases to exist, as the effective wavelength λ/n shrinks far below any reasonable transverse size of the beam. Applying the standard diffraction laws of Gaussian beams, we then have that the width of the beam at a given position z along propagation $w(z)$ is related to the input minimum spot size w_0 by the relationship $w(z) = w_0\sqrt{1+(z/z_0)^2}$, where $z_0 = n\pi w_0^2/\lambda$ is the Rayleigh length, so that $n = (L_z\lambda/\pi w_0^2)(w(L_z)^2/w_0^2 - 1)^{-1/2}$. The residual spreading from the 4.7 μm input to 6.8 μm output reported in Fig. 8.7(h) indicates that two 4.7 μm spots displaced by less than 3.4 μm at input will manifest strong overlap and cannot be fully distinguished at output.

8.5 Perspectives

GR suggests a solution to overcome chromatic dispersion in image transmission that sides other recent pioneering solutions, such as those based on metasurfaces [241], while offering new flexibility to presently available micro and nanoscale photonics for applications in optical components, lithography [242], and transformation optics [243]. The very idea that white-light is transferred, irrespective of its launch direction, along the normal to the sample can play a role in developing self-aligning white-light photonics, as would be required to harness, for example, sunlight during a day. The vanishing effective wavelength $(\lambda/n) \to 0$ ($n \gg 1$) implies at once that the laws of achromatic geometrical optics hold and that light energy can be localized to presently inaccessible submicrometric scales. For example, a microscope housed inside a medium manifesting GR will be able to detect features down to a vanishing Abbe limit $d = \lambda/(2\text{NA})$, as the numerical aperture NA $\propto n$ diverges [236]. Furthermore, ultra-tight transverse localization of light, that scales with $(\lambda/n)^2$, can potentially reduce the active material required in detectors or solar-panels, reducing the costs associated to the use of innovative materials, such as photovoltaic perovskites [182]. In terms of subwavelength quantum photonics, strong localization can also form the ideal setting for photon-by-photon nonlinear optics [244, 245].

Part III

Knife-Edge Super-Resolution

In this last part we use long wavelength, at THz frequencies, to develop a new method to achieve super-resolution through the knife-edge technique. This allows us to directly study the role of evanescent waves in super-resolution imaging, i.e. the filtering out of the evanescent spectrum as the super-resolved image approaches the diffraction-limited one.

Our results are published in Ref. [246]. Our other papers about THz imaging, marginally discussed here, are Ref. [247] and Ref. [248].

Chapter 9

Evanescent-Wave Filtering in Images Using Remote Terahertz Structured Illumination

Imaging with structured illumination allows for the retrieval of subwavelength features of an object by conversion of evanescent waves into propagating waves. In conditions in which the object plane and the structured illumination plane do not coincide, this conversion process is subject to progressive filtering of the components with high spatial frequency when the distance between the two planes increases, until the diffraction-limited lateral resolution is restored when the distance exceeds the extension of evanescent waves. In this work, we study the progressive filtering of evanescent waves by developing a remote super-resolution terahertz imaging system operating at a wavelength $\lambda = 1.00$ mm, based on a free-standing knife-edge and a reflective confocal terahertz microscope. In the images recorded with increasing knife-edge to object-plane distance, we observe the transition from a super-resolution of $\lambda/17 \simeq 60$ μm to a diffraction-limited lateral resolution of $\Delta x \simeq \lambda$ expected for our confocal microscope. The extreme non-paraxial conditions are analyzed in detail exploiting the fact that, in the terahertz frequency range, the knife-edge can be positioned at a variable subwavelength distance from the object plane. Electromagnetic simulations of radiation scattering by the knife edge reproduce the experimental super-resolution achieved.

9.1 Introduction

According to diffraction theory, monochromatic electromagnetic waves reflected from a material surface form a mixture of propagating and evanescent waves [236]. For propagating waves, the equal-phase and equal-amplitude fronts coincide, whereas evanescent waves display an exponential decay of their amplitude along the propagation axis, and so the

equal-phase and equal-amplitude fronts are perpendicular. Moreover, evanescent waves transmit no energy and, in distinction to their formally analogous exponentially decaying fields in dissipative media such as metals, they equally occur in vacuum and involve no energy dissipation whatsoever. The distinction between propagating and evanescent waves defines the notion of diffraction-limited imaging and super-resolution: a detector placed at a macroscopic distance from an irradiating or reflecting surface will only collect non-decaying propagating waves, i.e., waves that transfer low-resolution details of the image that are typically of the order of the optical wavelength, depending on the numerical aperture of the focusing optics at the object plane (diffraction-limited imaging). In turn, subwavelength spatial details that are encoded in the evanescent waves can be either directly detected using a scanning near-field detector [249], or, in a super-resolution scheme, they can be extracted by processing multiple images using specifically designed excitation/emission techniques with sub-wavelength spatial modulation, as occurs in structured illumination imaging [250]. In a standard structured illumination scheme, the plane at which the illumination is modulated coincides with the object plane to be imaged. Structured illumination can be generalized to conditions in which the two planes do not coincide, as would occur when super-resolution is required for buried objects. In these conditions super-resolution imaging implies a counterintuitive transition from high-resolution to progressively lower-resolution images as the distance of the structured illumination plane from the object plane increases, because high spatial frequencies are progressively lost in the conversion of decaying evanescent waves into propagating ones. While a great variety of microscopy schemes and experiments tap into the evanescent fields, this progressive filtering of the spatial spectrum inherent to remote structured illumination has not been previously experimentally investigated.

Using monochromatic terahertz (THz) radiation, we report for what we believe to be the first time the transition from a near-field image, composed of spatial frequencies provided by both propagating and evanescent waves, to a diffraction-limited image, formed only by the spatial spectrum of propagating waves. Using a simple knife-edge scanning scheme, we are able to observe this transition in great detail and quantitatively study the progressive modification of the spectral transfer function as the distance of the knife-edge scanning plane (i.e. the structured illumination plane) from the object plane was increased. The experiment becomes technically possible in the THz range because the near-field region extends up to fractions of a millimeter above the sample surface, allowing for mechanical positioning of the knife-edge with a precision that is far smaller than the wavelength. In the visible range, the near-field extends only a fraction of a micrometer above the sample surface where surface roughness and electrostatic interactions make positioning with subwavelength precision a challenge.

9.2 Fourier Analysis Method

The filtering of high spatial frequency components with increasing distance of the structured illumination plane from the object plane can be mathematically described by considering that an optical field $\mathbf{E}$ of wavelength λ emitted or reflected from a surface obeys the Helmoltz equation $\nabla^2\mathbf{E}+k_0^2\mathbf{E}=0$, with $|k_0|=2\pi/\lambda$. This implies that each plane-wave component of wave-vector $\mathbf{k}=(k_x,k_y,k_z)$ must have $k_x^2+k_y^2+k_z^2=k_0^2$, so if the object plane is taken to coincide with the x,y plane at $z=0$, the irradiated field can be described in terms of spatial Fourier components as $E=\iint_{-\infty}^{\infty}E(k_x,k_y)e^{(ik_xx+ik_yy)}e^{(i\sqrt{k_0^2-k_x^2-k_y^2}z)}dk_xdk_y$, where $E(k_x,k_y)$ is the spatial spectrum. Waves with $k_\perp^2=k_x^2+k_y^2\leq(2\pi/\lambda)^2$ leave the object plane in the form of propagating waves. The spatial frequency components $k_\perp^2>(2\pi/\lambda)^2$, beyond the so-called Ewald sphere, can only be encoded into evanescent waves that exponentially decay in the z direction as $\exp\left(-z/z_{ev}(k_\perp)\right)$, where $z_{ev}(k_\perp)=(k_\perp^2-k_0^2)^{-1/2}$. The consequence is that the field collected by a lens or objective at distances $z\gg\lambda$ contains at most details down to the diffraction limit, and subwavelength features with a spatial scale $\Delta x<\lambda$ are inevitably lost [251].

9.3 Remote Super-Resolution

The key ingredient in our experiment is the knife-edge scan, which amounts to a super-resolution scheme operating with a structured illumination plane at a variable subwavelength distance from the reflecting surface where the illuminating radiation is focused (object plane). The knife-edge scan is a direct embodiment of the basic paradigm of super-resolved imaging: to selectively control the regions of the x,y plane that are allowed to reflect (emit) radiation at one given time, and acquire multiple images that can then be co-analyzed to extract subwavelength spatial components of the distribution of reflectors (emitters) [252–255]. The knife-edge scan achieves super-resolution in its most basic single-wavelength beam-profiling execution [256, 257], in contrast to advanced super-resolution techniques that generally involve radiation delivery and collection at different wavelengths, deconvolution calculations, fluorescence phenomena [258], and/or nonlinear interactions with other light fields [192]. In the THz range, knife-edge scans have been also implemented to greatly increase the spatial resolution of images of laser-induced broadband source points, where spatio-temporal aberrations can play an important role [259]. More recently, an optically-induced virtual knife-edge technique has also been demonstrated by structured illumination with a visible laser of the THz-emitting (object) plane [260]. Instead, the transition from near-field imaging to diffraction-limited imaging that we want to investigate here is clear-cut for monochromatic radiation.

To simplify the analysis, let us consider as the object plane a sample surface at $z=0$ emitting/reflecting radiation in the direction $z>0$, with subwavelength spatial features that

however vary only along one of the two transverse directions, say x. The field intensity distribution at the emitter position is $I(x, z = 0)$. As z increases, the field intensity distribution $I(x, z > 0)$ progressively loses its high spatial frequency components with $k_x > 2\pi/\lambda$. An image of the object plane is obtained by reflective confocal scanning microscopy, where the pixels in the image are illuminated one at a time and the corresponding reflected power is separately measured per each pixel (details on the experimental setup are given below). Let us now consider a fully opaque blade that scans along the x-axis a given plane at a fixed z (see schematic in Fig. 9.1(a)). The intensity distribution immediately after the blade is $O(x, z, x') = I(x, z)\theta(x - x')$, where $\theta(x - x')$ is the step function that represents an ideally sharp blade with its edge in x', and edge diffraction effects are initially being neglected, but will be considered later on in the paper. At a distance $z > 0$ from the object plane, the spatial frequency spectrum of $O(x, z, x')$ is altered compared to that at the object plane $O(x, z = 0, x')$, and corresponds to the spatial spectrum that can be scattered by the blade in the far-field. Scattering of the evanescent wave intensity by the blade edge into propagating waves newly formed at $z > 0$ allows super-resolved image reconstruction, which is here achieved by subtracting, for each pixel in the image, the total far-field power collected at each blade position x' from that collected at a previous position $x' - dx'$. The intensity distribution reconstructed on the far-field detector is

$$\begin{aligned} I_S(x', z) &= -\frac{d}{dx'} \int_{\mathbb{R}} dx \int_{\mathbb{R}} O(u, z, x')\text{PSF}\,(x - u)\, du \\ &= -\int_{\mathbb{R}} I(u, z) \frac{d}{dx'} \theta(u - x') du = I(x', z), \end{aligned} \tag{9.1}$$

where PSF(x) is the point-spread-function of the light collecting system [261]. Here, our terahertz reflective scanning confocal microscope has a quasi-gaussian PSF of width of 0.9 mm [247]. If the knife-edge scan is carried out on a plane in the near-field of the emitting surface, and within the above mentioned ideal blade approximation, the high spatial frequencies of the spectrum of $I(x, z)$ will be fully transferred to the reconstructed far-field image $I_S(x, z)$, which is therefore no longer limited by diffraction and is a remotely super-resolved image. While Eq. (9.1) captures the key aspects of our scheme, the ultimate achievable resolution has to be separately evaluated through the rigorous numerical predicton of wave scattering from the blade, as discussed below. Furthermore, our analysis is valid under the assumption that radiation emission by the object is temporally and spatially incoherent, a condition that is here guaranteed by the scanning confocal microscopy scheme. [262, 263]

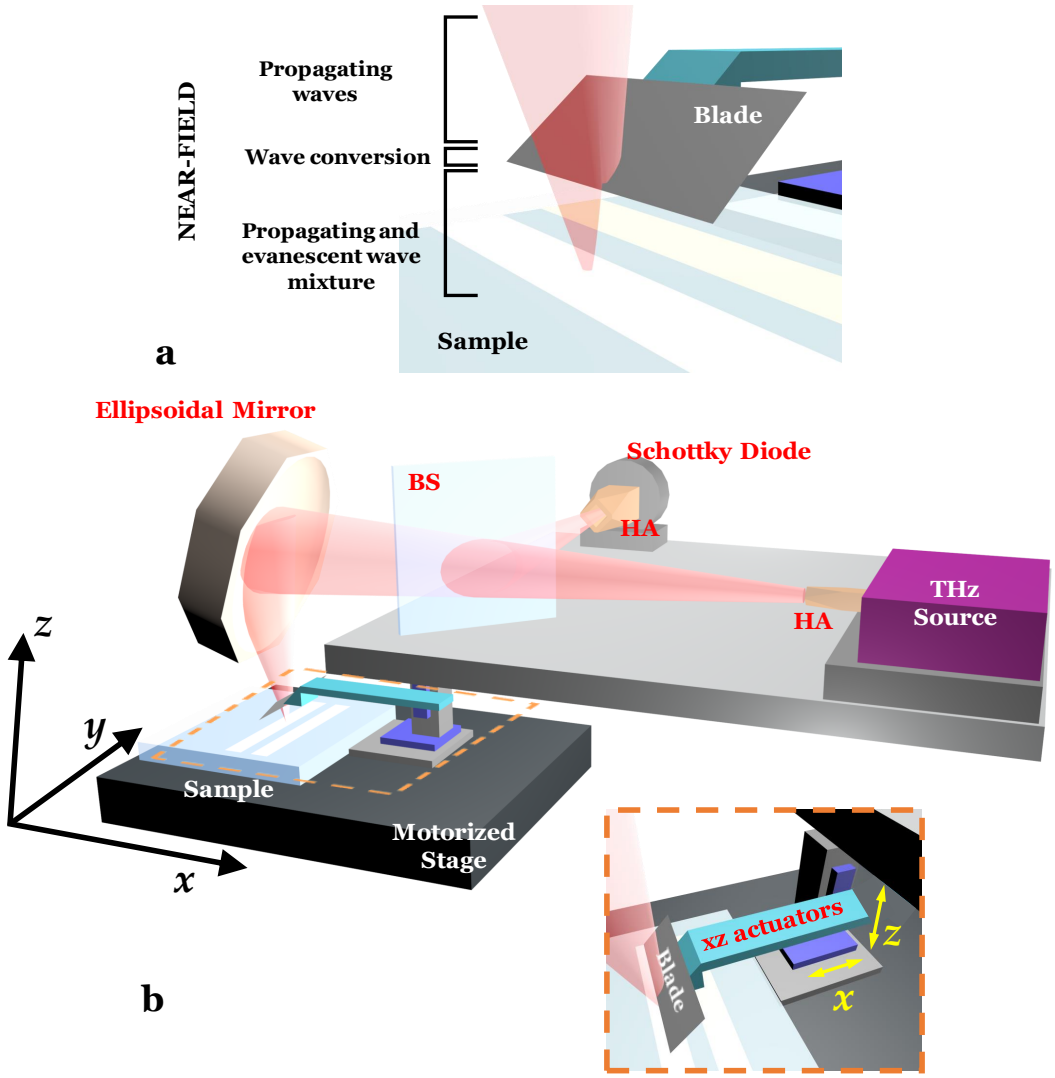

Figure 9.1. (a) Knife-edge super-resolution scheme. (b) THz setup. The apparatus is a modified confocal microscope: the radiation at 0.300 THz goes from the source to the sample throughout a quartz beam-splitter (BS). The Schottky diode detector is placed at the same distance 310 mm from the sample as the source. The ellipsoidal Mirror behaves both as focalizing lens and collection lens. Motorized xyz stages allow to place the sample in the focal plane and make the raster scan. (c) Sketch of the knife-edge profiling system with a steel blade moved by xz actuators. Waveguide-based radiation sources and detectors coupled to the free space using horn antennas (HA) ensure that only light which is focused in the diffraction-limited spot is actually fed into the waveguide [264].

9.4 Experiments

We assembled the reflective confocal microscope sketched in Fig. 9.1(b), similar to experimental setup of Ref.[247], with an added knife-edge profiling system. The microscope

operates at $\lambda = 1.00$ mm ($\nu = 0.300$ THz) with a reflective objective with high numerical aperture NA$\simeq 0.5$. According to the Rayleigh criterion,the diffraction-limited resolution leads that two linear image details are resolved if they are distant more than $\Delta x = \lambda/2\text{NA}$ in one-directional scans of the sample in the focal spot [247]. The THz source is an amplifier-multiplier chain (AMC, by Virginia Diodes Inc.). The horn antenna mounted at the end of the AMC emits TEM_{00} radiation with a relative bandwidth $\Delta\lambda/\lambda \simeq 5 \cdot 10^{-3}$ and constant continuous-wave power of ~ 0.1 mW. The detector is a zero-bias Schottky diode (ZBD, by Virginia Diodes Inc.) featuring a noise equivalent power of 1 nW/Hz$^{0.5}$ at the sampling rate of 40 s^{-1}. The fully opaque knife is a steel shaving blade, displaced by a step-motor with step precision better than 0.05 μm, much below the typical sampling step size of 10 μm, itself much shorter than λ. The total quartz beamsplitter efficiency is calculated to be ~ 0.1 at $\lambda = 1.00$ mm [247]. The S/N ratio is 10^3 per pixel for a totally reflecting sample, while the apparent noise in the images and in the linescans is due to fluctuations in atmospheric absorption and source temperature during the image acquisition, and the noise obviously increases in the super-resolved reconstructions which require a full set of about 1000 images. The investigated samples are optical lithography masks, made of fused silica coated with a 30 nm thick chromium film patterned by electron beam lithography into stripes and squares of different sizes. The root-mean square edge sharpness is better than 5 nm. The reflectivity of the chromium film in the THz range is $R_{\text{Cr}} = 0.99$, while the reflectivity of an infinitely thick fused silica plate at normal incidence is $R_{\text{SiO}_2} = 0.08$ hence providing strong optical image contrast.

The functioning of the knife-edge super-resolved imaging is conceptually demonstrated by the violation of the Rayleigh principle in the reconstructed images seen in Fig. 9.2. Therein, the knife-edge scan plane is at a distance $z \simeq 25$ μm $= \lambda/40$, deep into the near-field of the object plane. Two parallel stripes at a distance of 230 μm, i.e. (visible light photography reported in Fig. 9.2(a)) were imaged. The distance between the stripes lies below well below the limit set by the Rayleigh criterion $\Delta x \sim 1$ mm. When no knife-edge scan is implemented, a single broad feature is observed in the confocal microscopy image of Fig. 9.2(b). The two stripes are too close and cannot be resolved. In turn, when the knife-edge scan reconstruction is enacted following the recipe of Eq. (9.1), the two reflecting stripes are clearly distinguished on the non-relfecting background, as reported in Fig. 9.2(c). To quantitatively evaluate the imaging resolution reached in the super-resolved reconstruction, we imaged a sharp border between a chromium surface and a bare silica surface [Fig. 9.2(d) shows the border using visible light]. The imaging resolution is evaluated by calculating the slope of the linescan variation from 10% to 90% of the intensity profile of the border. Without the knife-edge technique, we measure a slope of 0.91 mm^{-1} corresponding to an Abbe diffraction limit of 1.1 mm, as shown in Fig. 9.2(e). In Fig. 9.2(f) we report the maximum resolution achieved using the near-field knife-edge scan. We

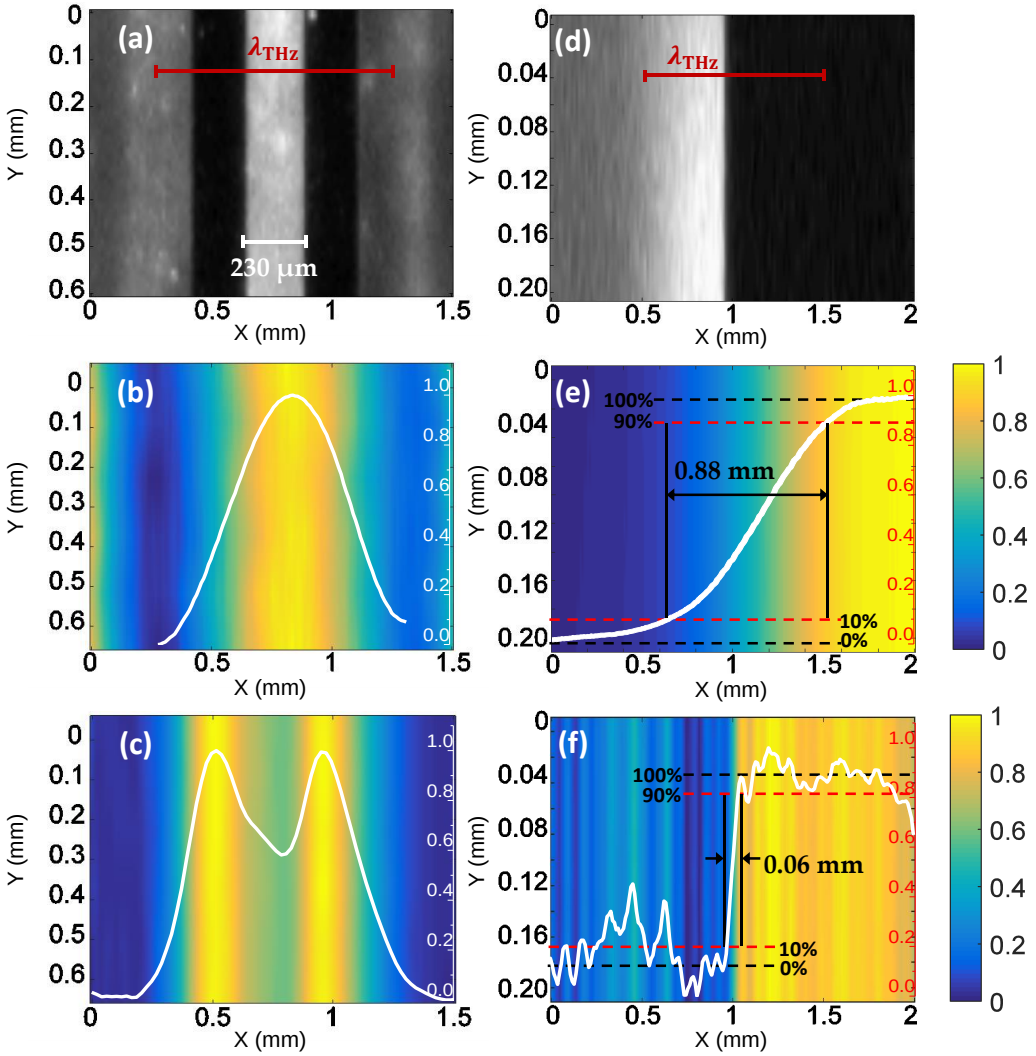

Figure 9.2. (a-c) Imaging of two chromium stripes on a fused silica substrate, distant 230 μm $\simeq \lambda/4$ from each other. (a) Image taken with visible camera. (b) Image taken with the scanning THz ($\lambda = 1$ mm) confocal microscope. (c) Super-resolved image. The two peaks are clearly distinguished. (d-f) Imaging of a chromium/silica border. (d) Image taken with visible camera. (e) Image taken with the scanning THz confocal microscope. (f) Super-resolved image with 0.06 mm $\simeq \lambda/17$ linescan profile width. Images (c) and (f) are achieved applying Eq. (9.1) respectively on 76 images one for each 20 μm knife-edge step and 201 images with 10 μm steps. Profiles and images are in arbitrary units.

measured a slope of 13.3 mm^{-1} corresponding to a striking sub-wavelength resolution of approximately 0.06 mm, or $\lambda/17$. The observed imaging resolution is still six times larger than the single step in the confocal microscopy scan of 10 μm), which was chosen as it roughly corresponded with the actual physical sharpness of the blade evaluated with an optical microscope, therefore a different reason has to be found for the observed imaging resolution of the order of 60 μm. In fact, as discussed below, the imaging resolution is

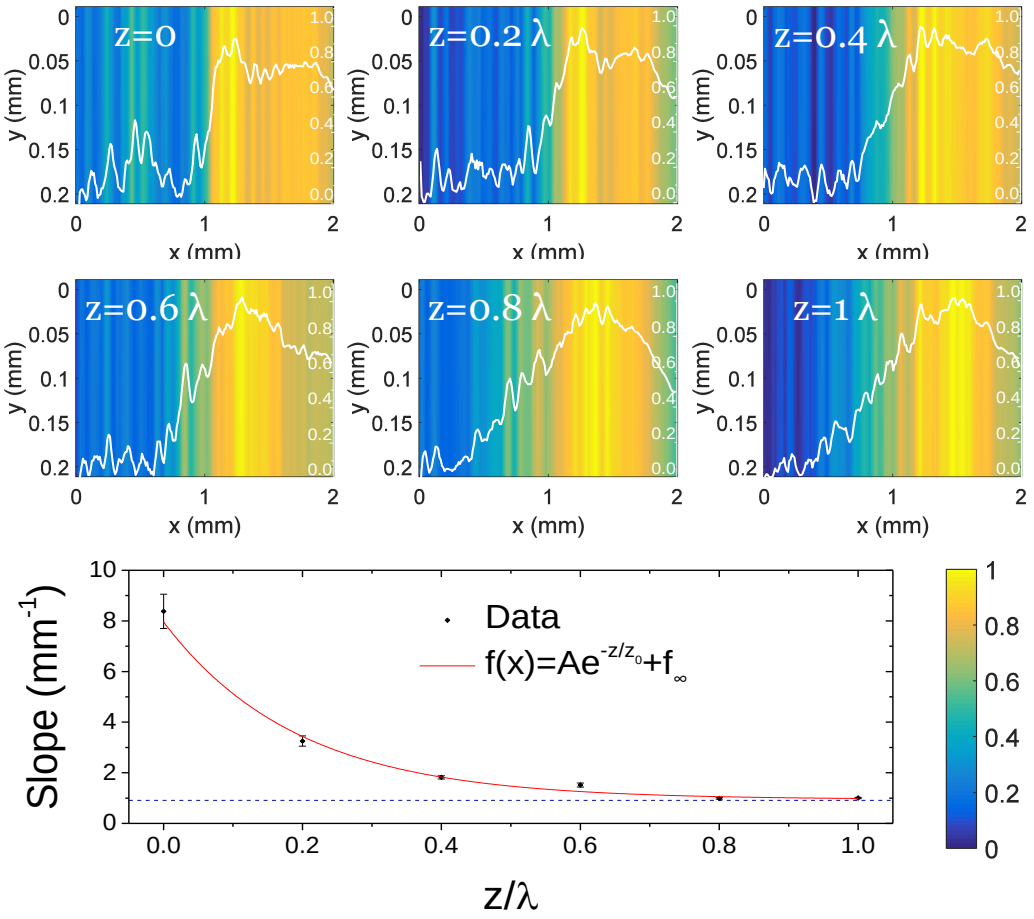

Figure 9.3. Transition from near-field imaging to diffraction-limited imaging. (Top) As the evanescent-to-propagating wave conversion is performed at $z > 0$, farther from the emitting/reflecting surface, the sharp edge is progressively smeared out (white line represents the profile). (Bottom) The slope of the linescan profile as a function of z. Points are experimental data whereas the red line is a guide to the eye represented by the function $f(z) = A\exp(-z/z_0)+f_\infty$ where: $A = (7.0 \pm 1.3)$ mm^{-1}, $z_0 = (0.19 \pm 0.03)$ mm and $f_\infty = (0.95 \pm 0.07)$ mm^{-1}. The blue dashed line is $f(z) = 0.91$ mm^{-1} calculated from the normalized value of the slope of Fig. 9.2(e) with no knife-edge. Profiles and images are in arbitrary units.

dominated by the spatial width of the edge diffraction pattern. The finite imaging resolution can be modeled by substituting $\theta(x-x')$ in Eq. (9.1) with $f_d(x) = \frac{1}{2} + \frac{1}{2}\text{erf}\left(\frac{x-x'}{d}\right)$, where $\text{erf}(x)$ is the error-function, so that Eq. (9.1) can be rewritten as

$$\begin{aligned} I_S(x,z) &= -\int_{\mathbb{R}} I(u,z)\frac{d}{dx'}f_d(u-x')du \\ &= \int_{\mathbb{R}} I(u,z)e^{\frac{(u-x')^2}{d^2}}du, \end{aligned} \tag{9.2}$$

where a new convolution integral intervenes and the term $\exp((u-x')^2/d^2)$ behaves as an

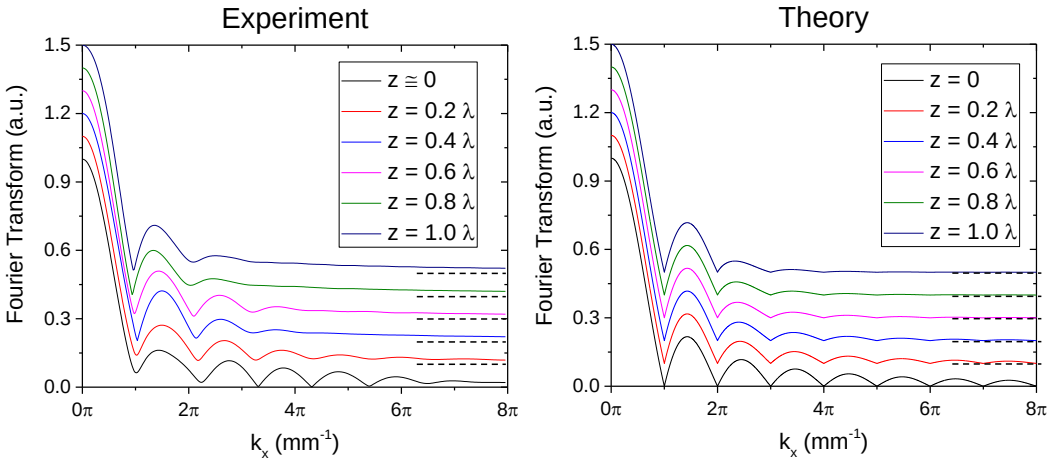

Figure 9.4. Filtering of the spatial frequency spectrum in the transition from near-field imaging to diffraction-limited imaging as the distance z between object plane and structured illumination plane increases. (Left) Plot of the spectrum displaying a spatial frequency-dependent characteristic decay length, shorter at higher frequencies; (Right) corresponding theoretical prediction obtained exploiting the expressions in Eq. (9.3).

effective PSF, and $d \approx 60$ μm quantifies the "effective sharpness" of the blade. The image in Fig. 9.2(c) is taken using an x-oriented raster scan. Instead, the images in Fig. 9.2(f) and Fig. 9.3 are taken with a y-oriented raster scan. This latter raster scan mode allows one to obtain the most reliable value of the super-resolution because the data along the y direction can be readily integrated before image reconstruction, but it inevitably causes spurious oscillations in the reconstructed image, as the data of adjacent points in the x direction are taken at very different times after one entire y linescan. The multi-peak structure appearing around $x = 0.5$ mm in Fig. 9.2(f) probably has a different physical origin not related to super-resolution imaging, and it will be discussed further on in this paper.

9.5 Results

The progressive filtering out of the high spatial frequency components from the super-resolved images, caused by the decay of the intensity of the evanescent waves scattered by the blade edge when z is increased, is made evident in Fig. 9.3. In the top panel the reconstructed lineascans similar to that of Fig. 9.2(f) are shown for several z values. As z increases, one sees the decrease of the slope of the image intensity step corresponding to the metal/silica border on the sample surface. The lateral (super-)resolution can be still defined as the inverse of this slope, and it is reported in the bottom panel of Fig. 9.3. Interestingly, the slope does not drop to zero for $z \to \lambda$, but tends to the value $f_\infty = 0.91$ mm^{-1} of the standard confocal microscopy image of Fig. 9.2(e) taken with no blade in the beam path. This asymptotic value of the super-resolution is indicated as a horizontal blue

dashed line in the bottom panel of Fig. 9.3. This fact indicates that, as the intensity of the evanescent waves intercepted by the blade at the given plane z becomes negligible, only the propagating waves are scattered by the blade, and the reconstructed image displays the same lateral resolution as the image without a blade. The red line is an exponential fit to $f(z) = A\exp(-z/z_0) + f_\infty$, which delivers $z_0 = 0.19$mm, however, as we now explain, a single characteristic exponential decay length for the loss of super-resolution with increasing z cannot be defined.

The experimental spatial frequency spectrum is finally calculated as the one-dimensional Fourier transform of the linescans in Fig. 9.3 and plotted in the left panel of Fig. 9.4. The amplitude decay with increasing z is more rapid for the Fourier components at higher frequency k_x, rather than homogeneously at all k_x values. We underline that this phenomenon is not related to energy dissipation, as it occurs without a corresponding attenuation in the total reflected beam intensity, but rather it is the signature of the progressively reduced capability of the blade edge to scatter the evanescent waves in vacuum towards the far-field. As a consequence, the contribution of the evanescent waves to the super-resolved image is progressively filtered out with increasing z, and more rapidly for higher k_x. The experimental spectral filtering can be compared to the theoretical expectation plotted in the right panel of Fig. 9.4, derived from the Fourier transform of the simplified theoretical linescan of Eq. (9.2):

$$\begin{aligned} E(k_x, z) &= E(k_x, z=0)e^{i(k_0^2-k_x^2)^{1/2}z} \ (k_x < k_0) \\ E(k_x, z) &= E(k_x, z=0)e^{-(k_x^2-k_0^2)^{1/2}z} \ (k_x > k_0). \end{aligned} \tag{9.3}$$

The main features of the experimental spectra in Fig. 9.4 are captured by the theoretical model of Eq. (9.3). As z is increased, there is no single exponential decay length of the image resolution, but rather each k_x component has its own decay length. As z approaches $\lambda/2$, all secondary peaks in the spectra are filtered out apart from the first one around $k_x \sim 15$ mm^{-1}, i.e. only the slowest decaying $k_x \gtrsim 2\pi/\lambda$ at the edge of the Ewald sphere are still scattered to the far field by the blade. This explains the rough validity of the single exponential fit in Fig. 9.3, with decay length $z_0 = 0.19$ which can be attributed to the lowest spatial frequency peak at $k_x \sim 15$ mm^{-1} just outside the Ewald sphere. Apparently, this peak alone is sufficient to obtain a super-resolution of 0.5 mm $\sim \lambda/2$, beyond the diffraction limit $\lambda/2\text{NA} \sim 1$ mm, for a considerable distance of the object plane from the blade scanning plane of $0.4\lambda \sim 400$ μm, i.e., the blade does not need to graze the surface in a terahertz super-resolution microscope.

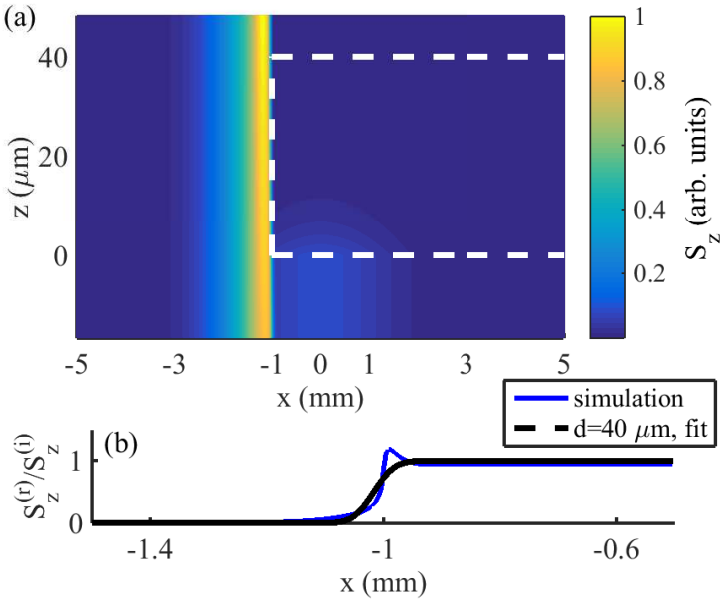

Figure 9.5. Numerical electromagnetic simulation of a Gaussian beam with $\nu = 0.300$ THz scattered by a semi-infinite conducting slab of finite thickness t = 40 μm. The slab extends in the x, y plane and it sits at 20 μm from a non-reflecting surface. (a) Image plot of the z-component of the Poynting-vector $S_z(x, z)$. The dashed white lines are the borders of the slab. Note the very different scale for the z and x axes. (b) Plot of $S_z^{(r)}/S_z^{(i)}$ (solid line) where $S_z^{(r)}$ and $S_z^{(i)}$ are the z-components of the Poynting-vector of the reflected and the incident beam at the $z = 0$ plane. The dashed black line is the experimental fit of the function $f_d(x) = \frac{1}{2} + \frac{1}{2}\text{erf}(\frac{x-x'}{d})$ for $d = 60$ μm and $x' = -1.02$ mm.

9.6 Ultimate resolution limit

In order to evaluate the ultimate limit to the super-resolution attained by our technique we have performed a two-dimensional full-wave electromagnetic simulation of the radiation scattering by a metal blade illuminated with a focused Gaussian beam at 0.300 THz. We consider a monochromatic linearly polarized Gaussian beam. The incident field is $\mathbf{E}(x) = \text{Re}[E_0 \exp(-x^2/\sigma^2 - i\omega t)]\mathbf{e}_y$ where E_0 is a constant, $\omega = 2\pi c/\lambda$ and $\sigma = 2\lambda = 2$ mm. The analyzed scattering geometry is shown in Fig. 9.5(a). The conducting slab representing the blade has a dielectric constant $\epsilon_r = -150 + i50$ and thickness $L = 40$ μm. We analyze the situation where the incident beam is centered at $x = 0$ and the physical blade edge is at $x = -1.00$ mm, a situation in which the blade should fully obstruct the incident beam, and we monitor the correspondence of the scattered field pattern with the physical position and sharpness of the blade edge. Given the very different length scales involved (λ, z, L) and the presence of metallic surfaces, the simulation is not trivial. The computational domain is terminated with perfect electric conductor conditions at the $x = \pm 6$ mm planes and we adopt scattering boundary conditions at the entrance ($z = -17$ μm) and at the exit ($z = 50$ μm) facets of the domain. A suitable discretization of the computational domain is

implemented with a maximum and a minimum mesh size of $0.2\ mm$ and $2\ \mu$m, respectively (which leads to 125895 degrees of freedom), and we use the UMFPACK direct solver[1] with default parameters. In Fig. 9.5(a), we show the z-component of the Poynting-vector $\mathbf{S}(x,z) = \frac{1}{2}\,\mathrm{Re}[\mathbf{E} \times \mathbf{H}^*]$. The color plot indicates that even for an infinitely sharp blade edge, the scattering pattern has a finite dimension and a complex structure, related to well-known edge diffraction patterns by opaque screens [236]. The center of this finite-size field distribution is not at the blade edge (here $x = -1.02$ mm), but just outside it, at $x' < x$. In Fig. 9.5(b) we display $S_z^{(r)}/S_z^{(i)}$ (solid line) where $S_z^{(r)}$ and $S_z^{(i)}$ are the z-components of the Poynting-vector of the reflected and the incident beam at the plane $z = 0$, respectively. The ratio $S_z^{(r)}/S_z^{(i)}$ (blue continuous line) represents the effective electromagnetic sharpness of an infitely sharp blade and therefore the ultimate limit of our super-resolution scheme. In Fig. 9.5(b) we superimpose the numerical prediction (blue curve) with the profile function $f_d(x)$ introduced in Eq. (9.2) (black dashed line) with the experimentally determined value $d = 60\ \mu$m and field distribution offset $x' = -1.02$ mm. The experimental fit to $f_d(x)$ is done with the least square method for x' and fixing $d = 60\ \mu$m from Fig. 9.2(f). While the offset of 0.02 mm between the reconstructed image and the object is not visible in our experiment, we can conclude from the good superposition of Fig. 9.5(b) that edge diffraction at the blade termination explains well the maximum observed resolution of 60μm or $\lambda/17$.

Finally, we note that the polarization direction of the electric field vector can slightly affect the knife-edge reconstruction algorithm [265] therefore, for comparison, the image in Fig. 9.2(c) is taken with polarization parallel to the blade edge (y-axis) while Fig. 9.2(f) is taken with polarization orthogonal to it (along the x-axis). While the fundamental observation of super-resolution is achieved in both cases, in the latter case the orthogonal polarization should also excite cavity modes between the metal blade and the metal film on the sample surface. The detailed study of such parasitic proximity effects is beyond the scopes of this work, but we speculate that they may be responsible for the multi-peak structure seen around $x = 0.5$ mm in Fig. 9.2(f), where one would instead expect a plateau of very low value of the reconstructed image pixels. As a partial confirmation of the above, the multi-peak structure fades away as soon as the blade is lifted from the sample surface already at $z \sim 0.2\lambda$, i.e. well below the cut-off distance of evanescent-wave filtering. Therefore, the multi-peak structure must be related to near-field oscillations (e.g. surface plasmon polaritons) whose field extends only in a deeply subwavelength range of z values.

9.7 Discussion

From a fundamental perspective, our study provides first experimental evidence into the effect of so-called rigorous diffraction theory on super-resolved terahertz imaging

[1] COMSOL Group, COMSOL Multiphysics: Version 3.4

[236]. Here, at the transition between the near-field region and the diffraction-limited wave propagation region, a mixed regime known as Rayleigh-Sommerfeld diffraction is observed.

The imaging method expands THz beam profiling methods and appears fundamentally different from previous imaging techniques since it taps into the full non-paraxial mixture of different spatial Fourier components both inside and outside the Ewald sphere. In a Scanning Near-Field Optical Microscope [266–270], the tip acts as the equivalent of a delta-function in space, capturing and combining the whole spatial spectrum without distinguishing between diffraction-limited and evanescent components, so properties associated to evanescent waves have to be detected by suitable near-field demodulation techniques. Specifically, in a near-field probe experiment, resolution falls off far more rapidly than predicted by Eq. 9.3, typically at distances from the emitters below $\lambda/6$ (see, for example, Fig. 9.3 in Ref.[271]).

In order to perform super-resolved terahertz imaging beyond the edge of the Ewald sphere, it is required to work at a single wavelength, excluding methods based on wide-band excitation where the concept of diffraction-limit is not clear-cut and the highest resolution in the images could potentially be carried by short wavelength components of the frequency spectrum [272, 273].

From a practical point of view, since no sub-wavelength source or detector is used [274, 275], our scheme circumvents the need for a sub-wavelength aperture with its crippling many-orders-of-magnitude toll on transmitted power [273, 276], enacts super-resolution with the losses typical of a standard confocal scheme [277], and does not require ultra-sensitive detectors (such as cryogenic bolometers [273]) or high power sources (such as gas lasers [278, 279]).

9.8 Future Perspectives

In summary, we report the first observation of the progressive transition from near-field imaging to diffraction-limited imaging when the structured illumination plane is lifted from the object plane by distances of the order of one wavelength. The effect is attributed to evanescent wave intensity decay and it is detected using a remote mechanical knife-edge scan technique in a confocal terahertz imaging system. The loss of imaging super-resolution is associated with filtering of the spatial frequency spectrum of the image, where higher spatial frequencies decay more rapidly with increasing distance and a single exponential decay length cannot be defined for the evanescent wave intensity. The findings have immediate impact on the development of super-resolved terahertz imaging, terahertz imaging of buried structures, and in general for super-resolution imaging in the cases of opaque media and of non-planar emitter surfaces, where the object plane and the structured illumination plane may not be easily made to coincide.

Conclusions

In This thesis we have explored several new optical phenomena that arise from both specifically designed light patterns or from the physics of nanodisordered ferroelectric materials.

We have introduced an innovative approach to treat cumulative nonlinearity and specifically the photorefractive effect. We have demonstrated that the field temporal evolution can be mapped into a spatial evolution. This correspondence allows us to observe and describe the Fermi-Pasta-Ulam-Tsingou recurrence but also Bessel beam self-trapping with its breathing feature and discrete-to-continuous soliton transformation in the nonlinear grating embedded in a ferroelectric crystal. This lattice causes a nanodisordered ferroelectric perovskite to turn into a super-crystal. We have characterized this new phase studying the birefringence and the second harmonic generation: in all experiments footprints of super-crystal are found. In particular, we have found evidences of periodic structure also in the material that allows us to report the highest value of refractive index for visible light: $n > 26$. In addition we have investigated the near field to grasp the role of evanescent waves. We conveniently adopt THz wave to build a remote knife-edge super-resolution setup that allow us to observe decaying of resolution as the near field turns into far field.

Acknowledgments

I acknowledge my tutor Prof. Eugenio Del Re for his constant and essential guide and all the members, past and present, of the Photonics Group at Physics Department at Sapienza University of Rome: Davide Pierangeli, Ludovica Falsi, Giuseppe Di Domenico, Fabrizio Di Mei, Paolo Di Porto, Feifei Xin, Fabiano Evangelista, Giulia Marcucci and Claudio Conti.

I thank for their relevant contribution Paolo Maria Santini from Sapienza University of Rome, Luca Tartara and Giambattista Parravicini from Pavia University, Jacopo Parravicini from Milano-Bicocca University and Aharon J. Agranat from the Hebrew University of Jerusalem.

Furthermore I acknowledge all the other collaborators and coauthors: Michele Ortolani, Valeria Giliberti, Mauro Missori, Alessandro Ciattoni and Carlo Rizza.

A special thank goes to my mother Antonella, father Quinto and brother Gabriele and all my relatives for moral and economic support.

Finally I'd like to thank all my friends and my students with whom I have shared my PhD experience.

Bibliography

[1] D. Pierangeli et al. “Observation of Fermi-Pasta-Ulam-Tsingou Recurrence and Its Exact Dynamics”. In: *Phys. Rev. X* 8 (4 2018), p. 041017.

[2] Mariano Flammini et al. “Observation of Bessel-beam self-trapping”. In: *Physical Review A* 98.3 (2018), p. 033808.

[3] D Pierangeli et al. “Continuous solitons in a lattice nonlinearity”. In: *Physical review letters* 114.20 (2015), p. 203901.

[4] J. D. Jackson. *Classical electrodynamics*. John Wiley & Sons, 2012.

[5] Eugenio DelRe, Bruno Crosignani, and Paolo Di Porto. “Photorefractive solitons and their underlying nonlocal physics”. In: *Progress in Optics* 53 (2009), p. 153.

[6] HS Eisenberg et al. “Discrete spatial optical solitons in waveguide arrays”. In: *Physical Review Letters* 81.16 (1998), p. 3383.

[7] Franco Dalfovo et al. “Theory of Bose-Einstein condensation in trapped gases”. In: *Reviews of Modern Physics* 71.3 (1999), p. 463.

[8] Norden E Huang, Zheng Shen, and Steven R Long. “A new view of nonlinear water waves: the Hilbert spectrum”. In: *Annual review of fluid mechanics* 31.1 (1999), pp. 417–457.

[9] Igor S Aranson and Lorenz Kramer. “The world of the complex Ginzburg-Landau equation”. In: *Reviews of Modern Physics* 74.1 (2002), p. 99.

[10] Kevin E Strecker et al. “Formation and propagation of matter-wave soliton trains”. In: *Nature* 417.6885 (2002), p. 150.

[11] Arnaud Couairon and André Mysyrowicz. “Femtosecond filamentation in transparent media”. In: *Physics reports* 441.2-4 (2007), pp. 47–189.

[12] DR Solli et al. “Optical rogue waves”. In: *Nature* 450.7172 (2007), p. 1054.

[13] Andrey E Miroshnichenko, Sergej Flach, and Yuri S Kivshar. “Fano resonances in nanoscale structures”. In: *Reviews of Modern Physics* 82.3 (2010), p. 2257.

[14] B.E.A. Saleh and M. C. Teich. *Fundamentals of photonics*. Vol. 22. Wiley New York, 1991.

[15] F. Gori. *Elementi di ottica*. Accademica, 1997.

[16] Michael V Berry and Nandor L Balazs. "Nonspreading wave packets". In: *American Journal of Physics* 47.3 (1979), pp. 264–267.

[17] J1 Durnin, JJ Miceli Jr, and JH Eberly. "Diffraction-free beams". In: *Physical review letters* 58.15 (1987), p. 1499.

[18] Miguel A Bandres and Julio C Gutiérrez-Vega. "Airy-Gauss beams and their transformation by paraxial optical systems". In: *Optics Express* 15.25 (2007), pp. 16719–16728.

[19] F Gori, G Guattari, and C Padovani. "Bessel-gauss beams". In: *Optics communications* 64.6 (1987), pp. 491–495.

[20] Peng Zhang et al. "Generation of acoustic self-bending and bottle beams by phase engineering". In: *Nature communications* 5 (2014), p. 4316.

[21] Zhou Lin et al. "Acoustic non-diffracting Airy beam". In: *Journal of Applied Physics* 117.10 (2015), p. 104503.

[22] ZhenYu Hong, Jie Zhang, and Bruce W Drinkwater. "Observation of orbital angular momentum transfer from Bessel-shaped acoustic vortices to diphasic liquid-microparticle mixtures". In: *Physical review letters* 114.21 (2015), p. 214301.

[23] Melanie McLaren et al. "Self-healing of quantum entanglement after an obstruction". In: *Nature communications* 5 (2014), p. 3248.

[24] Juanying Zhao et al. "Observation of self-accelerating Bessel-like optical beams along arbitrary trajectories". In: *Optics letters* 38.4 (2013), pp. 498–500.

[25] GA Siviloglou et al. "Observation of accelerating Airy beams". In: *Physical Review Letters* 99.21 (2007), p. 213901.

[26] Pavel Polynkin et al. "Generation of extended plasma channels in air using femtosecond Bessel beams". In: *Optics express* 16.20 (2008), pp. 15733–15740.

[27] Cord L Arnold et al. "Nonlinear Bessel vortex beams for applications". In: *Journal of Physics B: Atomic, Molecular and Optical Physics* 48.9 (2015), p. 094006.

[28] Chen Xie et al. "Tubular filamentation for laser material processing". In: *Scientific reports* 5 (2015), p. 8914.

[29] Florian O Fahrbach et al. "Light-sheet microscopy in thick media using scanned Bessel beams and two-photon fluorescence excitation". In: *Optics express* 21.11 (2013), pp. 13824–13839.

[30] David McGloin and Kishan Dholakia. "Bessel beams: diffraction in a new light". In: *Contemporary Physics* 46.1 (2005), pp. 15–28.

[31] A. Ashkin et al. “Optically-Induced Refractive Index Inhomogeneities in LiNbO3 and LiTaO3”. In: *Applied Physics Letters* 9.1 (1966), pp. 72–74.

[32] P Yeh. “Two-wave mixing in nonlinear media”. In: *IEEE Journal of Quantum Electronics* 25.3 (1989), pp. 484–519.

[33] Peter Günter and Jean Pierre Huignard. *Photorefractive Materials and Their Applications 2: Materials*. Vol. 114. Springer, 2007.

[34] N.V. Kukhtarev. “Kinetics of hologram recording and erasure in electrooptic crystals”. In: *Pisma v Zhurnal Tekhnischeskoi Fiziki* 2 (1976), pp. 1114–1119.

[35] J. Petter et al. “Self-bending of photorefractive solitons”. In: *Optics communications* 170.4-6 (1999), pp. 291–297.

[36] Eugenio DelRe and Elia Palange. “Optical nonlinearity and existence conditions for quasi-steady-state photorefractive solitons”. In: *JOSA B* 23.11 (2006), pp. 2323–2327.

[37] Julien Fatome et al. “Observation of optical undular bores in multiple four-wave mixing”. In: *Physical Review X* 4.2 (2014), p. 021022.

[38] Linn F Mollenauer, Roger H Stolen, and James P Gordon. “Experimental observation of picosecond pulse narrowing and solitons in optical fibers”. In: *Physical Review Letters* 45.13 (1980), p. 1095.

[39] Bertrand Kibler et al. “The Peregrine soliton in nonlinear fibre optics”. In: *Nature Physics* 6.10 (2010), p. 790.

[40] Stephane Barland et al. “Cavity solitons as pixels in semiconductor microcavities”. In: *Nature* 419.6908 (2002), p. 699.

[41] A Chabchoub, NP Hoffmann, and Nail Akhmediev. “Rogue wave observation in a water wave tank”. In: *Physical Review Letters* 106.20 (2011), p. 204502.

[42] Eugenio DelRe et al. “Scale-free optics and diffractionless waves in nanodisordered ferroelectrics”. In: *Nature Photonics* 5.1 (2011), p. 39.

[43] Mordechai Segev and Aharon J Agranat. “Spatial solitons in centrosymmetric photorefractive media”. In: *Optics letters* 22.17 (1997), pp. 1299–1301.

[44] Eugenio DelRe et al. “One-dimensional steady-state photorefractive spatial solitons in centrosymmetric paraelectric potassium lithium tantalate niobate”. In: *Optics letters* 23.6 (1998), pp. 421–423.

[45] Demetrios N Christodoulides and MI Carvalho. “Bright, dark, and gray spatial soliton states in photorefractive media”. In: *JOSA B* 12.9 (1995), pp. 1628–1633.

[46] D Burak and W Nasalski. “Gaussian beam to spatial soliton formation in Kerr media”. In: *Applied optics* 33.27 (1994), pp. 6393–6401.

[47] E DelRe et al. “Photorefractive solitons”. In: *Photorefractive Materials and Their Applications 1*. Springer, 2006, pp. 317–367.

[48] E DelRe et al. “Pairing space-charge field conditions with self-guiding for the attainment of circular symmetry in photorefractive solitons”. In: *Applied physics letters* 85.23 (2004), pp. 5499–5501.

[49] Yuri S Kivshar and Govind Agrawal. *Optical solitons: from fibers to photonic crystals*. Academic press, 2003.

[50] Alexander Dreischuh et al. “Observation of attraction between dark solitons”. In: *Physical review letters* 96.4 (2006), p. 043901.

[51] Eugenio DelRe, Stefano Trillo, and Aharon J Agranat. “Collisions and inhomogeneous forces between solitons of different dimensionality”. In: *Optics letters* 25.8 (2000), pp. 560–562.

[52] Vladimir Tikhonenko, Jason Christou, and Barry Luther-Davies. “Three dimensional bright spatial soliton collision and fusion in a saturable nonlinear medium”. In: *Physical Review Letters* 76.15 (1996), p. 2698.

[53] George I Stegeman and Mordechai Segev. “Optical spatial solitons and their interactions: universality and diversity”. In: *Science* 286.5444 (1999), pp. 1518–1523.

[54] VV Steblina, Yu S Kivshar, and AV Buryak. “Scattering and spiraling of solitons in a bulk quadratic medium”. In: *Optics letters* 23.3 (1998), pp. 156–158.

[55] Alexander V Buryak et al. “Induced coherence and stable soliton spiraling”. In: *Physical review letters* 82.1 (1999), p. 81.

[56] Ido Kaminer et al. “Periodic solitons in nonlocal nonlinear media”. In: *Optics letters* 32.21 (2007), pp. 3209–3211.

[57] JS Aitchison et al. “Experimental observation of spatial soliton interactions”. In: *Optics letters* 16.1 (1991), pp. 15–17.

[58] VE Zakharov and LA Ostrovsky. “Modulation instability: the beginning”. In: *Physica D: Nonlinear Phenomena* 238.5 (2009), pp. 540–548.

[59] Miguel Onorato et al. “Rogue waves and their generating mechanisms in different physical contexts”. In: *Physics Reports* 528.2 (2013), pp. 47–89.

[60] Kristian Dysthe, Harald E Krogstad, and Peter Müller. “Oceanic rogue waves”. In: *Annu. Rev. Fluid Mech.* 40 (2008), pp. 287–310.

[61] D Pierangeli et al. “Spatial rogue waves in photorefractive ferroelectrics”. In: *Physical review letters* 115.9 (2015), p. 093901.

[62] D Pierangeli et al. “Photorefractive light needles in glassy nanodisordered KNTN”. In: *Optics letters* 39.6 (2014), pp. 1657–1660.

[63] Joseph W Goodman. "Statistical properties of laser speckle patterns". In: *Laser speckle and related phenomena*. Springer, 1975, pp. 9–75.

[64] Stefan Wabnitz. *Nonlinear guided wave optics: a testbed for extreme waves*. IOP Publishing, 2017.

[65] Clifford R Pollock and Michal Lipson. *Integrated photonics*. Vol. 20. 25. Springer, 2003.

[66] Christopher Barsi, Wenjie Wan, and Jason W Fleischer. "Imaging through nonlinear media using digital holography". In: *Nature Photonics* 3.4 (2009), p. 211.

[67] Daan Frenkel and Berend Smit. *Understanding molecular simulation: from algorithms to applications*. Vol. 1. Elsevier, 2001.

[68] T Dauxois. "Fermi, Pasta, Ulam, and a mysterious lady". In: *Phys. Today* 61 (2008), pp. 55–57.

[69] Joseph Ford. "The Fermi-Pasta-Ulam problem: paradox turns discovery". In: *Physics Reports* 213.5 (1992), pp. 271–310.

[70] PG Grinevich and PM Santini. "The finite gap method and the analytic description of the exact rogue wave recurrence in the periodic NLS Cauchy problem. 1". In: *arXiv preprint arXiv:1707.05659v2* (2017).

[71] PG Grinevich and PM Santini. "The exact rogue wave recurrence in the NLS periodic setting via matched asymptotic expansions, for 1 and 2 unstable modes". In: *Physics Letters A* 382.14 (2018), pp. 973–979.

[72] E. Fermi et al. *Studies of the nonlinear problems*. Tech. rep. Los Alamos Scientific Lab., N. Mex., 1955.

[73] GP Berman and FM Izrailev. "The Fermi–Pasta–Ulam problem: fifty years of progress". In: *Chaos: An Interdisciplinary Journal of Nonlinear Science* 15.1 (2005), p. 015104.

[74] Giovanni Gallavotti. *The Fermi-Pasta-Ulam problem: a status report*. Vol. 728. Springer, 2007.

[75] Giancarlo Benettin, Helen Christodoulidi, and Antonio Ponno. "The Fermi-Pasta-Ulam problem and its underlying integrable dynamics". In: *Journal of Statistical Physics* 152.2 (2013), pp. 195–212.

[76] Miguel Onorato et al. "Route to thermalization in the α-Fermi–Pasta–Ulam system". In: *Proceedings of the National Academy of Sciences* 112.14 (2015), pp. 4208–4213.

[77] M Guasoni et al. "Incoherent fermi-pasta-ulam recurrences and unconstrained thermalization mediated by strong phase correlations". In: *Physical Review X* 7.1 (2017), p. 011025.

[78] Yuri V Lvov and Miguel Onorato. "Double Scaling in the Relaxation Time in the β-Fermi-Pasta-Ulam-Tsingou Model". In: *Physical review letters* 120.14 (2018), p. 144301.

[79] Stefan Wabnitz and Benjamin Wetzel. "Instability and noise-induced thermalization of Fermi–Pasta–Ulam recurrence in the nonlinear Schrödinger equation". In: *Physics Letters A* 378.37 (2014), pp. 2750–2756.

[80] O Kimmoun et al. "Modulation instability and phase-shifted Fermi-Pasta-Ulam recurrence". In: *Scientific reports* 6 (2016), p. 28516.

[81] S Trillo et al. "Experimental observation and theoretical description of multisoliton fission in shallow water". In: *Physical review letters* 117.14 (2016), p. 144102.

[82] Mingzhong Wu and Carl E Patton. "Experimental observation of Fermi-Pasta-Ulam recurrence in a nonlinear feedback ring system". In: *Physical review letters* 98.4 (2007), p. 047202.

[83] Chengying Bao et al. "Observation of Fermi-Pasta-Ulam recurrence induced by breather solitons in an optical microresonator". In: *Physical review letters* 117.16 (2016), p. 163901.

[84] Gaetan Van Simaeys, Ph Emplit, and Marc Haelterman. "Experimental demonstration of the Fermi-Pasta-Ulam recurrence in a modulationally unstable optical wave". In: *Physical review letters* 87.3 (2001), p. 033902.

[85] Arnaud Mussot et al. "Fermi-Pasta-Ulam recurrence in nonlinear fiber optics: the role of reversible and irreversible losses". In: *Physical Review X* 4.1 (2014), p. 011054.

[86] Arnaud Mussot et al. "Fibre multi-wave mixing combs reveal the broken symmetry of Fermi–Pasta–Ulam recurrence". In: *Nature Photonics* 12.5 (2018), p. 303.

[87] Mark J Ablowitz, B Prinari, and AD Trubatch. *Discrete and continuous nonlinear Schrödinger systems*. Vol. 302. Cambridge University Press, 2004.

[88] John M Dudley et al. "Modulation instability, Akhmediev Breathers and continuous wave supercontinuum generation". In: *Optics express* 17.24 (2009), pp. 21497–21508.

[89] B Frisquet, B Kibler, and G Millot. "Collision of Akhmediev breathers in nonlinear fiber optics". In: *Physical Review X* 3.4 (2013), p. 041032.

[90] Miro Erkintalo et al. "Higher-order modulation instability in nonlinear fiber optics". In: *Physical review letters* 107.25 (2011), p. 253901.

[91] A Chabchoub et al. "Super rogue waves: observation of a higher-order breather in water waves". In: *Physical Review X* 2.1 (2012), p. 011015.

[92] B Kibler et al. “Superregular breathers in optics and hydrodynamics: omnipresent modulation instability beyond simple periodicity”. In: *Physical Review X* 5.4 (2015), p. 041026.

[93] John M Dudley et al. “Instabilities, breathers and rogue waves in optics”. In: *Nature Photonics* 8.10 (2014), p. 755.

[94] Nail Akhmediev et al. “Roadmap on optical rogue waves and extreme events”. In: *Journal of Optics* 18.6 (2016), p. 063001.

[95] D Pierangeli et al. “Enhancing optical extreme events through input wave disorder”. In: *Physical Review A* 94.6 (2016), p. 063833.

[96] Pierre Suret et al. “Single-shot observation of optical rogue waves in integrable turbulence using time microscopy”. In: *Nature communications* 7 (2016), p. 13136.

[97] GP Berman and AR Kolovsky. “The limit of stochasticity for a one-dimensional chain of interacting oscillators”. In: *Zh. Eksp. Teor. Fiz* 87 (1984), p. 1938.

[98] E Infeld. “Quantitive theory of the Fermi-Pasta-Ulam recurrence in the nonlinear Schrödinger equation”. In: *Physical Review Letters* 47.10 (1981), p. 717.

[99] NN Akhmediev, VM Eleonskii, and NE Kulagin. “Exact first-order solutions of the nonlinear Schrödinger equation”. In: *Theoretical and mathematical physics* 72.2 (1987), pp. 809–818.

[100] F Di Mei et al. “Intrinsic negative mass from nonlinearity”. In: *Physical review letters* 116.15 (2016), p. 153902.

[101] D Pierangeli et al. “Super-crystals in composite ferroelectrics”. In: *Nature communications* 7 (2016), p. 10674.

[102] Qieni Lu et al. “Visualization of Spatial–Temporal Evolution of Light-Induced Refractive Index in Mn: Fe: KTN Co-Doped Crystal Based on Digital Holographic Interferometry”. In: *IEEE Photonics Journal* 7.4 (2015), pp. 1–11.

[103] Siu A Chin, Omar A Ashour, and Milivoj R Belić. “Anatomy of the Akhmediev breather: Cascading instability, first formation time, and Fermi-Pasta-Ulam recurrence”. In: *Physical Review E* 92.6 (2015), p. 063202.

[104] John M Martinis et al. “Rabi oscillations in a large Josephson-junction qubit”. In: *Physical review letters* 89.11 (2002), p. 117901.

[105] Natasha Devine et al. “Recurrence phase shift in Fermi–Pasta–Ulam nonlinear dynamics”. In: *Physics Letters A* 375.46 (2011), pp. 4158–4161.

[106] JM Soto-Crespo, N Devine, and N Akhmediev. “Adiabatic transformation of continuous waves into trains of pulses”. In: *Physical Review A* 96.2 (2017), p. 023825.

[107] Antonio Picozzi et al. “Optical wave turbulence: Towards a unified nonequilibrium thermodynamic formulation of statistical nonlinear optics”. In: *Physics Reports* 542.1 (2014), pp. 1–132.

[108] D Pierangeli et al. “Turbulent transitions in optical wave propagation”. In: *Physical review letters* 117.18 (2016), p. 183902.

[109] Davide Pierangeli et al. “Observation of replica symmetry breaking in disordered nonlinear wave propagation”. In: *Nature Communications* 8.1 (2017), p. 1501.

[110] NN Akhmediev et al. “Pseudorecurrence in two-dimensional modulation instability with a saturable self-focusing nonlinearity”. In: *Physical review letters* 65.12 (1990), p. 1423.

[111] Benno Rumpf and Alan C Newell. “Coherent structures and entropy in constrained, modulationally unstable, nonintegrable systems”. In: *Physical review letters* 87.5 (2001), p. 054102.

[112] Peng Zhang et al. “Generation of linear and nonlinear nonparaxial accelerating beams”. In: *Optics letters* 37.14 (2012), pp. 2820–2822.

[113] Noémi Wiersma et al. “Airy beam self-focusing in a photorefractive medium”. In: *Scientific reports* 6 (2016), p. 35078.

[114] R Gadonas et al. “Self-action of Bessel beam in nonlinear medium”. In: *Optics communications* 196.1-6 (2001), pp. 309–316.

[115] DE Roskey et al. “Self-action and regularized self-guiding of pulsed Bessel-like beams in air”. In: *Optics express* 15.16 (2007), pp. 9893–9907.

[116] Miguel A Porras et al. “Nonlinear unbalanced Bessel beams: stationary conical waves supported by nonlinear losses”. In: *Physical review letters* 93.15 (2004), p. 153902.

[117] Miguel A Porras, Carlos Ruiz-Jiménez, and Juan Carlos Losada. “Underlying conservation and stability laws in nonlinear propagation of axicon-generated Bessel beams”. In: *Physical Review A* 92.6 (2015), p. 063826.

[118] Pontus Johannisson et al. “Nonlinear bessel beams”. In: *Optics communications* 222.1-6 (2003), pp. 107–115.

[119] V Pyragaite et al. “Self-action of Bessel light beams in medium with large nonlinearity”. In: *Optics communications* 257.1 (2006), pp. 139–145.

[120] A Dubietis et al. “Axial emission and spectral broadening in self-focusing of femtosecond Bessel beams”. In: *Optics Express* 15.7 (2007), pp. 4168–4175.

[121] Oleg G Romanov et al. “Propagation and self-action of Bessel light beams in dye solutions”. In: *Nonlinear Phenomena in Complex Systems* 16.4 (2013), pp. 373–381.

[122] Miguel A Porras, Carlos Ruiz-Jiménez, and Márcio Carvalho. “Stationary and stable light-beam propagation in Kerr media with nonlinear absorption with controllable dissipation patterns”. In: *Physical Review A* 95.4 (2017), p. 043816.

[123] Yuri S Kivshar and Dmitry E Pelinovsky. “Self-focusing and transverse instabilities of solitary waves”. In: *Physics Reports* 331.4 (2000), pp. 117–195.

[124] Mordechai Segev et al. “Spatial solitons in photorefractive media”. In: *Physical Review Letters* 68.7 (1992), p. 923.

[125] Matthew Morin et al. “Waveguides formed by quasi-steady-state photorefractive spatial solitons”. In: *Optics letters* 20.20 (1995), pp. 2066–2068.

[126] Nicolas Fressengeas et al. “Build up mechanisms of (1+ 1)-dimensional photorefractive bright spatial quasi-steady-state and screening solitons”. In: *Optics communications* 145.1-6 (1998), pp. 393–400.

[127] Marcus Asaro et al. “Soliton-induced waveguides in an organic photorefractive glass”. In: *Optics letters* 30.5 (2005), pp. 519–521.

[128] Erwan Lucas et al. “Breathing dissipative solitons in optical microresonators”. In: *Nature communications* 8.1 (2017), p. 736.

[129] Mengjie Yu et al. “Breather soliton dynamics in microresonators”. In: *Nature communications* 8 (2017), p. 14569.

[130] Eugenijus Gaižauskas et al. “Discrete damage traces from filamentation of Gauss-Bessel pulses”. In: *Optics letters* 31.1 (2006), pp. 80–82.

[131] J Arlt and K Dholakia. “Generation of high-order Bessel beams by use of an axicon”. In: *Optics Communications* 177.1-6 (2000), pp. 297–301.

[132] G Di Domenico et al. “Miniaturized photogenerated electro-optic axicon lens Gaussian-to-Bessel beam conversion”. In: *Applied optics* 56.10 (2017), pp. 2908–2911.

[133] G Antonacci et al. “Diffraction-free light droplets for axially-resolved volume imaging”. In: *Scientific Reports* 7.1 (2017), p. 17.

[134] Cesare Dari-Salisburgo, Eugenio DelRe, and Elia Palange. “Molding and stretched evolution of optical solitons in cumulative nonlinearities”. In: *Physical review letters* 91.26 (2003), p. 263903.

[135] Junkichi Satsuma and Nobuo Yajima. “B. Initial value problems of one-dimensional self-modulation of nonlinear waves in dispersive media”. In: *Progress of Theoretical Physics Supplement* 55 (1974), pp. 284–306.

[136] D John Mitchell and Allan W Snyder. “Soliton dynamics in a nonlocal medium”. In: *JOSA B* 16.2 (1999), pp. 236–239.

[137] Claudio Conti, Marco Peccianti, and Gaetano Assanto. “Observation of optical spatial solitons in a highly nonlocal medium”. In: *Physical review letters* 92.11 (2004), p. 113902.

[138] M-F Shih et al. “Observation of two-dimensional steady-state photorefractive screening solitons”. In: *Electronics Letters* 31.10 (1995), pp. 826–827.

[139] Eugenio DelRe et al. “Two-dimensional photorefractive spatial solitons in centrosymmetric paraelectric potassium–lithium–tantalate–niobate”. In: *Applied physics letters* 73.1 (1998), pp. 16–18.

[140] Nicholas C Harris et al. “Quantum transport simulations in a programmable nanophotonic processor”. In: *Nature Photonics* 11.7 (2017), p. 447.

[141] Yichen Shen et al. “Deep learning with coherent nanophotonic circuits”. In: *Nature Photonics* 11.7 (2017), p. 441.

[142] Xiaogang Qiang et al. “Large-scale silicon quantum photonics implementing arbitrary two-qubit processing”. In: *Nature Photonics* 12.9 (2018), p. 534.

[143] Amy C Sullivan, Matthew W Grabowski, and Robert R McLeod. “Three-dimensional direct-write lithography into photopolymer”. In: *Applied optics* 46.3 (2007), pp. 295–301.

[144] Graham D Marshall et al. “Laser written waveguide photonic quantum circuits”. In: *Optics express* 17.15 (2009), pp. 12546–12554.

[145] Fulvio Flamini et al. “Thermally reconfigurable quantum photonic circuits at telecom wavelength by femtosecond laser micromachining”. In: *Light: Science & Applications* 4.11 (2015), e354.

[146] Zachary Chaboyer et al. “Design and fabrication of reconfigurable laser-written waveguide circuits”. In: *Optics Express* 25.26 (2017), pp. 33056–33065.

[147] Yang Yang et al. “Recent Progress in Biomimetic Additive Manufacturing Technology: From Materials to Functional Structures”. In: *Advanced Materials* (2018), p. 1706539.

[148] James W Chan et al. “Waveguide fabrication in phosphate glasses using femtosecond laser pulses”. In: *Applied physics letters* 82.15 (2003), pp. 2371–2373.

[149] Tanya M Monro, C Martiin De Sterke, and L Poladian. “Catching light in its own trap”. In: *Journal of Modern Optics* 48.2 (2001), pp. 191–238.

[150] Hidetaka Terasawa et al. “Light-induced self-written waveguide fabrication using 1550 nm laser light”. In: *Optics letters* 42.11 (2017), pp. 2236–2238.

[151] Ra’ed Malallah et al. “Self-written waveguides in photopolymer”. In: *Applied Optics* 57.22 (2018), E80–E88.

[152] Anna Bezryadina et al. “Nonlinear self-action of light through biological suspensions”. In: *Physical review letters* 119.5 (2017), p. 058101.

[153] Song Lan et al. “Directional coupler with soliton-induced waveguides”. In: *Optics letters* 24.7 (1999), pp. 475–477.

[154] Kokou Dorkenoo et al. “Quasi-solitonic behavior of self-written waveguides created by photopolymerization”. In: *Optics letters* 27.20 (2002), pp. 1782–1784.

[155] Chien-Chung Jeng et al. “Control modulation instability in photorefractive crystals by the intensity ratio of background to signal fields”. In: *Optics express* 23.8 (2015), pp. 10266–10271.

[156] Eugenio DelRe et al. “Electro-optic beam manipulation through photorefractive needles”. In: *Optics letters* 27.24 (2002), pp. 2188–2190.

[157] A Pierangelo et al. “Electro-activation and electro-morphing of photorefractive funnel waveguides”. In: *Optics Express* 17.25 (2009), pp. 22659–22665.

[158] J Parravicini et al. “Volume integrated phase modulator based on funnel waveguides for reconfigurable miniaturized optical circuits”. In: *Optics letters* 40.7 (2015), pp. 1386–1389.

[159] Cornelia Denz, Sergej Flach, and Yuri S Kivshar. *Nonlinearities in periodic structures and metamaterials*. Vol. 150. Springer, 2010.

[160] HS Eisenberg et al. “Diffraction management”. In: *Physical Review Letters* 85.9 (2000), p. 1863.

[161] Jason W Fleischer et al. “Spatial photonics in nonlinear waveguide arrays”. In: *Optics express* 13.6 (2005), pp. 1780–1796.

[162] Yaroslav V Kartashov, Boris A Malomed, and Lluis Torner. “Solitons in nonlinear lattices”. In: *Reviews of Modern Physics* 83.1 (2011), p. 247.

[163] Jason W Fleischer et al. “Observation of discrete solitons in optically induced real time waveguide arrays”. In: *Physical review letters* 90.2 (2003), p. 023902.

[164] Nikos K Efremidis et al. “Discrete solitons in photorefractive optically induced photonic lattices”. In: *Physical Review E* 66.4 (2002), p. 046602.

[165] Daniel Mandelik et al. “Band-gap structure of waveguide arrays and excitation of Floquet-Bloch solitons”. In: *Physical review letters* 90.5 (2003), p. 053902.

[166] D Mandelik et al. “Gap solitons in waveguide arrays”. In: *Physical review letters* 92.9 (2004), p. 093904.

[167] Cibo Lou et al. “Nonlinear spectrum reshaping and gap-soliton-train trapping in optically induced photonic structures”. In: *Physical review letters* 98.21 (2007), p. 213903.

[168] Peng Zhang et al. “Optically induced transition between discrete and gap solitons in a nonconventionally biased photorefractive crystal”. In: *Optics letters* 33.8 (2008), pp. 878–880.

[169] Yannis Kominis. “Bright, dark, antidark, and kink solitons in media with periodically alternating sign of nonlinearity”. In: *Physical Review A* 87.6 (2013), p. 063849.

[170] ZH Musslimani et al. “Optical Solitons in P T Periodic Potentials”. In: *Physical Review Letters* 100.3 (2008), p. 030402.

[171] U Naether et al. “Self-trapping threshold in disordered nonlinear photonic lattices”. In: *Optics letters* 38.9 (2013), pp. 1518–1520.

[172] Alessandro Ciattoni et al. “Photorefractive solitons embedded in gratings in centrosymmetric crystals”. In: *Optics letters* 31.11 (2006), pp. 1690–1692.

[173] D Pierangeli et al. “Observation of an intrinsic nonlinearity in the electro-optic response of freezing relaxors ferroelectrics”. In: *Optical Materials Express* 4.8 (2014), pp. 1487–1493.

[174] AJ Agranat, CEM de Oliveira, and G Orr. “Dielectric electrooptic gratings in potassium lithium tantalate niobate”. In: *Journal of Non-Crystalline Solids* 353.47-51 (2007), pp. 4405–4410.

[175] Aharon J Agranat et al. “Stable electro-optic striation grating produced by programed periodic modulation of the growth temperature”. In: *Applied physics letters* 90.19 (2007), p. 192902.

[176] Lei Wang et al. “Field-induced enhancement of voltage-controlled diffractive properties in paraelectric iron and manganese co-doped potassium–tantalate–niobate crystal”. In: *Applied Physics Express* 7.11 (2014), p. 112601.

[177] Tadayuki Imai et al. “Changes in permittivity of KTa1- xNbxO3 crystals induced by electron injection in relation to nonlinear dielectric response”. In: *Applied Physics Express* 7.7 (2014), p. 071501.

[178] J Parravicini et al. “Aging solitons in photorefractive dipolar glasses”. In: *Optics Express* 21.25 (2013), pp. 30573–30579.

[179] Viola Folli, Eugenio DelRe, and Claudio Conti. “Beam instabilities in the scale-free regime”. In: *Physical review letters* 108.3 (2012), p. 033901.

[180] M Ferraro et al. “Observation of polarization-maintaining light propagation in depoled compositionally disordered ferroelectrics”. In: *Optics letters* 42.19 (2017), pp. 3856–3859.

[181] Fabrizio Di Mei et al. “Giant broadband refraction in the visible in a ferroelectric perovskite”. In: *Nature Photonics* 12 (2018), pp. 734–738.

[182] Samuel D Stranks and Henry J Snaith. "Metal-halide perovskites for photovoltaic and light-emitting devices". In: *Nature nanotechnology* 10.5 (2015), p. 391.

[183] Yun-Ching Chang et al. "Giant electro-optic effect in nanodisordered KTN crystals". In: *Optics letters* 38.22 (2013), pp. 4574–4577.

[184] Xin Zhang et al. "Abnormal optical anisotropy in correlated disorder KTa 1- x Nb x O 3: Cu with refractive index gradient". In: *Scientific reports* 8.1 (2018), p. 2892.

[185] Vladimir V Shvartsman and Doru C Lupascu. "Lead-free relaxor ferroelectrics". In: *Journal of the American Ceramic Society* 95.1 (2012), pp. 1–26.

[186] Eugenio DelRe and Aharon J Agranat. "Dielectric nonlinearity in photorefractive spatial soliton formation". In: *Physical Review A* 65.5 (2002), p. 053814.

[187] George A Samara. "The relaxational properties of compositionally disordered ABO3 perovskites". In: *Journal of Physics: Condensed Matter* 15.9 (2003), R367.

[188] AA Bokov and Z-G Ye. "Recent progress in relaxor ferroelectrics with perovskite structure". In: *Journal of materials science* 41.1 (2006), pp. 31–52.

[189] Jose Trull et al. "Second-harmonic parametric scattering in ferroelectric crystals with disordered nonlinear domain structures". In: *Optics express* 15.24 (2007), pp. 15868–15877.

[190] Vito Roppo et al. "The role of ferroelectric domain structure in second harmonic generation in random quadratic media". In: *Optics Express* 18.5 (2010), pp. 4012–4022.

[191] Mousa Ayoub, Jörg Imbrock, and Cornelia Denz. "Second harmonic generation in multi-domain χ 2 media: from disorder to order". In: *Optics express* 19.12 (2011), pp. 11340–11354.

[192] Eugenio DelRe et al. "Subwavelength anti-diffracting beams propagating over more than 1,000 Rayleigh lengths". In: *Nature Photonics* 9.4 (2015), p. 228.

[193] Qieni Lu et al. "Field-induced lifetime enhancement of photorefractive gratings in a Mn: Fe: KTN crystal". In: *Optics letters* 42.13 (2017), pp. 2407–2410.

[194] Alexander Gumennik, Yael Kurzweil-Segev, and Aharon J Agranat. "Electrooptical effects in glass forming liquids of dipolar nano-clusters embedded in a paraelectric environment". In: *Optical Materials Express* 1.3 (2011), pp. 332–343.

[195] Hao Tian et al. "Impact of polar nanoregions on the quadratic electro-optic effect in K0. 95Na0. 05Ta1- xNbxO3 crystals near the Curie temperature". In: *Applied Physics Express* 7.6 (2014), p. 062601.

[196] Peng Tan et al. "Temperature field driven polar nanoregions in KTa1- x Nb x O3". In: *Applied Physics Letters* 109.25 (2016), p. 252904.

[197] Xiangda Meng et al. “Strong electromechanical coupling in paraelectric KTa1-xNbxO3 crystals”. In: *Journal of the American Ceramic Society* 100.11 (2017), pp. 5220–5225.

[198] Hao Tian et al. “Dynamic response of polar nanoregions under an electric field in a paraelectric KTa 0.61 Nb 0.39 O 3 single crystal near the para-ferroelectric phase boundary”. In: *Scientific reports* 5 (2015), p. 13751.

[199] Peng Tan et al. “Field-driven electro-optic dynamics of polar nanoregions in nanodisordered KTa1- x Nb x O3 crystal”. In: *Applied Physics Letters* 111.1 (2017), p. 012903.

[200] Gerald Burns and FH Dacol. “Glassy polarization behavior in ferroelectric compounds Pb (Mg13Nb23) O3 and Pb (Zn13Nb23) O3”. In: *Solid state communications* 48.10 (1983), pp. 853–856.

[201] Dwight Viehland et al. “Freezing of the polarization fluctuations in lead magnesium niobate relaxors”. In: *Journal of Applied Physics* 68.6 (1990), pp. 2916–2921.

[202] Jacopo Parravicini et al. “Liquid–solid directional composites and anisotropic dipolar phases of polar nanoregions in disordered perovskites”. In: *Nanoscale* 9.27 (2017), pp. 9572–9580.

[203] Karin M Rabe, Charles H Ahn, and Jean-Marc Triscone. *Physics of ferroelectrics: a modern perspective*. Vol. 105. Springer Science & Business Media, 2007.

[204] CEM De Oliveira et al. “Controlled composition modulation in potassium lithium tantalate niobate crystals grown by off-centered TSSG method”. In: *Journal of crystal growth* 273.1-2 (2004), pp. 203–206.

[205] G. N. Ramachandran. *Advanced Methods of Crystallography*. Academic Press, Inc., 1964.

[206] Assaf Bitman et al. “Electroholographic tunable volume grating in the g 44 configuration”. In: *Optics letters* 31.19 (2006), pp. 2849–2851.

[207] W Kleemann, FJ Schäfer, and D Rytz. “Diffuse Ferroelectric Phase Transition and Long-Range Order of Dilute K Ta 1- x Nb x O 3”. In: *Physical review letters* 54.18 (1985), p. 2038.

[208] V Westphal, W Kleemann, and MD Glinchuk. “Diffuse phase transitions and random-field-induced domain states of the “relaxor”ferroelectric PbMg 1/3 Nb 2/3 O 3”. In: *Physical Review Letters* 68.6 (1992), p. 847.

[209] M Takagi and T Ishidate. “Anomalous birefringence of cubic BaTiO3”. In: *Solid state communications* 113.7 (2000), pp. 423–426.

[210] AM Pugachev et al. “Broken local symmetry in paraelectric BaTiO 3 proved by second harmonic generation”. In: *Physical review letters* 108.24 (2012), p. 247601.

[211] Tadayuki Imai, Jun Miyazu, and Junya Kobayashi. "Measurement of charge density distributions in KTa 1-x Nb x O 3 optical beam deflectors". In: *Optical Materials Express* 4.5 (2014), pp. 976–981.

[212] Hao Tian et al. "Variable gradient refractive index engineering: design, growth and electro-deflective application of KTa 1- x Nb x O 3". In: *Journal of Materials Chemistry C* 3.42 (2015), pp. 10968–10973.

[213] Wenbin Zhu et al. "Three order increase in scanning speed of space charge-controlled KTN deflector by eliminating electric field induced phase transition in nanodisordered KTN". In: *Scientific reports* 6 (2016), p. 33143.

[214] Ju-Hung Chao et al. "High speed non-mechanical two-dimensional KTN beam deflector enabled by space charge and temperature gradient deflection". In: *Optics Express* 25.13 (2017), pp. 15481–15492.

[215] Jacopo Parravicini et al. "Macroscopic response and directional disorder dynamics in chemically substituted ferroelectrics". In: *Physical Review B* 93.9 (2016), p. 094203.

[216] Amnon Yariv and Pochi Yeh. *Optical waves in crystals*. Vol. 5. John Wiley & Sons, New York, 1984.

[217] Andriy Shevchenko et al. "Polarization time of unpolarized light". In: *Optica* 4.1 (2017), pp. 64–70.

[218] Paul J Campagnola and Leslie M Loew. "Second-harmonic imaging microscopy for visualizing biomolecular arrays in cells, tissues and organisms". In: *Nature biotechnology* 21.11 (2003), p. 1356.

[219] Robert W. Boyd. *Nonlinear Optics, Third Edition*. 3rd. Orlando, FL, USA: Academic Press, Inc., 2008. ISBN: 0123694701, 9780123694706.

[220] Dunzhao Wei et al. "Experimental demonstration of a three-dimensional lithium niobate nonlinear photonic crystal". In: *Nature Photonics* 12.10 (2018), p. 596.

[221] N.W. Ashcroft and N.D. Mermin. *Solid State Physics*. HRW international editions. Holt, Rinehart and Winston, 1976. ISBN: 9780030839931.

[222] Solomon M Saltiel et al. "Multiorder nonlinear diffraction in frequency doubling processes". In: *Optics letters* 34.6 (2009), pp. 848–850.

[223] Martin M Fejer et al. "Quasi-phase-matched second harmonic generation: tuning and tolerances". In: *IEEE Journal of Quantum Electronics* 28.11 (1992), pp. 2631–2654.

[224] V Berger. "Nonlinear photonic crystals". In: *Physical review letters* 81.19 (1998), p. 4136.

[225] Solomon M Saltiel et al. "Generation of second-harmonic conical waves via nonlinear Bragg diffraction". In: *Physical review letters* 100.10 (2008), p. 103902.

[226] Yehuda B Band. *Light and matter: electromagnetism, optics, spectroscopy and lasers*. Vol. 1. John Wiley & Sons, 2006.

[227] Robert Fischer et al. "Broadband femtosecond frequency doubling in random media". In: *Applied physics letters* 89.19 (2006), p. 191105.

[228] Anna Fragemann, Valdas Pasiskevicius, and Fredrik Laurell. "Second-order nonlinearities in the domain walls of periodically poled KTiOPO 4". In: *Applied Physics Letters* 85.3 (2004), pp. 375–377.

[229] Alexandr A Kaminskii et al. "Second-harmonic generation with Cherenkov-type phase matching in a bulk nonlinear LaBGeO5 crystal". In: *Quantum Electronics* 26.5 (1996), p. 381.

[230] Mousa Ayoub et al. "Čerenkov-type second-harmonic spectroscopy in random nonlinear photonic structures". In: *Optics express* 21.7 (2013), pp. 8220–8230.

[231] Mousa Ayoub, Jörg Imbrock, and Cornelia Denz. "Ferroelectric domain diagnostics near the phase transition by Čerenkov second-harmonic generation". In: *Optical Materials Express* 7.9 (2017), pp. 3448–3455.

[232] Tianxiang Xu et al. "Three-dimensional nonlinear photonic crystal in ferroelectric barium calcium titanate". In: *Nature Photonics* (2018), p. 1.

[233] Stefan W Hell. "Far-field optical nanoscopy". In: *science* 316.5828 (2007), pp. 1153–1158.

[234] Mark L Brongersma, Yi Cui, and Shanhui Fan. "Light management for photovoltaics using high-index nanostructures". In: *Nature materials* 13.5 (2014), p. 451.

[235] Amnon Yariv. *Quantum Electronics*. John Wiley & Sons, New York, 1967.

[236] Max Born and Emil Wolf. *Principles of optics: electromagnetic theory of propagation, interference and diffraction of light*. Cambridge University Press, 2005.

[237] Ku Im, Ji-Hun Kang, and Q-Han Park. "Universal impedance matching and the perfect transmission of white light". In: *Nature Photonics* 12.3 (2018), p. 143.

[238] Alexei A Bokov and Zuo-Guang Ye. "Dielectric relaxation in relaxor ferroelectrics". In: *Journal of Advanced dielectrics* 2.02 (2012), p. 1241010.

[239] PC Bons et al. "Quantum enhancement of the index of refraction in a Bose-Einstein condensate". In: *Physical review letters* 116.17 (2016), p. 173602.

[240] Taeyong Chang et al. "Broadband giant-refractive-index material based on mesoscopic space-filling curves". In: *Nature communications* 7 (2016), p. 12661.

[241] Francesco Aieta et al. "Multiwavelength achromatic metasurfaces by dispersive phase compensation". In: *Science* 347.6228 (2015), pp. 1342–1345.

[242] Scott Marshall Mansfield and GS Kino. "Solid immersion microscope". In: *Applied physics letters* 57.24 (1990), pp. 2615–2616.

[243] John B Pendry, David Schurig, and David R Smith. "Controlling electromagnetic fields". In: *science* 312.5781 (2006), pp. 1780–1782.

[244] Darrick E Chang, Vladan Vuletić, and Mikhail D Lukin. "Quantum nonlinear optics—photon by photon". In: *Nature Photonics* 8.9 (2014), p. 685.

[245] Lucia Caspani et al. "Integrated sources of photon quantum states based on nonlinear optics". In: *Light: Science & Applications* 6.11 (2017), e17100.

[246] M Flammini et al. "Evanescent-Wave Filtering in Images Using Remote Terahertz Structured Illumination". In: *Physical Review Applied* 8.5 (2017), p. 054019.

[247] Mariano Flammini et al. "Confocal Terahertz Imaging of Ancient Manuscripts". In: *Journal of Infrared, Millimeter, and Terahertz Waves* 38.4 (2017), pp. 435–442.

[248] Chiara Ciano et al. "Confocal Imaging at 0.3 THz With Depth Resolution of a Painted Wood Artwork for the Identification of Buried Thin Metal Foils". In: *IEEE Transactions on Terahertz Science and Technology* (2018).

[249] Jean-Jacques Greffet and Rémi Carminati. "Image formation in near-field optics". In: *Progress in surface science* 56.3 (1997), pp. 133–237.

[250] Florian Ströhl and Clemens F Kaminski. "Frontiers in structured illumination microscopy". In: *Optica* 3.6 (2016), pp. 667–677.

[251] Joseph W Goodman. *Introduction to Fourier optics*. Roberts and Company Publishers, 2005.

[252] EdwardH Synge. "A suggested method for extending microscopic resolution into the ultra-microscopic region". In: *The London, Edinburgh, and Dublin Philosophical Magazine and Journal of Science* 6.35 (1928), pp. 356–362.

[253] EA Ash and G Nicholls. "Super-resolution aperture scanning microscope". In: *Nature* 237.5357 (1972), p. 510.

[254] Mats GL Gustafsson. "Surpassing the lateral resolution limit by a factor of two using structured illumination microscopy". In: *Journal of microscopy* 198.2 (2000), pp. 82–87.

[255] Feifei Wei et al. "Wide field super-resolution surface imaging through plasmonic structured illumination microscopy". In: *Nano letters* 14.8 (2014), pp. 4634–4639.

[256] DR Skinner and RE Whitcher. "Measurement of the radius of a high-power laser beam near the focus of a lens". In: *Journal of Physics E: Scientific Instruments* 5.3 (1972), p. 237.

[257] Arthur H Firester, ME Heller, and Ping Sheng. "Knife-edge scanning measurements of subwavelength focused light beams". In: *Applied Optics* 16.7 (1977), pp. 1971–1974.

[258] Eric Betzig. "Nobel Lecture: Single molecules, cells, and super-resolution optics". In: *Reviews of Modern Physics* 87.4 (2015), p. 1153.

[259] Marco Peccianti et al. "Exact Reconstruction of THz Sub-λ Source Features in Knife-Edge Measurements". In: *IEEE Journal of Selected Topics in Quantum Electronics* 19.1 (2013), pp. 8401211–8401211.

[260] Sze Ho Phing et al. "Sub-wavelength terahertz beam profiling of a THz source via an all-optical knife-edge technique". In: *Scientific reports* 5 (2015), p. 8551.

[261] CJR Sheppard, Min Gu, and XQ Mao. "Three-dimensional coherent transfer function in a reflection-mode confocal scanning microscope". In: *Optics communications* 81.5 (1991), pp. 281–284.

[262] Kai Wicker and Rainer Heintzmann. "Resolving a misconception about structured illumination". In: *Nature Photonics* 8.5 (2014), p. 342.

[263] Robert H Webb. "Confocal optical microscopy". In: *Reports on Progress in Physics* 59.3 (1996), p. 427.

[264] Alireza Kazemipour et al. "The horn antenna as Gaussian source in the mm-wave domain". In: *Journal of Infrared, Millimeter, and Terahertz waves* 35.9 (2014), pp. 720–731.

[265] C Huber et al. "Corrections to the knife-edge based reconstruction scheme of tightly focused light beams". In: *Optics express* 21.21 (2013), pp. 25069–25076.

[266] Oleg Mitrofanov et al. "Collection-mode near-field imaging with 0.5-THz pulses". In: *IEEE Journal of Selected Topics in Quantum Electronics* 7.4 (2001), pp. 600–607.

[267] A Apostol and A Dogariu. "Spatial correlations in the near field of random media". In: *Physical review letters* 91.9 (2003), p. 093901.

[268] Raimund Mueckstein et al. "Imaging and analysis of THz surface plasmon polariton waves with the integrated sub-wavelength aperture probe". In: *Journal of Infrared, Millimeter, and Terahertz Waves* 32.8-9 (2011), p. 1031.

[269] Andreas J Huber et al. "Terahertz near-field nanoscopy of mobile carriers in single semiconductor nanodevices". In: *Nano letters* 8.11 (2008), pp. 3766–3770.

[270] IC Moldovan-Doyen et al. "Low temperature near-field scanning optical microscopy on infrared and terahertz photonic-crystal quantum cascade lasers". In: *Applied Physics Letters* 98.23 (2011), p. 231112.

[271] Hiroshi Hatano, Yasushi Inouye, and Satoshi Kawata. “Near-field optical microscope with a multiheight scanning–imaging mode”. In: *Optics letters* 22.20 (1997), pp. 1532–1534.

[272] Oleg Mitrofanov et al. “Terahertz pulse propagation through small apertures”. In: *Applied Physics Letters* 79.7 (2001), pp. 907–909.

[273] U Schade et al. “THz near-field imaging employing synchrotron radiation”. In: *Applied physics letters* 84.8 (2004), pp. 1422–1424.

[274] Yukio Kawano and Koji Ishibashi. “An on-chip near-field terahertz probe and detector”. In: *Nature Photonics* 2.10 (2008), p. 618.

[275] Oleg Mitrofanov et al. “Waveguide mode imaging and dispersion analysis with terahertz near-field microscopy”. In: *Applied Physics Letters* 94.17 (2009), p. 171104.

[276] Alexander J Macfaden et al. “3 μ m aperture probes for near-field terahertz transmission microscopy”. In: *Applied Physics Letters* 104.1 (2014), p. 011110.

[277] Nicholas Karpowicz et al. “Compact continuous-wave subterahertz system for inspection applications”. In: *Applied Physics Letters* 86.5 (2005), p. 054105.

[278] Mohammed Adnan Salhi, Ioachim Pupeza, and Martin Koch. “Confocal THz laser microscope”. In: *Journal of Infrared, Millimeter, and Terahertz Waves* 31.3 (2010), pp. 358–366.

[279] S Mair, B Gompf, and M Dressel. “Spatial and spectral behavior of the optical near field studied by a terahertz near-field spectrometer”. In: *Applied physics letters* 84.7 (2004), pp. 1219–1221.